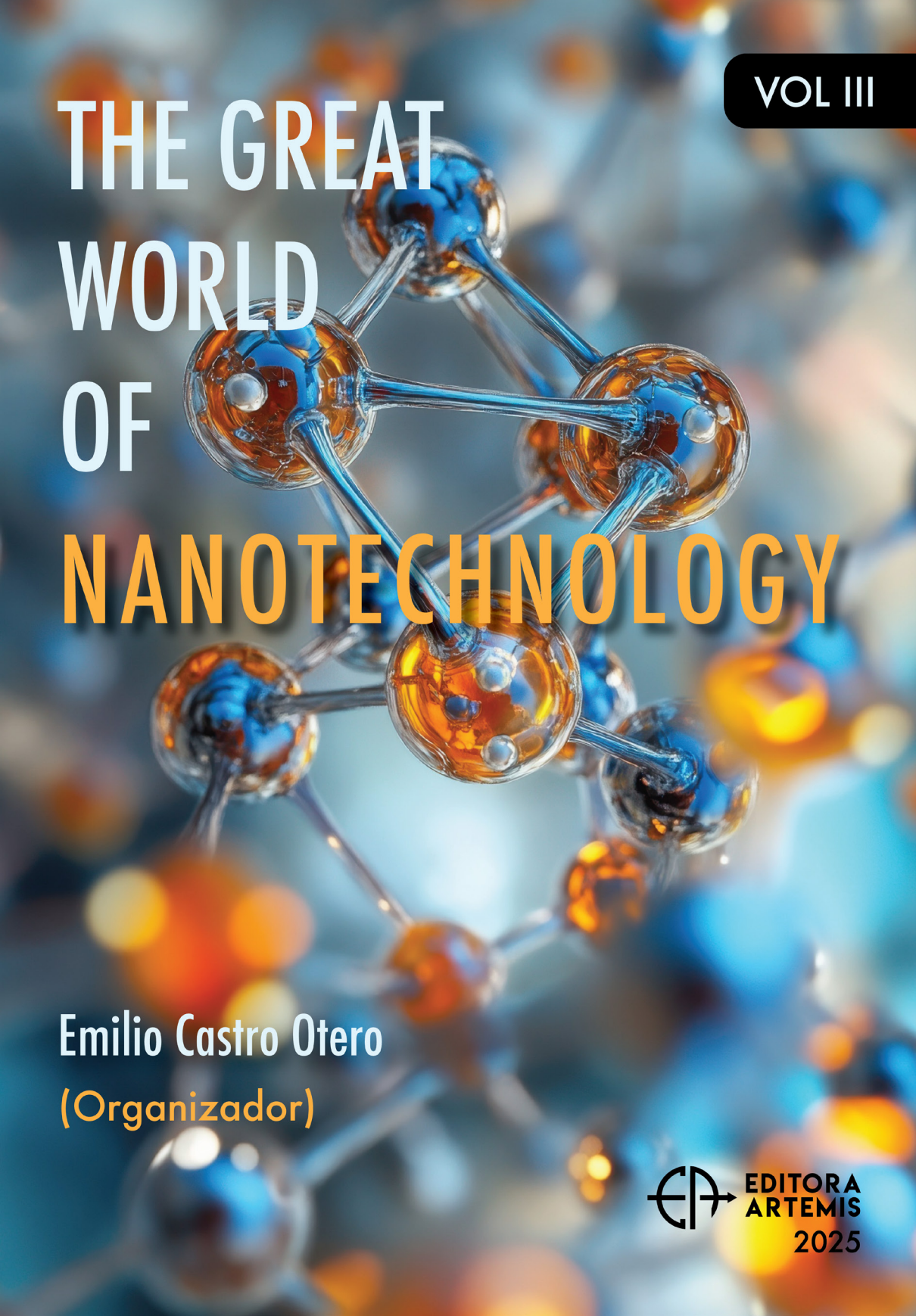
VOL III
THE GREAT WORLD OF NANOTECHNOLOGY
Emilio Castro Otero
(Organizador)
EDITORA ARTEMIS
2025

VOL III

THE GREAT WORLD OF NANOTECHNOLOGY

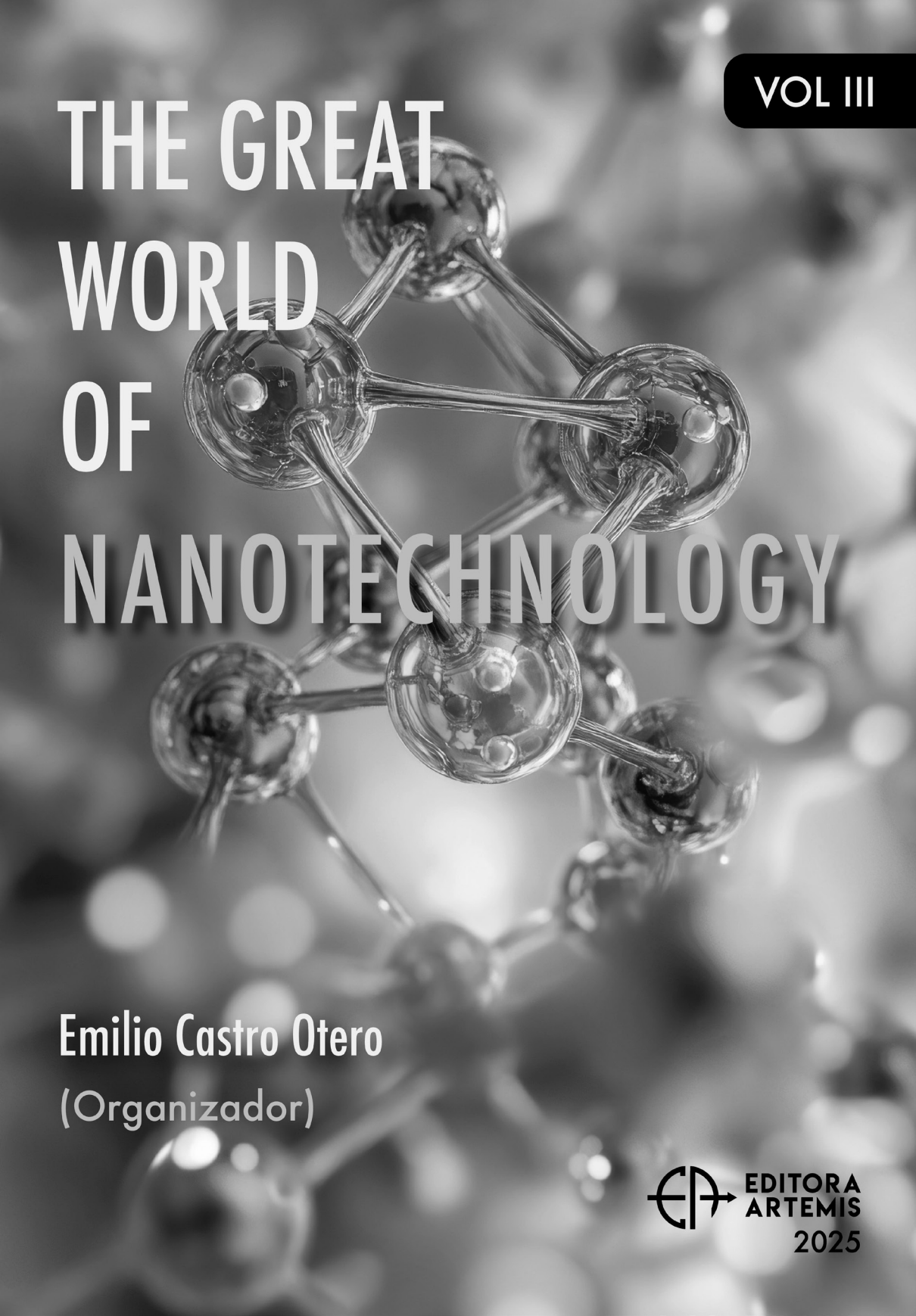

Emilio Castro Otero
(Organizador)

EDITORA ARTEMIS
2025

Editora Chefe	Profª Drª Antonella Carvalho de Oliveira
Editora Executiva	M.ª Viviane Carvalho Mocellin
Direção de Arte	M.ª Bruna Bejarano
Diagramação	Elisangela Abreu
Organizador	Prof. Dr. Emilio Castro Otero
Imagem da Capa	yourapechkin/123RF
Bibliotecário	Maurício Amormino Júnior – CRB6/2422

Editora Artemis
Curitiba-PR Brasil
www.editoraartemis.com.br
e-mail:publicar@editoraartemis.com.br

Editora Artemis
Curitiba-PR Brasil
www.editoraartemis.com.br
e-mail:publicar@editoraartemis.com.br

Dados Internacionais de Catalogação na Publicação (CIP)
(eDOC BRASIL, Belo Horizonte/MG)

O86g The Great World of Nanotechnology III / organização de Emilio Castro Otero. – 1. ed. – Curitiba, PR : Editora Artemis, 2025.

Formato: PDF
Requisitos de sistema: Adobe Acrobat Reader
Modo de acesso: World Wide Web
Edição bilíngue.
Inclui bibliografia
ISBN 978-65-81701-79-6
DOI 10.37572/EdArt_121225796

1. Nanotecnologia biomédica. 2. Engenharia de tecidos. 3. Nanomateriais – Aplicações. 4. Biossistemas – Inovação tecnológica. 5. Sensores avançados – Desenvolvimento. I. Otero, Emilio Castro.

CDD 620.5

Elaborado por Maurício Amormino Júnior – CRB6/2422

EDITORA ARTEMIS
2025

Editora Artemis
Curitiba-PR Brasil
www.editoraartemis.com.br
e-mail:publicar@editoraartemis.com.br

FOREWORD

We are thrilled to present the third installment of ***The Great World of Nanotechnology***, a volume dedicated to exploring the cutting edge of nanotechnology applications, from the fundamental science of materials to their tangible impact on health, industry, and the environment. This book is meticulously structured into four thematic blocks, designed to guide the reader through the latest innovations that seek to solve crucial challenges in modern society.

The first pillar of this volume, ***Fundamentals of Nanomaterial Manufacturing and Characterization***, delves into the critical methodologies for creating high-quality nanostructures. Chapter 1 offers systematic research on the Effects of the Transfer Process on the Structure of Graphene Synthesized by Chemical Vapor Deposition. Complementing this, Chapter 2 examines Polymer Nanofibers via Airbrushing.

In ***Nanomaterials for Surface Engineering and Smart Sensors****, the chapters* explore how these nanostructures can be applied in functional devices and material protection. Chapter 3 presents advances in the development of sensors based on graphene functionalized with nanoparticles. Similarly, Chapter 4 addresses the electrodeposition of nanostructured metal coatings.

Nanotechnology in Biomedical and Pharmaceutical Applications brings three chapters focusing on the use of nanotechnology to improve human health. Chapter 5 evaluates the Cytotoxic Effect of Nanoemulsion with Pumpkin Seed Oil on Breast Cancer Cell Lines. In the field of tissue engineering, Chapter 6 describes the development of Alginate/Collagen Structures Enhanced with Conductive Nanoparticles (PEDOT) for the Regeneration of Small-Diameter Blood Vessels. Finally, Chapter 7 discusses the development of an antiseptic gel based on bioactive compounds encapsulated in nanoparticles.

Concluding our exploration, ***Nanotechnological Solutions for Environmental Remediation*** addresses the water pollution crisis. The final chapter describes the Removal of Arsenic from Groundwater Using Recycled Iron Nanoparticles through the development of a low-cost filter that uses iron nanoparticles.

We invite you to immerse yourself in reading The Great World of Nanotechnology. Vol. III, where science on the smallest scale translates into large-scale solutions. We sincerely hope that this compilation of advanced research will not only be of utmost interest to you, but also inspire new directions of study and application in this infinitely promising field.

Emilio Castro Otero

PRÓLOGO

É com grande entusiasmo que apresentamos a terceira edição de ***The Great World of Nanotechnology***, um volume dedicado a explorar a vanguarda das aplicações nanotecnológicas, desde a ciência fundamental dos materiais até o seu impacto tangível na saúde, na indústria e no ambiente. Este livro está meticulosamente estruturado em quatro eixos temáticos, concebidos para guiar o leitor através das mais recentes inovações que procuram resolver desafios cruciais na sociedade moderna.

O primeiro eixo deste volume, ***Fundamentos da Fabricação e Caracterização de Nanomateriais***, aprofunda as metodologias críticas para a criação de nanoestruturas de alta qualidade. O Capítulo 1 oferece uma investigação sistemática sobre os Efeitos do Processo de Transferência na Estrutura do Grafeno Sintetizado por Deposição Química de Vapor e o segundo capítulo examina as Nanofibras Poliméricas via Aerografia.

Em seguida, o eixo ***Nanomateriais para Engenharia de Superfícies e Sensores Inteligentes***, explora como essas nanoestruturas podem ser aplicadas em dispositivos funcionais e proteção de materiais. O Capítulo 3 apresenta os avanços no desenvolvimento de Sensores Baseados em Grafeno Funcionalizado com Nanopartículas. Paralelamente, e o Capítulo 4 aborda a Eletrodeposição de Revestimentos Metálicos Nanoestruturados.

O eixo ***Nanotecnologia em Aplicações Biomédicas e Farmacêuticas***, centra-se na utilização da nanotecnologia para melhorar a saúde humana. O Capítulo 5 avalia o Efeito Citotóxico da Nanoemulsão com Óleo de Semente de Abóbora em Linhagens de Células de Cancro da Mama. No campo da engenharia de tecidos, o Capítulo 6 descreve o desenvolvimento de Estruturas de Alginato/Colagénio Melhoradas com Nanopartículas Condutoras (PEDOT) para a regeneração de Vasos Sanguíneos de Pequeno Diâmetro. Finalmente, o Capítulo 7 expõe a Elaboração de um Gel Antisséptico Baseado em Compostos Bioativos Encapsulados em Nanopartículas.

Concluindo a nossa exploração, o eixo ***Soluções Nanotecnológicas para Remédios Ambientais,*** aborda a crise da contaminação da água. Este último capítulo descreve a Eliminação de Arsénico das Águas Subterrâneas Usando Nanopartículas de Ferro Reciclado, através do desenvolvimento de um filtro de baixo custo que utiliza nanopartículas de ferro.

Convidamo-lo a mergulhar na leitura de The Great World of Nanotechnology Vol. III, onde a ciência na escala mais pequena se traduz em soluções em grande escala. Esperamos sinceramente que esta compilação de pesquisas avançadas não só seja do seu interesse, mas também inspire novos rumos de estudo e aplicação neste campo infinitamente promissor.

Emilio Castro Otero

TABLE OF CONTENTS

FUNDAMENTALS OF NANOMATERIAL MANUFACTURING AND CHARACTERIZATION

NANOMATERIALS FOR SURFACE ENGINEERING AND SMART SENSORS

TABLE OF CONTENTS

CHAPTER 1

EFFECTS OF THE TRANSFER PROCESS ON THE STRUCTURE OF CVD-SYNTHESIZED GRAPHENE: A RAMAN SPECTROSCOPY STUDY

Data de submissão: 10/11/2025
Data de aceite: 24/11/2025

Rodrigo Segura-del-Río
Instituto de Química
Facultad de Ciencias
Universidad de Valparaíso
Valparaíso, Chile
https://orcid.org/0000-0003-0928-0021

Fernanda Olivares Salgado
Departamento de Física, Universidad Técnica
Federico Santa María
Valparaíso, Chile
https://orcid.org/0000-0002-9727-0677

Ricardo Henríquez Correa
Departamento de Física, Universidad Técnica
Federico Santa María
Valparaíso, Chile
https://orcid.org/0000-0001-5141-1676

ABSTRACT: In this chapter, a systematic investigation about the synthesis and transfer of graphene through the chemical vapor deposition (CVD) of methane (CH_4) and acetylene (C_2H_2) as the carbon precursors onto copper substrates is provided. Raman spectroscopy enabled the characterization of the number of layers, the level of disorder and the structural changes created by the transfer process to the silicon substrates. The findings indicate that CH_4 has more favorable effect on the growth of graphene films with reduced defect density and higher control of thickness than C_2H_2. Also, it was found out that the transfer creates effective reduction in the number of layers and changes in the relative intensities of the D, G and 2D bands, which is due to strain effects, interaction with the support polymer, and support polymer residues. These findings aid in shedding light on the processes that influence the mechanism of maintaining structural integrity of graphene in its processing and give a guideline to the manufacturing production of high-quality films to be used in electronic and photoelectrocatalytic tasks.
KEYWORDS: graphene; chemical vapor deposition; raman spectroscopy; graphene transfer.

1. INTRODUCTION

Graphene is a two-dimensional allotrope of carbon, formed by atoms arranged in a hexagonal network of only one atom in thickness. Since its isolation by Geim and Novoselov in 2004, research related to this material has increased drastically, and its relevance was recognized with the Nobel Prize in Physics in 2010. The electronic, thermal, and mechanical properties of graphene make it a material of high scientific and technological

interest. It stands out for its exceptional electrical conductivity (Martini et al., 2019), derived from its structure of sp^2 covalent bonds and delocalized π electrons, and for its high thermal conductivity, estimated between 3000 and 5000 $W \cdot m^{-1} \cdot K^{-1}$ (Ghosh et al., 2010), values that suggest that graphene conducts heat better than carbon nanotubes (Balandin et al., 2008). Its elastic modulus reaches 42 $N \cdot m^{-1}$, with a mechanical deformation of approximately 25% before breaking (Lee et al., 2008). Other significant properties are its large surface area (Liu et al., 2019) and its transparency (Nair et al., 2008). However, all these properties can vary significantly depending on the synthesis technique and the precursor used.

The techniques for obtaining graphene are divided into two main categories (Olabi et al., 2021). The first category includes methods in which graphite is used as the raw material. This category is called "top-down," which means "from top to bottom". In this category three methods can be distinguished, which are mechanical exfoliation (Gao et al., 2018), chemical exfoliation (Kamedulski et al., 2019), and chemical synthesis (Liu et al., 2008), the latter including the reduction of graphene oxide. From the exfoliation of graphite, a powder composed of graphene flakes is obtained, which is very convenient for experimental use in laboratories and for large-scale applications. The general limitation of these methods is that it is very difficult to obtain large-area material. In general, exfoliation methods starting from graphite are the simplest; however, during the process many defects are generated in the graphene sheets. Although defects can serve as active sites for electrochemical reactions, they also considerably decrease the performance of graphene's most notable properties, which are electrical and thermal conduction. The second category includes all methods in which a carbon source is used as a molecular or atomic precursor to generate graphene growth. This category is called "bottom-up," which means "from bottom to top," in the sense that graphene is built from atoms or small molecular fragments. The methods included in this section are pyrolysis (Karu et al., 1966), epitaxial growth (First et al., 2010), and CVD (Wei et al., 2009). Through epitaxial growth on SiC, high-quality graphene can be obtained. The two main drawbacks of this method are the high cost of SiC wafers and the high synthesis temperatures above 1000 °C. On the other hand, graphene synthesized by pyrolysis has a low cost and a highly pure material can be obtained. However, the number of defects observed in the graphene is high, so the properties of the material are not optimal. Finally, the CVD technique is the most convenient in terms of quality and price (Novoselov et al., 2012).

It is important to highlight that in the CVD technique any carbon source in solid, liquid, or gaseous state can be used as a synthesis precursor. But the most significant advantage compared to other techniques is that it allows controlling the number of

graphene layers by adjusting parameters such as temperature and synthesis time, and the amount of precursor. The number of graphene layers is one of the most important characteristics of this material, since, as mentioned earlier, the properties vary significantly between a monolayer and multilayer graphene. In addition, the presence of H_2 also plays an important role in the synthesis. Graphene can grow without H_2; however, this molecule has a catalytic effect that affects the growth mechanism (Qi et al., 2013).

On the other hand, the synthesis substrate plays a fundamental role in graphene growth. The most used substrates are transition metals such as nickel (Ni) (Yu et al., 2008), platinum (Pt), palladium (Pd) (Kwon et al., 2009), iridium (Ir) (Coraux et al., 2009), and copper (Cu) (Song et al., 2014). The disadvantage of Ni is the high percentage of carbon solubility. The solubility of carbon in the substrate must be optimal so that it is not difficult to transfer it to another substrate later. In addition, Ni is limited by its small grain size. This is important because, with larger grain size, the synthesized graphene exhibits larger areas without boundaries that can act as defects. On the other hand, substrates such as Pt, Pd, and Ir are quite costly. Cu is the best option currently because it has lower carbon solubility compared to Ni and a much lower cost than other transition metals (Zhang et al., 2011). In addition, its grain size can be increased through an annealing process. These characteristics make it possible to transfer graphene more easily from Cu than from other substrates (Li et al., 2009).

Finally, the synthesis precursor is very important, since the decomposition mechanism and subsequent formation of graphene vary depending on the chosen precursor molecule. The most used precursor is methane (CH_4). The decomposition mechanism of this molecule to form graphene has been described as successive dehydrogenation stages (Zhang et al., 2011). Another carbon source that can be used is acetylene (C_2H_2). This precursor is promising because it produces rapid graphene growth. In addition, it is possible to control the number of layers by adjusting the injection time with the CVD technique (Song et al., 2014). Graphene can grow without H_2; however, some authors indicate that it promotes the process with a catalytic effect. The properties of graphene and its atomic structure make it an ideal platform for synthesizing other carbon materials or materials of different nature. Graphene could improve the efficiency and durability of many applications. However, it is necessary to critically address its current limitations.

2. GRAPHENE SYNTHESIS AND TRANSFER

Graphene was synthesized on copper foils of 2.25 cm^2 (MTI, purity > 99.99%, thickness 25 µm), previously cleaned by ultrasound in ethanol and acetone for 5 min with

each solvent (Song et al., 2014; Segura et al., 2016). The CVD process was carried out in three stages. First, the substrate was annealed at the synthesis temperature for 20 min under a flow of 200 sccm of Ar/H_2 to increase the grain size of the Cu. Then, in the growth stage, the carbon precursor (CH_4 or C_2H_2) was injected with a constant flow of 2 sccm for variable intervals of 1 to 30 min, maintaining 200 sccm of Ar and adjusting the amount of H_2 between 0 and 100 sccm. Finally, the system was cooled to room temperature under Ar flow. To optimize the synthesis conditions, four fundamental parameters were evaluated: (i) deposition time (1–30 min), (ii) temperature (950, 1000, and 1050 °C), (iii) H_2 flow (0, 5, and 20 sccm), and (iv) precursor flow (1–10 sccm). The comparison between methane and acetylene allowed establishing their influence on the quality, number of layers, and uniformity of the graphene.

Subsequently, the graphene was transferred from the copper to the final substrate using a method assisted by polymethyl methacrylate (PMMA) (Suk et al., 2011). A total of 90 µL of a PMMA solution (20 mg/mL in chlorobenzene) was applied by spin-coating at 500 rpm for 10 s and 1500 rpm for 50 s, followed by curing at 120 ºC for 5 min. The Cu was dissolved in an aqueous solution of $Fe(NO_3)_3$ 1 M until complete removal, and the PMMA/graphene film was washed three times with distilled water. It was then transferred onto the new substrate and dried under vacuum for 2 h, followed by heating at 180 ºC for 30 min. The polymer was removed by successive immersion in acetone (40 ºC, 3 min) and 2-propanol (3 min), finishing with a thermal treatment at 400 °C under Ar/H_2 flow. The complete transfer procedure is shown schematically in Figure 1.

Figure 1. Schematic of the graphene transfer process.

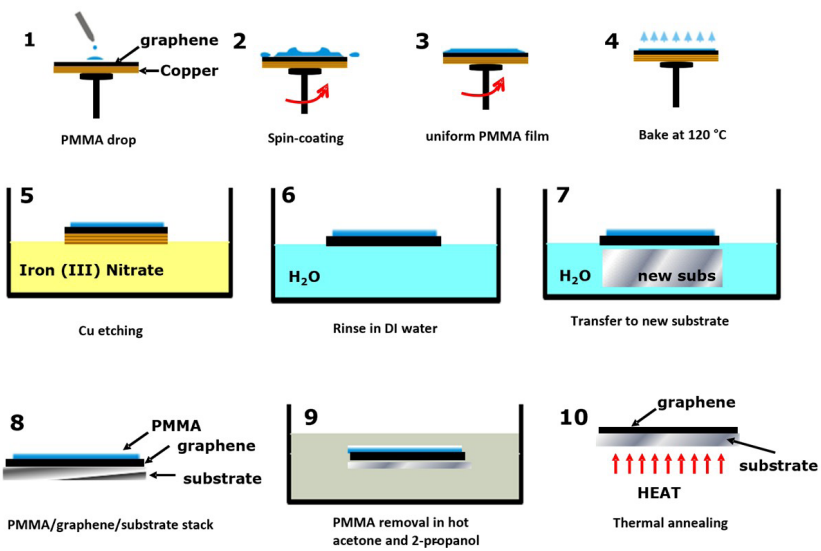

3. RESULTS

The synthesis of graphene on copper was optimized by CVD using two carbon precursors, acetylene and methane. For both, four main parameters were evaluated: (i) deposition time (1–30 min), (ii) temperature (950, 1000, and 1050 °C), (iii) hydrogen flow (0–100 sccm), and (iv) precursor flow (2–10 sccm).

The samples were characterized by Raman spectroscopy using a Renishaw inVia spectrometer with a 532 nm laser, to determine the number of layers and the degree of structural disorder. A 25× objective was used, and the laser intensity was kept at 5%. Ten spectra were collected from different regions of each sample and averaged, providing statistically representative data and minimizing the influence of local inhomogeneities or measurement artifacts. This technique is widely used to evaluate the quality of graphene, since it allows rapid and non-destructive identification of the number of layers, defects, and strain in the lattice (Saito et al., 2011; Pimenta et al., 2008). In the Raman spectra of graphene, the main bands distinguished are the D band (~1350 cm^{-1}), G band (~1580 cm^{-1}), and 2D band (~2690 cm^{-1}), occasionally accompanied by secondary signals such as D' (1620 cm^{-1}), G^+ (2450 cm^{-1}), and D+G (2940 cm^{-1}). The D band is associated with defects or grain boundaries and does not appear in pristine graphene. Its intensity increases with the defect density. The G band, originating from an in-plane vibrational mode (iTO and LO), is present in all types of graphene and its position is sensitive to strain or doping. The 2D band, corresponding to a second-order double-resonance process, is particularly useful for determining the number of layers: its shape and intensity change systematically with interlayer interaction (Malard et al., 2009). As the number of layers increases, the 2D band broadens and loses intensity, while the G band undergoes a slight shift to lower frequencies. In single-layer graphene, the 2D band is intense, symmetric, and narrow, with an I_{2D}/I_G intensity ratio > 2; in bilayers and few-layer graphene this value decreases progressively. Therefore, the I_{2D}/I_G ratio constitutes a direct criterion to estimate the number of layers and the structural quality of the material. The appearance and shape of the defect-induced bands (D, D', and D+G) also allow evaluation of the degree of crystalline order. In highly defective materials the D band increases notably, while in high-quality graphene this band is weak or absent. Raman spectroscopy offers an unequivocal, rapid, and non-destructive identification of single-layer, bilayer, and multilayer graphene, and is currently the most widely used method to characterize graphene (Ferrari et al., 2006; Ni et al., 2008). In this study, correlating the Raman response with the synthesis parameters enabled the

determination of optimal conditions for producing few-layer, low-defect graphene on copper. The following section presents the results obtained from this optimization.

3.1. EFFECT OF SYNTHESIS TIME

To analyze the effect caused by the precursor injection time, all fabrication parameters were kept constant while varying the time between 1 and 30 minutes, for the two proposed carbon sources (CH_4 and C_2H_2). The synthesis temperature used was 1000 ºC, the precursor flow 2 sccm, and the hydrogen flow 5 sccm. In Figure 2a, the Raman spectra for the samples prepared with CH_4 are presented. In this case, the ratio between the intensities of the 2D and G bands (I_{2D}/I_G) varies between 0.70 and 0.80, which corresponds approximately to 3 or 4 layers of graphene (Song et al., 2014). Despite increasing the time from 1 to 30 minutes, no significant difference is observed in the number of layers. Where a difference can be noticed is in the intensity of the D band. As the synthesis time increases, the intensity of this band decreases, which indicates a decrease in the number of defects. It is possible that by increasing the synthesis time, the molecules manage to form larger areas of material, and therefore the sample presents fewer grain boundaries and better-finished hexagonal structures. Therefore, in this case it is favorable to increase the synthesis time and obtain graphene sheets with better crystalline properties. On the other hand, in Figure 2b it can be noticed that in comparison with the syntheses performed with CH_4, the samples prepared with C_2H_2 do show an important difference when modifying the synthesis time. The 1-minute synthesis presents an I_{2D}/I_G ratio of 0.81, which corresponds approximately to 3 layers of graphene. Meanwhile, the 3- and 10-minute syntheses present ratios of 0.22 and 0.02 respectively, values that correspond to the formation of graphite.

Figure 2. Raman spectra for the graphene syntheses carried out by varying the precursor injection time a) methane and b) acetylene.

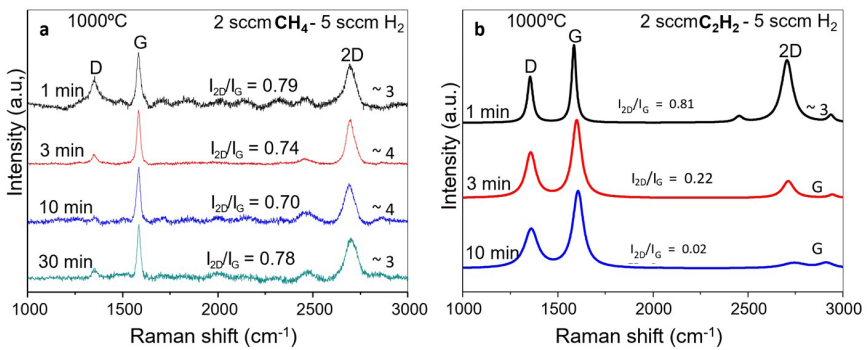

The difference observed between both precursors can be explained based on the molecular structure. It had previously been reported that C_2H_2 is a promising raw material because it produces a rapid growth of the graphene layers (Song et al., 2014). This makes sense if we consider that the CH_4 molecule has only one carbon atom, so it must join with another 5 carbon atoms to form a hexagon and break 4 C–H bonds to form the graphitic structure. On the other hand, C_2H_2 has two carbon atoms in its structure, so from 3 molecules a graphene hexagon can be formed. Under this context it is coherent that when increasing the synthesis time with CH_4 from 1 to 30 minutes practically the same number of layers is formed, while when using C_2H_2 the number of layers increases drastically.

3.2. EFFECT OF SYNTHESIS TEMPERATURE

In this section the effect of temperature on the synthesis of graphene was analyzed, keeping constant the other three parameters studied, which are the time, precursor flow, and hydrogen flow, for both CH_4 and C_2H_2. The synthesis time selected was 1 minute, and the precursor and hydrogen flow used was 3 and 5 sccm respectively. In Figure 3a the Raman spectra is presented for the samples prepared using CH_4. In this case, graphene of 4, 3, and 2 layers were obtained when the synthesis was carried out at 950 °C, 1000 °C, and 1050 °C respectively. That is, when increasing the synthesis temperature, the number of graphene layers decreases under the mentioned conditions. On the contrary, as can be seen in Figure 3b, when the synthesis is carried out with C_2H_2, the number of graphene layers increases when the temperature increases. Graphene of 3 and 5 layers was obtained when the synthesis temperature increased from 950 to 1000 ºC.

Figure 3. Raman spectra for the graphene syntheses carried out with a) methane and b) acetylene for different synthesis temperatures.

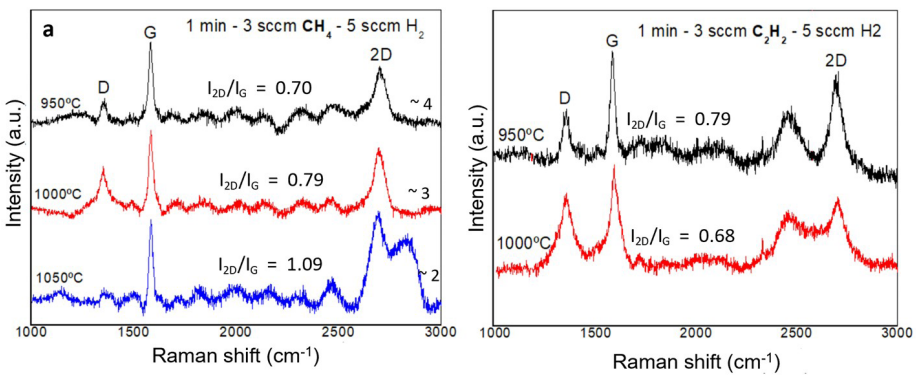

Again, in this section completely opposite phenomena are observed when comparing the two precursors. When increasing the synthesis temperature, the number of layers decreases if CH_4 is used and increases if C_2H_2 is used. It can also be observed that in the syntheses carried out with acetylene the intensity of the D band is higher, which indicates that the graphene sheets have more defects.

3.3. EFFECT OF PRECURSOR FLOW

To understand how the amount of precursor (CH_4 and C_2H_2) added in the synthesis of graphene affects the material, the synthesis time, temperature, and amount of hydrogen were kept constant. In Figure 4a the Raman spectra is presented for the samples synthesized with CH_4. For this precursor the injection flows selected were 3, 5, and 10 sccm. In the 3 spectra the ratio between the intensities of the I_{2D}/I_G bands varies around 0.60, which corresponds to approximately 5 or 6 layers of graphene. That is, when increasing the amount of precursor between 3 and 10 sccm it is not possible to notice a substantial difference in the number of layers. The D band also does not show significant changes in its intensity, and the presence of the other two disorder-related bands (D′ and D+G) is not appreciated. On the contrary, when using C_2H_2 as precursor a drastic variation occurs when increasing its injection flow. As can be seen in Figure 4b, when increasing the flow from 2 to 3 sccm only, the I_{2D}/I_G ratio varies from 0.81 to 0.71, that is, it increases from 3 to 4 layers with only 1 sccm difference. The above indicates that it is much more difficult to control the growth of this material using acetylene. On the other hand, it is also observed at first sight that the D band is much more intense in comparison with the spectra of the samples prepared with methane. In addition, the presence of another band produced by disorder, which is the D+G band, is observed. This indicates that the samples prepared with C_2H_2 present a greater number of defects than those prepared with CH_4. It is worth noting that the G+ band also appears to the left of the 2D band. However, in the literature there is still no clear consensus about the appearance of this band.

Figure 4. Raman spectra for the graphene syntheses with different amounts of flow of: a) methane and b) acetylene.

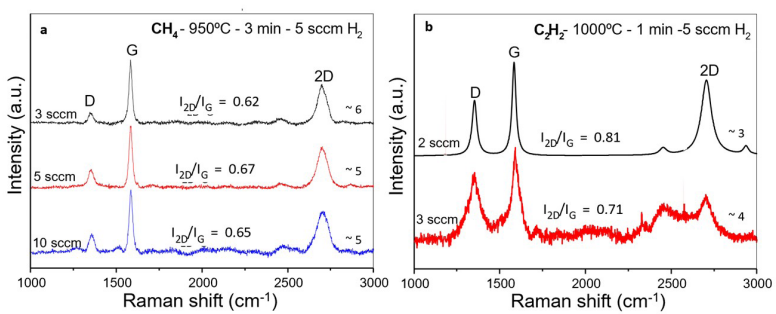

3.4. EFFECT OF HYDROGEN FLOW

In this section the effect of the hydrogen present in the synthesis of graphene was analyzed. The time, temperature, and precursor flow were kept constant. When analyzing how the amount of hydrogen affects the syntheses carried out with CH_4, it was found that with a lower amount of hydrogen a lower number of graphene layers is generated. As can be seen in Figure 5a, the synthesis prepared with 20 sccm of H_2 presents an I_{2D}/I_G ratio of 0.50, which corresponds to more than 8 layers. Meanwhile, the graphene synthesized without H_2 presents approximately 3 layers. In this case, if the objective is to obtain few-layer graphene, the most appropriate is to prepare it without H_2. However, it is probable that this graphene has a greater number of small grains. Hydrogen performs at least two functions in this synthesis (Vlassiouk et al., 2011). First, it acts as a catalyst for the activation of carbon through the dehydrogenation of methane and also participates in the control of grain size. This means that the presence of hydrogen allows the formation of larger grains, which improves the conductive properties of the material.

Similar to the synthesis carried out with CH_4, the syntheses carried out with C_2H_2 present a lower number of layers when decreasing the amount of hydrogen injected (Figure 5b). When adding 20 sccm of H_2 an I_{2D}/I_G ratio of 0.68 was obtained. Meanwhile, when adding 5 sccm of H_2 the I_{2D}/I_G ratio increases to 0.81 and consequently the number of layers decreases.

Figure 5. Raman spectra of graphene obtained using a) methane and b) acetylene with different amounts of hydrogen.

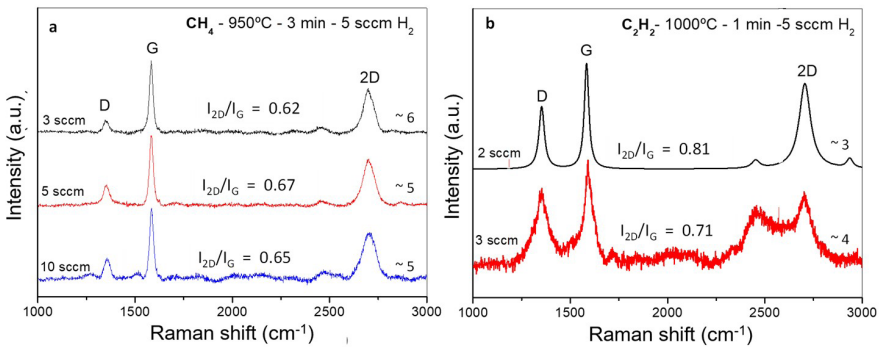

3.5. GRAPHENE TRANSFER AND SELECTION OF SYNTHESIS PARAMETERS

In this section the results obtained for the optimization of the transfer of graphene from the synthesis substrate (copper) to a new substrate are presented. For this study silicon was used as the transfer substrate and the procedure described previously

was employed. The analysis revealed that, when transferring the graphene samples, they undergo a kind of exfoliation during the process, as a result of the adhesion and release of the sheet on different surfaces until its final deposition. For this reason, when comparing the Raman spectra of graphene on copper and then on silicon, an increase in the I_{2D}/I_G ratio is observed, indicating a decrease in the number of layers (Figure 6). It is worth noting that, after the study of the synthesis of graphene, the optimal precursor and parameters were selected to facilitate the transfer and preserve its properties. As the optimal precursor CH_4 was chosen, since with C_2H_2 it is much more difficult to control the number of layers: small variations in its parameters completely modify the results. In contrast, with methane it is easier to maintain precise control of the thickness and reduce the number of structural defects. With respect to the synthesis parameters, these were selected considering the decrease in the number of layers that is produced by the exfoliation that the samples mentioned previously undergo. It was observed that, if in the synthesis graphene between 4 and 6 layers is obtained, which corresponds to an I_{2D}/I_G ratio between 0.60 and 0.70, then after the transfer the graphene presents 2 layers, as can be seen in Figure 6. Figure 6 shows 3 spectra of graphene synthesized on copper (black line) and also 3 spectra of the same graphene samples after the transfer onto silicon (red line). In Figure 6a the Raman spectra can be observed for a sample prepared for 3 minutes at 1000 °C. This sample on copper presented an I_{2D}/I_G ratio of 0.71 and then on silicon a ratio of 1.18. Initially the synthesized sample presented approximately 4 layers and after the transfer presents 2 layers. It is worth noting that when the I_{2D}/I_G ratio is close to 1, this corresponds to a graphene bilayer since both bands are equal. Meanwhile, in a spectrum of a monolayer of graphene the 2D band can be between 2 and 4 times larger than the G band. That is, the ratio between the intensities of these bands can also be between 2 and 4. In Figure 6b something very similar is observed. The graphene sample was prepared for 3 minutes at 950 °C. In this case the ratio between the intensities of the I_{2D}/I_G bands varies from 0.60 to 0.94. In number of layers these values correspond to 4–5 layers synthesized and 2 layers after the transfer. Then, in Figure 6c the spectrum can be observed for a sample prepared for 10 minutes at 950 °C. The ratio between the I_{2D}/I_G bands is 0.62 in the synthesis and 1.17 in the transfer. As in Figures 6a and 6b, in the synthesis approximately 5 layers are observed and then the transferred material corresponds to a graphene bilayer. An important difference observed when comparing all the spectra of the synthesized graphene with the transferred graphene is the increase of the G^+ band, which as mentioned previously appears at approximately 2450 cm^{-1} (Shimada et al., 2005). The origin of this band has been explained from different hypotheses by various authors which have been refuted over the years (Malard et al., 2009). Currently

there is still controversy about the assignment of this band (Saito et al., 2011). The reason is that there are different Raman DR (double resonance) components that occur at the same frequency, and it is still not clear which of them is responsible for the formation of this peak. On the contrary, the relative intensity of the Raman features associated with defects (for example, the D band) depends directly on the number of defects. In this case, however, the relative intensity of the bands associated with the Raman DR components varies from one sample to another. This band has also been studied in other sp^2 carbon materials such as carbon nanotubes (Shimada et al., 2005). Based on what was observed in this work, it could be inferred that the intensity of this band is affected by the transfer process, which could have to do with the substrate change or with the increase of the defects of the material. However, experimental and theoretical support is still needed to be able to correctly predict its behavior. Finally, it is important to highlight that the most recent bibliographic review studies on Raman spectroscopy of graphene do not mention anything about this peak, even though in the spectra they include, it does appear (Nanda et al., 2016).

Figure 6. Raman spectra of three graphene samples synthesized at different conditions on copper (black line) and then transferred to silicon (red line).

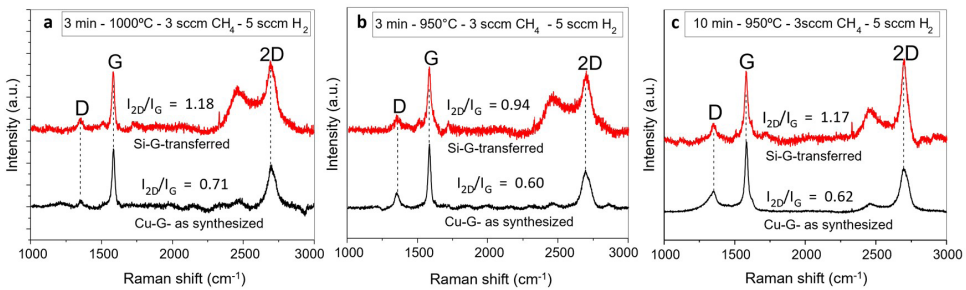

In general, to synthesize graphene with 4 to 6 layers it was possible to narrow the values for the 4 parameters studied in the synthesis. It is advisable to use the lowest possible precursor flow since the objective is to obtain few layers of material. This value is restricted by the minimum flow that the mass flow controller allows to be programmed. In this case the minimum value that can be programmed is 3 sccm. When adding a flow lower than 3 sccm the device error increases significantly. For this reason, 3 sccm was chosen as the optimal CH_4 flow. On the other hand, with respect to the H_2 flow, by consensus between the results obtained and the information found in the literature it was concluded that it is possible to synthesize graphene in the absence of H_2. However, the most advisable is to add a small amount so that the synthesized material presents better structural properties, lower number of defects, and grains of larger area. Therefore, it was

decided to add 5 sccm of hydrogen in all the syntheses. With respect to the synthesis time, the best results were obtained with 3 and 10 minutes. However, it was decided that the most adequate synthesis time is 10 minutes since the number of layers formed is the same as when using 3 minutes, but the sheets may be better finished and with fewer defects. Finally, as synthesis temperature 950 °C or 1000 °C can be used. With both temperatures in combination with the parameters mentioned previously graphene between 4 and 6 layers can be obtained to subsequently transfer it. Lastly, it is important to highlight again that to achieve an efficient transfer of 1 to 2 layers of graphene it is advisable to prepare a sample that presents 4 to 6 layers on the original substrate.

4. CONCLUSIONS

In this work the synthesis of graphene by CVD on copper was systematically investigated employing two carbon precursors (CH_4 and C_2H_2) and varying synthesis time, temperature, precursor flow, and hydrogen. It was found that methane (CH_4) allows a more reproducible control of the number of layers and leads to sheets with a lower density of defects in comparison with acetylene (C_2H_2), which favors rapid growth but is difficult to control and presents greater structural disorder. The transfer process (PMMA + Cu etch) induces an effective reduction of the number of layers (4–6 layers on Cu → 1–2 layers after transfer) and modifies Raman characteristics associated with double resonances, which suggests that partial exfoliation, the effect of the substrate, and PMMA residues influence the observed spectroscopy. From the optimizations, the recommended working condition is: CH_4 at 950–1000 °C, minimum compatible precursor flow (3 sccm in the system used), 5 sccm of H_2, and a time of 10 min to obtain transferable sheets of 1–2 layers after transfer. Finally, to strengthen the results and move toward applications, it is necessary to complement this study with TEM/AFM characterization of edges, and a post-transfer cleaning protocol that reduces PMMA residues and process variability.

REFERENCES

Balandin, A. A., Ghosh, S., Bao, W., Calizo, I., Teweldebrhan, D., Miao, F., & Lau, C. N. (2008). Superior thermal conductivity of single-layer graphene. Nano Letters, 8(3), 902–907. https://doi.org/10.1021/nl0731872

Coraux, J., N'Diaye, A. T., Engler, M., Busse, C., Wall, D., Buckanie, N., Meyer zu Heringdorf, F. J., Van Gastel, R., Poelsema, B., & Michely, T. (2009). Growth of graphene on Ir(111). New Journal of Physics, 11, Article 023006. https://doi.org/10.1088/1367-2630/11/2/023006

Ferrari, A. C., Meyer, J. C., Scardaci, V., Casiraghi, C., Lazzeri, M., Mauri, F., Piscanec, S., Jiang, D., Novoselov, K. S., Roth, S., & Geim, A. K. (2006). Raman spectrum of graphene and graphene layers. Physical Review Letters, 97(18), Article 187401. https://doi.org/10.1103/PhysRevLett.97.187401

First, P. N., de Heer, W. A., Seyller, T., Berger, C., Joseph, A., & Moon, J. (2010). Epitaxial graphenes on silicon carbide. MRS Bulletin, 35(4), 296–305. https://doi.org/10.1557/mrs2010.552

Gao, E., Lin, S. Z., Qin, Z., Buehler, M. J., Feng, X. Q., & Xu, Z. (2018). Mechanical exfoliation of two-dimensional materials. Journal of the Mechanics and Physics of Solids, 115, 248–262. https://doi.org/10.1016/j.jmps.2018.03.014

Ghosh, S., Bao, W., Nika, D. L., Subrina, S., Pokatilov, E. P., Lau, C. N., & Balandin, A. A. (2010). Dimensional crossover of thermal transport in few-layer graphene. Nature Materials, 9(7), 555–558. https://doi.org/10.1038/nmat2753

Güler, Ö., & Bağci, N. (2020). A short review on mechanical properties of graphene reinforced metal matrix composites. Journal of Materials Research and Technology, 9(6), 6808–6833. https://doi.org/10.1016/j.jmrt.2020.01.077

Kamedulski, P., Ilnicka, A., Łukaszewicz, J. P., & Skorupska, M. (2019). Highly effective three-dimensional functionalization of graphite to graphene by wet chemical exfoliation methods. Adsorption, 25(3), 631–638. https://doi.org/10.1007/s10450-019-00067-9

Karu, A. E., & Beer, M. (1966). Pyrolytic formation of highly crystalline graphite films. Journal of Applied Physics, 37(5), 2179–2181. https://doi.org/10.1063/1.1708759

Kwon, S. Y., Ciobanu, C. V., Petrova, V., Shenoy, V. B., Bareño, J., Gambin, V., Petrov, I., & Kodambaka, S. (2009). Growth of semiconducting graphene on palladium. Nano Letters, 9(12), 3985–3990. https://doi.org/10.1021/nl902140j

Lee, C., Wei, X., Kysar, J. W., & Hone, J. (2008). Measurement of the elastic properties and intrinsic strength of monolayer graphene. Science, 321(5887), 385–388. https://doi.org/10.1126/science.1157996

Li, X., Cai, W., An, J., Kim, S., Nah, J., Yang, D., Piner, R., Velamakanni, A., Jung, I., Tutuc, E., Banerjee, S. K., Colombo, L., & Ruoff, R. S. (2009). Large-area synthesis of high-quality and uniform graphene films on copper foils. Science, 324(5932), 1312–1314. https://doi.org/10.1126/science.1171245

Liu, M., Zhang, X., Wu, W., Liu, T., Liu, Y., Guo, B., & Zhang, R. (2019). One-step chemical exfoliation of graphite to ~100% few-layer graphene with high quality and large size at ambient temperature. Chemical Engineering Journal, 355, 181–185. https://doi.org/10.1016/j.cej.2018.08.146

Liu, N., Luo, F., Wu, H., Liu, Y., Zhang, C., & Chen, J. (2008). One-step ionic-liquid-assisted electrochemical synthesis of ionic-liquid-functionalized graphene sheets directly from graphite. Advanced Functional Materials, 18(10), 1518–1525. https://doi.org/10.1002/adfm.200700797

Malard, L. M., Pimenta, M. A., Dresselhaus, G., & Dresselhaus, M. S. (2009). Raman spectroscopy in graphene. Physics Reports, 473(5–6), 51–87. https://doi.org/10.1016/j.physrep.2009.02.003

Martini, L., Chen, Z., Mishra, N., Barin, G. B., Fantuzzi, P., Ruffieux, P., Fasel, R., Feng, X., Narita, A., Coletti, C., Müllen, K., & Candini, A. (2019). Structure-dependent electrical properties of graphene nanoribbon devices with graphene electrodes. Carbon, 146, 36–43. https://doi.org/10.1016/j.carbon.2019.01.071

Nair, R. R., Blake, P., Grigorenko, A. N., Novoselov, K. S., Booth, T. J., Stauber, T., Peres, N. M. R., & Geim, A. K. (2008). Fine structure constant defines visual transparency of graphene. Science, 320(5881), 1308. https://doi.org/10.1126/science.1156965

Nanda, S. S., Kim, M. J., Yeom, K. S., An, S. S. A., Ju, H., & Yi, D. K. (2016). Raman spectrum of graphene with its versatile future perspectives. TrAC Trends in Analytical Chemistry, 80, 125–131. https://doi.org/10.1016/j.trac.2016.02.024

Ni, Z., Wang, Y., Yu, T., & Shen, Z. (2008). Raman spectroscopy and imaging of graphene. Nano Research, 1(4), 273–291. https://doi.org/10.1007/s12274-008-8036-1

Novoselov, K. S., Fal'ko, V. I., Colombo, L., Gellert, P. R., Schwab, M. G., & Kim, K. (2012). A roadmap for graphene. Nature, 490(7419), 192–200. https://doi.org/10.1038/nature11458

Olabi, A. G., Ali, M., Wilberforce, T., & Taha, E. (2021). Application of graphene in energy storage device – A review. Renewable and Sustainable Energy Reviews, 135, 110026. https://doi.org/10.1016/j.rser.2020.110026

Pimenta, M. A.; Dresselhaus, G.; Dresselhaus, M. S.; Cançado, L. G.; Jorio, A.; Saito, R. (2007). Studying Disorder in Graphite-Based Systems by Raman Spectroscopy. Phys. Chem. Chem. Phys. 9 (11), 1276–1291. https://doi.org/10.1039/b613962k

Qi, M., Ren, Z., Jiao, Y., Zhou, Y., Xu, X., Li, W., Li, J., Zheng, X., & Bai, J. (2013). Hydrogen kinetics on scalable graphene growth by atmospheric pressure chemical vapor deposition with acetylene. Journal of Physical Chemistry C, 117(27), 14348–14353. https://doi.org/10.1021/jp403410b

Saito, K., Nakamura, J., & Natori, A. (2007). Ballistic thermal conductance of a graphene sheet. Physical Review B, 76(11), 1–4. https://doi.org/10.1103/PhysRevB.76.115409

Saito, R., Hofmann, M., Dresselhaus, G., Jorio, A., & Dresselhaus, M. S. (2011). Raman spectroscopy of graphene and carbon nanotubes. Advances in Physics, 60(3), 413–550. https://doi.org/10.1080/00018732.2011.582251

Segura, R. A., Olivares, F., Maze, J., Häberle, P., Henríquez, R. (2016). Photoelectrochemical Activity of Graphene Supported Titanium Dioxide. Journal of Nanomaterials, 7914189, 1-6. http://dx.doi.org/10.1155/2016/7914189

Shimada, T., Sugai, T., Fantini, C., Souza, M., Cançado, L. G., Jorio, A., Pimenta, M. A., Saito, R., Grüneis, A., Dresselhaus, G., Dresselhaus, M. S., Ohno, Y., Mizutani, T., & Shinohara, H. (2005). Origin of the 2450 cm−1 Raman bands in HOPG, single-wall and double-wall carbon nanotubes. Carbon, 43(5), 1049–1054. https://doi.org/10.1016/j.carbon.2004.11.044

Song, W., Jeon, C., Kim, S. Y., Kim, Y., Kim, S. H., Lee, S. I., Jung, D. S., Jung, M. W., An, K. S., & Park, C. Y. (2014). Two selective growth modes for graphene on a Cu substrate using thermal chemical vapor deposition. Carbon, 68, 87–94. https://doi.org/10.1016/j.carbon.2013.10.039

Suk, J. W., Kitt, A., Magnuson, C. W., Hao, Y., Ahmed, S., An, J., Swan, A. K., Goldberg, B. B., & Ruoff, R. S. (2011). Transfer of CVD-grown monolayer graphene onto arbitrary substrates. ACS Nano, 5(9), 6916–6924. https://doi.org/10.1021/nn201207c

Vlassiouk, I., Regmi, M., Fulvio, P., Dai, S., Datskos, P., Eres, G., & Smirnov, S. (2011). Role of hydrogen in chemical vapor deposition growth of large single-crystal graphene. ACS Nano, 5(7), 6069–6076. https://doi.org/10.1021/nn201978y

Wei, D., Liu, Y., Wang, Y., Zhang, H., Huang, L., & Yu, G. (2009). Synthesis of N-doped graphene by chemical vapor deposition and its electrical properties. Nano Letters, 9(5), 1752–1758. https://doi.org/10.1021/nl803279t

Yu, Q., Lian, J., Siriponglert, S., Li, H., Chen, Y. P., & Pei, S. S. (2008). Graphene segregated on Ni surfaces and transferred to insulators. Applied Physics Letters, 93(11), 1–4. https://doi.org/10.1063/1.2982585

Zhang, W., Wu, P., Li, Z., & Yang, J. (2011). First-principles thermodynamics of graphene growth on Cu surfaces. Journal of Physical Chemistry C, 115(36), 17782–17787. https://doi.org/10.1021/jp2006827

CHAPTER 2

NANOFIBRAS POLIMÉRICAS POR FIAÇÃO POR SOPRO EM SOLUÇÃO VIA AEROGRAFIA: UMA REVISÃO DAS PROPRIEDADES, VANTAGENS TECNOLÓGICAS E APLICAÇÕES EMERGENTES

Data de aceite: 10/12/2025

Gabriel da Cruz Dias[1]
Universidade Estadual de Maringá (UEM)
Campus Regional de Goioerê (CRG)
Departamento de Ciências
Goioerê, Paraná, Brasil
http://lattes.cnpq.br/1579632987794997

Thelma Sley Pacheco Cellet
Universidade Estadual de Maringá (UEM)
Campus Regional de Goioerê (CRG)
Departamento de Ciências
Goioerê, Paraná, Brasil
http://lattes.cnpq.br/5607888729834715

Mirian Cristina dos Santos
Universidade Estadual Paulista Júlio de Mesquita Filho (UNESP)
Campus Araraquara, Instituto de Química
Departamento de Química Analítica
Físico-Química e Inorgânica
Araraquara, São Paulo, Brasil
http://lattes.cnpq.br/1792298807472521

Caroline Silva Danna
Universidad Austral de Chile
Facultad de Ciencias de la Ingeniería
Instituto de Ingeniería Mecánica
Valdivia, Chile
http://lattes.cnpq.br/0095733632562421

Paulo Roberto Orlandi Ruiz
Universidade Estadual Paulista Júlio de Mesquita Filho (UNESP)
Faculdade de Ciências e Tecnologia
Departamento de Física
Presidente Prudente, São Paulo, Brasil
http://lattes.cnpq.br/6643374948010201

Deuber Lincon Agostini da Silva
Universidade Estadual Paulista Júlio de Mesquita Filho (UNESP)
Faculdade de Ciências e Tecnologia
Departamento de Física
Presidente Prudente, São Paulo, Brasil
http://lattes.cnpq.br/8933884950667644

Clarissa de Almeida Olivati
Universidade Estadual Paulista Júlio de Mesquita Filho (UNESP)
Faculdade de Ciências e Tecnologia
Departamento de Física
Presidente Prudente, São Paulo, Brasil
http://lattes.cnpq.br/9822212808651415

RESUMO: A otimização de nanofibras poliméricas tem recebido atenção substancial devido à sua elevada área superficial, porosidade aumentada e excelente desempenho mecânico, características que possibilitam aplicações em nanocompósitos, sensores ópticos, liberação controlada de fármacos, engenharia de tecidos, geração de energia e tratamento de água. Tradicionalmente, a eletrofiação tem sido

[1] Autor correspondente.

a técnica dominante para a produção de nanofibras, embora apresente limitações relacionadas à necessidade de altas tensões e à baixa taxa de produção. Para superar essas restrições, foi desenvolvida a técnica de Fiação por Sopro de Solução (FSS), do inglês Solution Blow Spinning (SBS), que utiliza gás pressurizado como força motriz e alcança taxas de produção de 10 a 30 vezes superiores às da eletrofiação. Esforços recentes têm se concentrado na adaptação da FSS por meio da aerografia, utilizando aerógrafos comerciais de baixo custo capazes de depositar fibras rapidamente em diversos tipos de substratos. Esta revisão discute a evolução das metodologias de fabricação de nanofibras, com ênfase no mecanismo FSS/aerografia, suas vantagens e as tendências atuais de pesquisa, destacando especialmente seu papel emergente no desenvolvimento de membranas para purificação de água e remediação ambiental.
PALAVRAS-CHAVE: nanofibras; fiação por sopro em solução; aerografia; propriedades poliméricas; tratamento de água.

POLYMERIC NANOFIBERS BY SOLUTION BLOW SPINNING VIA AIRBRUSHING: A REVIEW OF PROPERTIES, TECHNOLOGICAL ADVANTAGES AND EMERGING APPLICATIONS

ABSTRACT: The optimization of polymer nanofibers has garnered substantial attention due to their high surface area, elevated porosity, and excellent mechanical performance, enabling applications in nanocomposites, optical sensing, controlled drug delivery, tissue engineering, energy harvesting, and water treatment. Traditionally, electrospinning has been the dominant technique for nanofiber production, yet it is limited by high voltage requirements and low throughput. To overcome these constraints, Solution Blow Spinning (SBS), known in Portuguese as Fiação por Sopro em Solução (FSS), was developed, employing pressurized gas as the driving force and achieving production rates 10–30 times higher than electrospinning. Recent efforts have focused on adapting SBS through airbrushing, using low-cost commercial airbrush systems capable of rapidly depositing fibers onto diverse substrates. This review discusses the evolution of nanofiber fabrication methods, emphasizing the SBS/airbrushing mechanism, its advantages, and current research trends, particularly its emerging role in the development of membranes for water purification and environmental remediation.
KEYWORDS: nanofibers; solution blow spinning; airbrushing; polymer properties; water treatment.

1. APRESENTAÇÃO

A crescente liberação de efluentes contendo contaminantes tóxicos em decorrência das atividades humanas configura uma preocupação socioambiental significativa na atualidade. Diversos compostos utilizados na agropecuária, na agricultura e em processos industriais de alta tecnologia acabam dissolvidos nos corpos hídricos, sendo de difícil separação. Esse cenário favorece a disseminação de poluentes orgânicos e inorgânicos que podem atingir a cadeia alimentar e, consequentemente, representar riscos à saúde humana.

Entre esses contaminantes, destacam-se corantes, herbicidas, pesticidas e íons metálicos, cuja presença em ambientes aquáticos vem gerando alerta crescente, dado seu impacto direto na qualidade da água e na saúde pública. Particular atenção é direcionada aos efluentes da indústria têxtil: corantes e demais compostos tóxicos podem alcançar os lençóis freáticos e interferir em processos ecológicos, como a penetração de radiação solar, afetando organismos aquáticos e potencialmente acumulando-se em níveis superiores da cadeia alimentar. Diante desse cenário, torna-se essencial o desenvolvimento de tecnologias eficientes para a remoção desses poluentes.

O presente trabalho tem como objetivo investigar a produção de nanofibras poliméricas por meio da técnica de Fiação por Sopro em Solução (FSS), com ênfase na adaptação do processo para sistemas de aerografia utilizando aerógrafos comerciais. A análise concentra-se nos fundamentos fluidodinâmicos e nos mecanismos de estiramento e solidificação da solução polimérica sob fluxo de ar pressurizado, bem como na influência dos parâmetros operacionais decorrentes do uso de bicos de aerógrafo.

A crescente demanda por nanomateriais com elevada área superficial, alta porosidade e excelentes propriedades mecânicas tem impulsionado pesquisas em nanofibras para aplicações em diversas áreas, incluindo engenharia de tecidos, liberação controlada de fármacos, sensores, geração e armazenamento de energia, como reforço de compósitos e, especialmente, no tratamento de água e efluentes.

Historicamente, a técnica de eletrofiação consolidou-se como o método pioneiro para obtenção de nanofibras. No entanto, suas limitações como a necessidade de altas tensões elétricas, baixa produtividade e restrições ao uso em superfícies vivas ou irregulares motivaram o desenvolvimento de alternativas tecnológicas. Nesse contexto, a FSS surge como método promissor, uma vez que utiliza gás pressurizado como força motriz, elimina a dependência de campo elétrico e permite taxas de produção até dez vezes maiores que as obtidas pela eletrofiação tradicional.

A adaptação da FSS via aerografia, tema central desta revisão, apresenta vantagens significativas: simplicidade operacional, baixo custo, grande disponibilidade comercial dos dispositivos, elevada versatilidade e possibilidade de deposição direta sobre substratos planos, irregulares ou biológicos. Estudos recentes demonstram que essa abordagem permite a obtenção de nanofibras com excelentes propriedades morfológicas e funcionais, incluindo a manutenção de fases cristalográficas em determinados polímeros, característica frequentemente comprometida em processos de eletrofiação devido às intensas forças eletrostáticas envolvidas.

Neste Sentido, o mesmo reúne os fundamentos físicos e químicos da técnica, discute parâmetros críticos do processo (pressão, concentração, viscosidade, distância de trabalho), apresenta resultados consolidados na literatura e evidencia o potencial crescente da aerografia como rota rápida, simples e acessível para a produção de nanofibras. A partir dessa análise, busca-se destacar o avanço tecnológico proporcionado por essa metodologia, bem como suas perspectivas de aplicação em áreas emergentes, especialmente no tratamento de água.

2. NANOFIBRAS POLIMÉRICAS: PROPRIEDADES E APLICAÇÕES

A produção e o estudo de nanofibras poliméricas têm ganhado destaque na área de materiais devido ao conjunto de funcionalidades que emergem quando polímeros naturais ou sintéticos são estruturados em escala nanométrica. Além das características já consolidadas, como elevada área específica e porosidade intrínseca resultante da interconectividade da rede formada, essas arquiteturas possibilitam maior capacidade de incorporação de agentes ativos e melhorias significativas no desempenho mecânico, ampliando sua aplicabilidade em diferentes tecnologias.

Entre as principais aplicações, destacam-se seu uso em filtros e membranas de separação empregadas em processos de adsorção, ultrafiltração e destilação. Na área da saúde, as nanofibras têm sido exploradas em sistemas de liberação controlada de fármacos, na engenharia de tecidos, além do desenvolvimento de selantes cirúrgicos. Outras frentes de aplicação incluem sua utilização como fase de reforço em nanocompósitos, em sensores ópticos, em tecnologias de geração e armazenamento de energia e em dispositivos nanoestruturados de alta funcionalidade.

Estudos recentes evidenciam o crescente interesse em materiais voltados ao tratamento de efluentes, destacando-se, por exemplo, nanofibras termoplásticas como alternativas promissoras para membranas de destilação devido à boa estabilidade térmica e alta porosidade. Além disso, a incorporação de nanomateriais em nanofibras obtidas via FSS demonstra grande potencial para o desenvolvimento de materiais com capacidades aprimoradas de adsorção.

Figura 1. Sínteses e aplicações emergentes relacionadas às nanofibras poliméricas.

Fonte: Adaptado de Kenry & ChweeTeck Lim (2017).

3. O DESENVOLVIMENTO DA METODOLOGIA DE OBTENÇÃO DE NANOFIBRAS

Eletrofiação (Electrospinning)

A eletrofiação é o método de referência dominante para a produção de nanofibras em escala laboratorial, baseado na ejeção de um jato de solução polimérica ou polímero fundido sob a influência de um campo eletrostático de alta intensidade, resultando na deposição controlada das fibras sobre um coletor aterrado.

À medida que a diferença de potencial aumenta, a gota da solução se alonga e forma o Cone de Taylor, momento em que as interações eletrostáticas superam a tensão superficial e dão origem a um jato que se desloca em direção ao coletor. Embora eficiente, a técnica apresenta limitações significativas, o que inviabiliza sua aplicação direta em tecidos vivos, além de operar com baixas velocidades e baixa eficiência em processos de grande escala, elevando seus custos.

Soma-se a isso a limitação relacionada ao uso de solventes que não interagem adequadamente com o campo elétrico, o que restringe ainda mais suas possibilidades de aplicação.

Figura 2. Esquema utilizado em experimentos de eletrofiação.

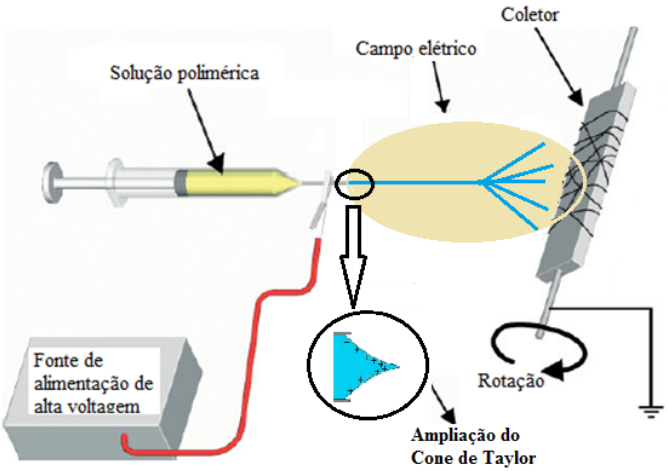

Fonte: Adptado de Martins, A.; Araujo, J. V.; Reis, R. L.; Neves, N. M (2007).

Fiação por Sopro em Solução (FSS)

A técnica de Fiação por Sopro em Solução (FSS), desenvolvida por Medeiros e colaboradores, surgiu como alternativa para superar limitações da eletrofiação, em especial a dependência de tensões elétricas elevadas. Seu funcionamento baseia-se na utilização de dois fluxos concêntricos: um contendo a solução polimérica e outro composto por um gás pressurizado (ar, nitrogênio ou argônio), que atua como força motriz responsável pelo estiramento e pela aceleração do jato polimérico.

Ao deixar o bocal externo, o gás sofre uma rápida redução de pressão ao entrar em contato com a pressão atmosférica, o que aumenta sua velocidade de escoamento e provoca uma queda de pressão no centro do jato; essa diferença gera a força motriz responsável por acelerar o fluido polimérico.

A alta velocidade do gás também induz cisalhamento na interface gás/solução, superando a tensão superficial da gota e promovendo o estiramento do polímero até a formação de micro e nanofibras. A FSS tem se mostrado eficiente para a fiação de diversos polímeros comuns à eletrofiação, como poliestireno, polimetil-metacrilato e poliácido láctico, alcançando taxas de alimentação significativamente superiores às típicas da eletrofiação.

Figura 3. Esquema experimental da FSS.

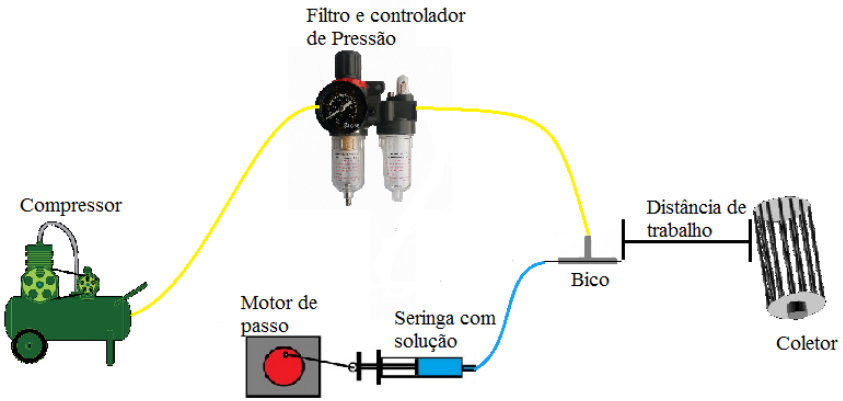

Fonte: Reirado de Zadorosny, L. (2017).

4. AEROGRAFIA: UMA ADAPTAÇÃO PROMISSORA DA FSS

O conceito de aerografia, baseado na pulverização de soluções, remonta à pré-história, como evidenciado em pinturas rupestres, embora o dispositivo moderno tenha sido inventado apenas em 1879 por Francis Edgar Stanley e posteriormente aprimorado por Charles Burdick, cujo design serviu de base para os aerógrafos profissionais atuais.

O aerógrafo funciona pela mistura de ar comprimido com tinta ou solução polimérica, gerando um jato direcionado ao substrato. Sua classificação considera dois aspectos principais: o tipo de mistura e o tipo de acionamento. Quanto à mistura, o aerógrafo pode ser do tipo externo, em que ar e solução se combinam apenas na saída do bico, adequado para aplicações mais amplas, ou interno, no qual a mistura ocorre dentro do corpo do dispositivo, permitindo maior uniformidade do jato e traços mais finos. Quanto ao acionamento, os modelos podem ser de ação simples, em que o gatilho controla apenas o fluxo de ar, exigindo ajuste independente do fluido, ou de dupla ação, que possibilita regular simultaneamente ar e solução, conferindo maior precisão e controle sobre a formação do jato.

A adaptação do aerógrafo comercial para a técnica de FSS tem se mostrado promissora quando comparada à eletrofiação, apresentando vantagens como ampla disponibilidade dos dispositivos, altas taxas de produção, baixo custo operacional, versatilidade de manuseio, possibilidade de deposição das fibras sobre qualquer tipo de superfície, inclusive *in vivo*, uma vez que o processo utiliza apenas gás comprimido. e obtenção de nanofibras com elevada porosidade e menores diâmetros.

Entretanto, limitações como a impossibilidade de controlar a taxa de alimentação da solução, a necessidade de concentrações menores, ocorrência de entupimentos por altas viscosidades e restrições de pressão estabelecidas pelo fabricante ainda representam desafios.

A morfologia das nanofibras obtidas por aerografia depende de forma crítica de parâmetros como concentração da solução, pressão do gás e distância de trabalho: Concentrações poliméricas baixas resultam em fibras defeituosas, devido à evaporação insuficiente do solvente, enquanto concentrações elevadas aumentam a viscosidade e o risco de obstrução aumenta. Como a pressão atua como força motriz, pressões maiores geraram aglomerados, e por fim, distâncias curtas entre o bocal e o coletor impedem a completa evaporação do solvente, causando aderência indesejada, enquanto distâncias muito grandes reduzem a quantidade de material que efetivamente atinge o coletor.]

Figura 4. Fotografia digital de aerógrafo comercial; (a) detalhes do bico, (b) estrutura e (c) detalhes do reservatório.

Fonte: Retirado de DIAS e colaboradores (2019).

5. APLICAÇÕES E TRABALHOS RELACIONADOS: UM BREVE EXEMPLO

A versatilidade da aerografia tem permitido sua aplicação em diferentes áreas antes dominadas pela eletrofiação, destacando-se especialmente sua eficiência em procedimentos *in situ* sobre tecidos vivos, algo inviável na técnica eletrofiada.

Estudos da literatura avaliaram a viabilidade da blenda polimérica de poli(ácido lático-co-glicólico) (PLGA) e polietilenoglicol (PEG), obtida pela técnica de fiação por sopro em solução (FSS), como selante cirúrgico para anastomoses intestinais em dois modelos pré-clínicos. No primeiro, camundongos foram submetidos a transecção parcial do ceco sem suturas, e a FSS foi comparada a três selantes comerciais, cola de fibrina, hidrogel de PEG e cianoacrilato quanto à capacidade de vedação, pressão de ruptura e taxa de sobrevivência. Os resultados evidenciaram que a FSS promoveu pressões de ruptura significativamente mais elevadas e melhorou as taxas de sobrevivência dos

animais em relação aos grupos tratados com cola de fibrina e hidrogel de PEG, alcançando desempenho comparável ao cianoacrilato.

Na etapa seguinte, a FSS foi aplicada como reforço de uma anastomose suturada do intestino delgado em um modelo pré-clínico de leitões. Nesse cenário, todos os animais sobreviveram por 14 dias, sem ocorrência de vazamentos anastomóticos. A aplicação da FSS também resultou em aumento expressivo da pressão de ruptura, quase quatro vezes maior, quando comparada ao segmento apenas suturado.

Do ponto de vista de aplicabilidade clínica, a FSS apresentou manuseio simples e controlado, podendo ser aplicada com um aerógrafo convencional, aderindo adequadamente a tecidos ligeiramente úmidos e permitindo remoção fácil quando depositada em excesso. Em contraste, alguns selantes comerciais mostraram maior dificuldade de aplicação ou induziram respostas inflamatórias mais intensas.

Em conjunto, esses resultados consolidam a FSS como uma alternativa promissora para o reforço de anastomoses gastrointestinais, combinando desempenho mecânico superior, boa aplicabilidade cirúrgica e potencial translacional relevante, um panorama geral da possibilidade de trabalhos é apresentado nos trabalhos de Kern, N.G, Behrens A. M, Srinivasan P, Rossi, C.T., Daristotle, J.L, Kofinas, P. Sandler A. D (2017).

A técnica de FSS/Aerografia também tem se mostrado eficaz na produção de compósitos, permitindo a incorporação uniforme de nanopartículas e em aplicações em células solares.

Neste sentido, a literatura tem demonstrado avanços significativos na utilização de técnicas de deposição por spray, utilizando aerógrafos para a fabricação de dispositivos fotovoltaicos orgânicos. Nesse contexto, destaca-se o estudo que investigou a produção de células solares de hetero junção em massa utilizando a blenda P3HT (poli(3-hexiltiofeno)): PCBM ([6,6]-fenil-C_{61}-butirato de metil-éster) como camada ativa. O uso do aerógrafo para deposição desse filme polimérico mostrou-se uma alternativa atraente aos métodos tradicionais, por permitir processamento de baixo custo, aplicação sobre áreas extensas e compatibilidade com tecnologias de produção em larga escala, como impressão e revestimento contínuo.

A eficiência do processo depende fortemente do controle preciso dos parâmetros de deposição, os quais foram sistematicamente avaliados no estudo em questão. Entre eles, destacaram-se temperatura do substrato, otimizada em 40 °C, distância de pulverização de aproximadamente 17 cm, e a escolha de uma mistura de co-solventes, constituída por orto-diclorobenzeno e clorobenzeno na proporção 1:5, responsável por melhorar a uniformidade e reduzir defeitos morfológicos durante a formação do filme.

Os dispositivos fabricados nessas condições alcançaram eficiência de conversão de energia de 4,1%, com camada ativa de espessura média de 270 nm, apresentando morfologia adequada ao transporte de cargas, ainda que com rugosidade superior à de filmes produzidos por spin-coating. Esses resultados evidenciam que o spray-coating constitui uma técnica eficaz e potencialmente competitiva em relação aos métodos tradicionais, tanto em qualidade de filme quanto em desempenho fotovoltaico, como apresentado no trabalho de Susanna G., Salamandra, L., Brown, T. M., di Carlo, A., Brunetti, F., Reale, A(2011).

Outro estudo utilizou a técnica de Fiação por Sopro de Solução (FSS) para produzir, pela primeira vez, nanofibras do supercondutor $YBa_2Cu_3O_{7-x}$ (YBCO – óxido de ítrio-bário-cobre). Os autores, Rotta, M.; Zadorosny, L.; Carvalho, C. L.; Malmonge, J. A.; Malmonge, L. F.; zadorosny, R (2016) demonstram que a FSS mostrou-se especialmente promissora por eliminar a necessidade de altas tensões elétricas e coletores condutores, além de apresentar taxas de produção significativamente superiores às da eletrofiação.

Para a preparação da solução precursora, foram utilizados acetatos metálicos de ítrio, bário e cobre combinados ao PVP (polivinilpirrolidona) como agente estruturante, em duas razões Ac:PVP (1:1 e 5:1). As fibras obtidas inicialmente apresentaram morfologia contínua, com diâmetros médios entre 389 e 426 nm. Após etapas controladas de secagem, calcinação e sinterização sob fluxo de oxigênio, formaram-se nanofibras cerâmicas de YBCO com diâmetros finais de 359 e 375 nm, mantendo estrutura fibrosa e exibindo superfícies granulares típicas de materiais cerâmicos.

Esses resultados evidenciaram o potencial da FSS como uma rota eficiente, econômica e escalonável para a produção de nanofibras cerâmicas supercondutoras, com aplicações em eletrônica de alta frequência, dispositivos de potência e circuitos em escala manométrica.

A técnica de Fiação por Sopro de Solução (FSS) foi utilizada para produzir nanocompósitos de (fluoreto de polivinilideno (PVDF) contendo diferentes teores de dióxido de titânio (TiO_2), gerando filmes com morfologia fibrilar e boa dispersão das nanopartículas. A adição de TiO_2 modificou a taxa de evaporação do solvente durante o processamento, influenciando a rugosidade e a topografia das fibras, embora não tenha alterado significativamente as fases cristalinas do PVDF, que permaneceu majoritariamente na fase β.

O trabalho de González-benito, J. Teno J., González-gaitano G., Xu, S., Chiang, M.Y.(2017) dão outra ideia de formação de compósitos, neste, as análises de superfície mostraram que concentrações crescentes de TiO_2 aumentaram

inicialmente a contribuição polar da energia livre de superfície, levando, em teores maiores, a superfícies mais hidrofóbicas. Ensaios de adesão celular indicaram que a presença de TiO_2 elevou a força de adesão de *Streptococcus mutans*, efeito atribuído predominantemente a interações específicas com os grupos funcionais do material. Esses resultados demonstraram que a FSS foi uma rota eficaz para a produção de nanocompósitos PVDF/TiO_2 com propriedades morfológicas e de superfície moduláveis para aplicações biomédicas.

6. O CENÁRIO ATUAL DA PESQUISA EM NANOFIBRAS POLIMÉRICAS

A pesquisa em nanofibras poliméricas tem apresentado um crescimento contínuo e significativo ao longo da última década, tendência que se consolidou entre 2020 e 2025. Esse avanço é corroborado pelo aumento expressivo de publicações relacionadas à eletrofiação e técnicas correlatas, que passaram de cerca de mil artigos anuais em 2014 para mais de 2.500 em 2024. Estima-se que mais de 200 polímeros já foram processados por eletrofiação com sucesso, demonstrando a versatilidade do campo.

No mesmo período, observou-se também uma expansão consistente do interesse pela técnica Fiação por sopro ou “aerografia. Revisões recentes mostram que o número de trabalhos sobre FSS cresce de forma sistemática desde meados dos anos 2010, alcançando seus maiores índices de publicação entre 2022 e 2024, o que evidencia o amadurecimento científico da técnica e sua consolidação em diversas áreas de aplicação.

As pesquisas envolvendo nanofibras poliméricas permanecem fortemente concentradas nos campos de Ciência dos Polímeros, Ciência e Engenharia de Materiais, Química Multidisciplinar, Físico-Química e Nanociência e Nanotecnologia. Além disso, cresce o número de estudos voltados para tratamento de água e efluentes, ultrafiltração e desenvolvimento de membranas seletivas. Tais áreas respondem por grande parte da produção científica recente, refletindo tanto o avanço das metodologias de obtenção quanto a expansão das aplicações industriais e ambientais.

Publicações entre 2020 e 2024 destacam seu uso em aplicações biomédicas, filtros de ar e água, materiais funcionais, além de sua utilidade em processos emergenciais, como na fabricação acelerada de nanofibras para máscaras do tipo N95.

O termo aerografia, embora menos difundido na literatura nacional, também tem ganhado tração em publicações internacionais relacionadas à deposição e otimização de fibras.

Apesar do robusto crescimento global, a pesquisa em FSS no Brasil ainda é relativamente incipiente, com poucos grupos dedicando-se exclusivamente ao

desenvolvimento teórico e experimental da técnica. Essa lacuna, entretanto, representa uma oportunidade estratégica para consolidação nacional da área, sobretudo considerando a demanda crescente por métodos de produção de nanomateriais mais rápidos, versáteis e economicamente viáveis. Dessa forma, a evolução da eletrofiação e da FSS no período de 2020 a 2025 confirma o dinamismo e o potencial tecnológico das nanofibras poliméricas, reforçando sua relevância tanto para geração de conhecimento quanto para aplicações industriais emergentes.

A adaptação da Fiação por Sopro em Solução por meio da Aerografia permite altas taxas de produção e a capacidade de depositar nanofibras em substratos irregulares ou vivos. Embora a Aerografia apresente desafios na otimização de parâmetros (como risco de entupimento com soluções mais concentradas e limitações de pressão do equipamento comercial), a otimização de variáveis (como 20% m/v de PVDF a 5 bar) demonstrou a capacidade de produzir nanofibras de qualidade nanométrica (138.4 nm) com a desejada fase preservada.

O desenvolvimento e a simplificação da tecnologia de obtenção de nanofibras por aerografia abrem espaço para futuras melhorias e a ampla utilização em diversas áreas, especialmente na área biomédica e na produção de filtros avançados para o tratamento de água.

7. ALGUMAS CONSIDERAÇÕES

A aerografia, como adaptação simplificada da FSS, como já mencionado anteriormente, demonstra elevado potencial para a produção rápida de nanofibras com diâmetros reduzidos, alta porosidade e excelente capacidade de deposição sobre diferentes tipos de substratos, e apesar dos desafios ainda existentes, como entupimentos, limitações de pressão e controle menos preciso da taxa de alimentação, os resultados apresentados na literatura comprovam que ajustes adequados de parâmetros (como concentrações otimizadas de polímero e pressões moderadas) permitem a obtenção de fibras de alta qualidade.

O cenário atual demonstra que, enquanto internacionalmente a técnica FSS/Aerografia avança de maneira consistente, no Brasil o campo ainda se encontra em desenvolvimento inicial, com poucos grupos dedicados à sua investigação.

O avanço contínuo das investigações nessa área tende a consolidar essa técnica como uma das estratégias mais promissoras para a produção de nanomateriais de alto desempenho nos próximos anos.

Dessa forma, conclui-se que a FSS via aerografia configura uma plataforma tecnológica robusta e em expansão, capaz de democratizar o acesso à produção de nanofibras poliméricas e de ampliar significativamente suas aplicações científicas, ambientais e industriais.

REFERÊNCIAS BIBLIOGRÁFICAS

1. Huanga, Z-M., Zhang, Y.-Z., Kotakic, M., Ramakrishna, S. A review on polymer nanofibers by electrospinning and their applications in nanocomposites. Composites Science and Technology. V.63(15). p.2223-2253. 2003.

2. Kenry, Lim T., C. Nanofiber technology: current status and emerging developments. Progress in Polymer Science. n.70 p.1–17. 2017.

3. Gopal, R.; Kaur, S.; Ma, Z.; Chan, C.; Ramakrishna, S.; Matsuura, T. Electrospun nanofibrous filtration membrane. Journal of Membrane Science, Amsterdam, v. 281, p.581-586, 2006.

4. Trindade, R. S. Caracterização de membranas poliméricas aplicadas ao processo de microfiltração. 2010. 74 f. Trabalho de Conclusão de Curso (Graduação) - Universidade Federal do Rio Grande do Sul - UFRGS, Porto Alegre, 2010. Fd.

5. Wolf, C.; Tscherner, M.; KöstleR, S. Ultra-fast opto-chemical sensors by using electrospun nanofibers as sensing layers. Sensors And Actuators B: Chemical, Amsterdam, v. 209, p.1064-1069, mar. 2015.

6. Costa, R. G. F.; Oliveira, J. E.; Paula, G. F.; PiccianI, P. H. S.; Medeiros, E. S.; Mattoso, L. H. C. Eletrofiação de polímeros em solução. Parte II: Aplicações e perspectivas. Polímeros, São Carlos, v. 22, n. 2, p. 178-185, 2012.

7. Martins, A.; Araujo, J. V.; Reis, R. L.; Neves, N. M. Electrospun nanostructured scaffolds for tissue engineering applications. Nanomedicine, London, v. 2, n. 6, p. 929-942, 2007.

8. Liao, S.; Li, B.; Ma, W.; Wei, H.; Chan, C.; RamakishnA, S. Biomimetic electrospun nanofibers for tissue regeneration. Biomedic Materials, Bristol, v. 1, n. 3, p. R45-R53, 2006.

9. Hassanzadeh P, Kharaziha M, Nikkhah M, Shin SR, Jin J, He S, et al. Chitinnanofiber micropatterned flexible substrates for tissue engineering. J MaterChem B 2013;1:4217–24.

10. Shah S, Yin PT, Uehara TM, Chueng STD, Yang L, Lee KB. Guiding stem cel ldifferentiation into oligodendrocytes using graphene-nanofiber hybridscaffolds. Adv Mater 2014;26:3673–80.

11. Yang X, Zou W, Su Y, Zhu Y, Jiang H, Shen J, et al. Activated nitrogen-doped carbon nanofibers with hierarchical pore as efficient oxygen reductionreaction catalyst for microbial fuel cells. J Power Sources 2014;266:36–42.

12. Shang M, Wang W, Sun S, Gao E, Zhang Z, Zhang L, et al. The design andrealization of a large-area flexible nanofiber-based mat for pollutantdegradation: an application in photocatalysis. Nanoscale 2013;5:50 36–42.

13. Cheng L, Ma SY, Wang TT, Li XB, Luo J, Li WQ, et al. Synthesis andcharacterization of hollow nanofibers by electrospinning for ethanolsensing properties. Mater Lett 2014;131:23–6.

14. Wu Q, Tran T, Lu W, Wu J. Electrospun silicon/carbon/titanium oxidecomposite nanofibers for lithium ion batteries. J Power Sources2014;258: 39–45.

15. Liu Y, Zhao L, Li M, Guo L. core-shell nanofiber film forphotoelectrochemical hydrogen generation. Nanoscale 2014;6:7397–404.

16. Shi H, Zhou M, Song D, Pan X, Fu J, Zhou J, et al. Highly porous electrospun nanofibers with high photocatalytic activities. Ceram Intern2014;40:10383–93.

17. Liao Y, Li XG, Hoek EMV, Kaner RB. Carbon nanotube/polyaniline nanofiberultrafiltration membranes. J Mater Chem A 2013;1:15390–6.

18. Wang Y, Zhang X, He X, Zhang W, Zhang X, Lu C. In situ synthesis of coated cellulose nanofibers hybrid for effective removal of methylene blue.Carbohydr Polym 2014;110:302–8.

19. Ayad MM, Salahuddin NA,Minisy IM, Amer WA. Chitosan/polyanilinenanofibers coating on the quartz crystal microbalance electrode for gassensing. Sens Actuators B 2014;202:144–53.

20. Zhao R, Li X, Sun B, Zhang Y, Zhang D, Tang Z, et al. Electrospunchitosan/sericin composite nanofibers with antibacterial property aspotential wound dressings. Int J Biol Macromol 2014;68: 92–7.

21. Li, D.; Xia, Y. Electrospinning of nanofibers: reinventing the wheeel? Advanced Materials, Weinheim, v. 16, n. 14, p. 1151-1170, 2004.

22. Wu, N., Wei, H. H., Zhang, L. Z. Efficient removal of heavy metal ions with biopolymer template synthesized mesoporous titania beads of hundreds of micrometers size, Environmental Science & Technology 46 (2012) 419–425.

23. Lan, S. H., Ju, F., Wu X. W. Treatment of wastewater containing EDTA Cu(II) using the combined process of interior microelectrolysis and fentonoxidation–coagulation, Separation and Purification Technology 89 (2012) 117–124.

24. Rashidi, F., Sarabi, R. S., Ghasemi, Z., Serif, A. Kinetic, equilibrium and thermodynamic studies for the removal of lead (II) and copper (II) ions from aqueous solutions by nanocrystalline, Superlattices and Microstructures 48 (2010) 577–591.

25. Machado, R. L. Despirogenação de soluções de imunoglobulina G humana: adsorção de endotoxinas em membrana de quitosana. Dissertação (mestrado) - Universidade Estadual de Campinas, Campinas/SP. 2003.

26. Armoa, M. H., Junior, M. J. Princípios e aplicações de processos de separação por membranas inorgânicas. Ciência & Tecnologia: FATEC-JB, Jaboticabal, v. 2, n. 1, p. 80-97, 2011. ISSN 2178-9436.

27. Morandi, C. G. Síntese, Caracterização e otmização de membranas poliméricas adsorventes para a remoção de disruptores endócrinos de águas residuais. (2011) 54f. Trabalho de Diplomação me Engenharia Química. Universidade Federal do Rio Grande do Sul. Porto Alegre 2011.

28. Mohammad A.W., Teowa, Y. H.. Ang W.L., Chung Y.T., Oatley-Radcliffe D.L., HILAL, N. Nanofiltration membranes review: Recent advances and future prospects. Desalination n.356 p.226–254.2015.

29. Bhardwaj, N.; Kundu, S.C. Electrospinning: A fascinating fiber fabrication technique. Biotechnology Advances, 28, p. 325–347, 2010.

30. Doshi, J.; Reneker, D.H. Electrospinning Process and Applications of Electrospun Fibers. Journal of Electrostatics, 35, p 151-160, 1995.

31. Bian, S; Jayaram, S.; Cherney, E.A. Electrospinning as a new method of preparing nanofilled silicone rubber composites. IEEE Transactions on Dielectrics and Electrical Insulation, vol. 19, n° 3; 2012.

32. Costa, R.G.F.; Oliveira, J.E.; Paula, G.F.; Picciani, P.H.; Medeiros, E.S.; Ribeiro, C.; Mattoso, L.H.C. Eletrofiação de Polímeros em solução. Parte I: Fundamentação teórica. Polímeros: Ciência e Tecnologia, vol. 22, n° 2, p. 170-177, 2012.

33. Yarin, A.L.; Koombhongse, S.; Reneker, D.H. Taylor cone and jetting from liquid droplets in electrospinning of nanofibers. Journal of Applied Physics, vol 90, n° 9, p 4836-4846, 2001.

34. Oktay, B.; Apohan, N.K.; Kuruca, S.E. Fabrication of nanofiber mats from electrospinning of functionalized polymers. Materials Science and Engineering, 64, 2014.

35. Greiner, A.; Wendorff, J.H. Electrospinning: A fascinating method for the preparation of ultrathin fibers. Angewandte Chemie – International Edition, vol. 46, p. 5670 – 5703, 2007.

36. SITE INOVAÇÃO TECNOLÓGICA. Bioplásticos de fibras vegetais se equiparam à fibra de carbono. 13/04/2011. Online. Disponível em [https://www.inovacaotecnologica.com.br/noticias/noticia.php?artigo=bioplasticos-fibras-vegetais&id=010160110413]. Capturado em 15/08/2013.

37. Teo, W.E.; Ramakrishna, S. A review on electrospinning design and nanofibre assemblies. Nanotechnology, 17, p 89–106, 2006.

38. Almeida, R.S.; Boery, M.N.O.; Barra, G.M.O.; d'Ávila, M.A. Processo de eletrofiação por aplicação de CA do polímero poli(fluoreto de vinilideno) – PVDF. 7° Congresso Latino Americano de Órgãos Artificiais e Biomateriais, Natal-RN, 2012.

39. Frenot, A.; Chronakis, I.S. Polymer nanofibers assembled by electrospinning. Current Opinion in Colloid and Interface Science, 8, p. 64–75, 2003.

40. Guerrini, L.M.; Branciforti, M.C.; Bretas, R.E.S. Eletrofiação do poli (álcool vinílico) via solução aquosa. Polímeros: Ciência e Tecnologia, vol. 16, n° 4, p. 286-293, 2006.

41. Costa, L. M. M.; Bretas, R. E. S.; Gregório, R. Jr. Effect of solution concentration on the electrospray/electrospinning transition and on the crystalline phase of PVDF. Materials Sciences and Applications, Irvine, v. 1, p. 247-252, 2010.

42. Pham, Q. P.; Sharma, U.; Mikos, A.G. Electrospinning of polymeric nanofibers for tissue engineering applications: a review. Tissue Engineering, New Rochelle, v. 12, p. 1197-1211, 2006.

43. Nasir, M.; Matsumoto, H.; Danno, T.; Minagawa, M.; Irisawa, T.; Shioya, M.; Tanioka, A.; Control of diameter, morphology, and structure of PVDF nanofiber fabricated by electrospray deposition. Journal of Polymer Science: Part B: Polymer Physics, Hoboken, v. 44, n. 5, p. 779-786, 2006.

44. Hu, X., Zhang, X., Shen, X, LI H, Takai O, Saito N. Plasma-induced synthesis of nanofibers and nanoflowers in water. Plasma Chem Plasma Process.v.34n.11p29–39. 2014.

45. Ren L, Ozisik R, Kotha SP, Underhill PT. Highly efficient fabrication of polymernanofiber assembly by centrifugal jet spinning: process and characterization.Macromolecules 2015;48:2593–602.

46. Huang Y, Duan Y, Ding Y, Bu N, Pan Y, Lu N, et al. Versatile, kineticallycontrolled, high precision electrohydrodynamic writing of micro/nanofibers.Sci Rep 2014;4(5949):1–9.

47. Park JU, Hardy M, Kang SJ, Barton K, Adair K, Mukhopadhyay Dk Lee CY, et al.High-resolution electrohydrodynamic jet printing. Nat Mater 2007;6:782–9.

48. Wongpajan R., Thumsorn S., Inoya, H., Okoshi, M., Hamada, H. Development of Cotton Candy Method for High Productivity Polypropylene. Fibers Webs. Fibers and Polymers 2018, Vol.19, No.1.

49. Medeiros, E. S.; Glenn, G. M.; Klamczynski, A. P.; Orts, W. J.; Mattoso, L. H. C. Solution blow spinning. 2010. US Patent, 0062.08.

50. Medeiros, E. S.; Glenn, G. M.; Klamczynski, A. P.; ORTS, W. J.; Mattoso, L. H.C. Solution blow spinning: a new method to produce micro- and nanofibers from polymer solutions. Journal of Applied Polymer Science, Hoboken, v. 113, n. 4, p. 2322-2330, 2009.

51. Behrens, A.M, Casey B.J., Sikorski, M.J., WU K. L., Tutak, WO., Sandler, A. D., Kofinas, P. In situ deposition of PLGA nanofibers via solution blow spinning. American Chemical Society Macro Letters.v.3 p.249–54. 2014.

52. Daristotle, J. L., Behrens A. M., Sandler, A.D., Kofinas P., A Review of the Fundamental Principles and Applications of Solution Blow Spinning. ACS Appl. Mater. Interfaces 2016, 8, 34951−34963.

53. Oliveira, J. E.; Moraes, E. A.; Costa, R. G. F.; Afonso, A. S.; Mattoso, L. H. C.; Orts, W. J.; Medeiros, E. S. Nano and submicrometric fibers of Poly(D,L-Lactide) obtained by solution blow spinning: process and solution variables. Journal of Applied Polymer Science, Hoboken, v.112, n. 5, p. 3396-3405. 2011.

54. Zadorosny, L. Produção e caracterização de micro e nanofibras de Poli (fluoreto de vinilideno) – (PVDF) obtidos pela técnica de fiação por sopro em solução. 2013. 86 f. Dissertação (Mestrado)– Faculdade de Engenharia, Universidade Estadual Paulista- UNESP. Ilha Solteira, 2013.

55. Dias G.C., Zadorosny, L., Sanches, A.O., Malmonge, L.F. Produção microfibras magnéticas de Poli(fluoreto de vinilideno) e Hexaferrita de Bário-(PVDF/), obtidos pela técnica de fiação por sopro de solução (FSS). Revista Iberoamericana de Polímeros y Materiales. v.19. n.1.p.10-19. 2018.

56. Li, L.; Kang, W.; Zhao, Y.; Li, Y.; Shi, J.; Cheng, B. Preparation of Flexible Ultra-Fine Fiber Mats via the Solution Blowing Method. Ceram. Int. 2015, 41 (1), 409−415.

57. Cheng, B.; Tao, X.; Shi, L.; Yan, G.; Zhuang, X. Fabrication of Ceramic Fiber Mats by Solution Blowing Process. Ceram. Int. 2014, 40 (9), 15013−15018.

58. Shi, S.; Zhuang, X.; Cheng, B.; Wang, X. Solution Blowing of Nanoflake-Encapsulated Carbon Nanofibers as Electrodes for Supercapacitors. J. Mater. Chem. A 2013, 1 (44), 13779.

59. Jia, K.; Zhuang, X.; Cheng, B.; Shi, S.; Shi, Z.; Zhang, B. Solution Blown Aligned Carbon Nanofiber Yarn as Supercapacitor Electrode. J. Mater. Sci.: Mater. Electron. 2013, 24 (12), 4769−4773.

60. Farias, R. M. DA C.; Menezes, R. R.; Oliveira, J. E.; Medeiros E. S. Production of Submicrometric Fibers of Mullite by Solution Blow Spinning (SBS). Mater. Lett. 2015, 149, 47−49.

61. Rotta, M.; Zadorosny, L.; Carvalho, C. L.; Malmonge, J. A.; Malmonge, L. F.; zadorosny, R. YBCO Ceramic Nanofibers Obtained by the New Technique of Solution Blow Spinning. Ceram. Int. 2016, 42 (14), 16230−16234.

62. Dias, Y. J., Gimenes C.T., Torres, S. A. P. V., Malmonge, J. A • Gualdi, A. J., de PAULA, F. R. . fibers synthesis by solution blow spinning technique. J Mater Sci: Mater Electron (2018) 29:514–518 DOI 10.1007/s10854-017-7941-z.

63. Costa, D. L.; Leite, R. S.; Neves, G. A.; Santana, L. N. D. L.; Medeiros, E. S.; Menezes, R. R. Synthesis of and Nano and Submicrometric Fibers by Solution Blow Spinning. Mater. Lett. 2016, 183, 109–113.

64. Soltan, M. A. A. An investigation into the history of the airbrush and the impact of the conservation treatment of airbrushed canvas paintings. Doctoral thesis, Northumbria University. 2015.

69. SCHWEIZER, M., GOSDAL, A.; PEREIRA C.Tipos de Aerógrafos. (2002). Disponível em [https://www.spmodelismo.com.br/material/aerografo/tipos.php]. Acesso em 14 de março de 2017.

70. Tutak, W., Gelven, G., Markle, C. and Palmer, X.-L. (2015), Rapid polymer fiber airbrushing: Impact of a device design on the fiber fabrication and matrix quality. J. Appl. Polym. Sci., 132, 42813, doi:10.1002/app.42813.

71. Hoffman, K.; Skrtic, D.; Sun, J.; Tutak, W. Airbrushed Composite Polymer Nanofiber Scaffolds with Improved Cell Penetration for Bone Tissue Regeneration. Tissue Eng., Part C 2015, 21 (3), 284–291.

72. Vak, D., Kim, S.S., JO, J., Oh, S.H., Na, S. I., Kim, J., Kim, D.Y., Fabrication of organic bulk heterojunction solar cells by a spray deposition method for low- cost power generation. Applied. Physics. Letters. v.91 p.081102–081104. 2007.

73. Girotto, C., Rand, B.P., Genoe, J., Heremans, P. Exploring spray coating as a deposition technique for the fabrication of solution-processed solar cells. Solar Energy Materials & Solar Cells v.93 p.454–458. 2009.

74. Green, R., Morfa, A., Ferguson, A.J., Kopidakis, N., Rumbles, G., Shaheen, S.E. Performance of bulk heterojunction photovoltaic devices prepared by air- brush spray deposition. Applied Physics. Letters. v. 92 p033301–033303. 2008.

75. Na, S.I., Yu, B-K., Kim,S-S., Vak, D., K. S., Yeo J.S., Kim, D-Y. Fully spray-coated ITO-free organic solar cells for low-cost power generation, Solar Energy Materials & Solar Cells v.94 p.1333–1337. 2010.

76. Steele A, Bayer I, Loth E. Inherently Superoleophobic Nanocomposite Coatings by Spray Atomization Nano Letters. v. 9(1) p.501-505. 2008.

77. Pham, V.H., Cuong, T.V, Hur, S.H., Shin, E.W., Kim, J.S., Chung, J.S., Kim, E.J. Fast and simple fabrication of a large transparent chemically-converted graphene film by spray-coating.Carbon. v.48(7) p.1945-1951. 2010.

78. Kern, N.G, Behrens A. M, Srinivasan P, Rossi, C.T., Daristotle, J.L, Kofinas, P. Sandler A. D. Solution blow spun polymer: A novel preclinical surgical sealant for bowel anastomoses. Journal of Pediatric Surgery.v.52(8) 2017p.1308-1312. 2017.

79. Susanna G., Salamandra, L., Brown, T. M., di Carlo, A., Brunetti, F., Reale, A. Airbrush spray-coating of polymer bulk-heterojunction solar cells. Solar Energy Materials & Solar Cells v.95 p. 1775–1778. 2011.

80. Lahlou, H., Vilanovaa, X., Fierro V., Celzardb, A., Llobet E., Correig X. Preparation and characterisation of a planar pre-concentrator for benzene based on different activated carbon materials deposited by air-brushing. Sensors and Actuators B v.154 p.213–219. 2011.

81. González-benito, J. Teno J., González-gaitano G., Xu, S., Chiang, M.Y. PVDF/TiO_2 nanocomposites prepared by solution blow spinning: Surface properties and their relation with S. Mutans adhesion. Polymer Testing v.58. p.21-30. 2017.

82. Srinivasan S, Chhatre S.S., Mabry, J. M., Cohen RE, Mckinley GH. Solution spraying of poly(methyl methacrylate) blends to fabricate microtextured, superoleophobic surfaces. Polymer. v. 52(14). p.3209-18. 2011.

83. Vural, M.; Behrens, A. M.; Ayyub, O. B.; Ayoub, J. J.; Kofinas, P. Sprayable Elastic Conductors Based on Block Copolymer Silver Nanoparticle Composites. American Chemical Society Nano. v.9 (1) p.336–344. 2015.

84. Tutak, W.; Sarkar, S.; Lin-gibson, S.; Farooque, T. M.; Jyotsnendu, G.; Wang, D.; Kohn, J.; Bolikal, D.; Simon, C. G. The Support of Bone Marrow Stromal Cell Differentiation by Airbrushed Nanofiber Scaffolds. Biomaterials. v.34 (10) p. 2389–2398. 2013.

85. Jin, T., Wang, J., Zhu, X, Xu, Y, Zhou, X, Yang, L. A new transient expression system for large-scale production of recombinant proteins in plants based on air-brushing an Agrobacterium suspension. Biotechnology Reports. v. 6 p.36–40. 2015.

86. de Windt T.S., Vonk L.A., Buskermolen J.K., Visser J., Karperien M. Bleys, R.L.A.W, Dhert , W.J.A., Saris D.B.F. Arthroscopic airbrush assisted cell implantation for cartilage repair in the knee: a controlled laboratory and human cadaveric study. Osteoarthritis and Cartilage v. 23 p.143-150. 2015.

87. Dias, G.C., Cellet, T.S.P., Santos. M. C., Sanches, A. O., Malmonge, L.F. PVDF Nanofibers Obtained by Solution Blow Spinning With use of a Commercial Airbrush. Journal of Polymer Research accept Frebuary 2019 [URL do artigo].

88. REMPEL, S. P. Obtenção de micro/nanofibras poliméricas por fiação por sopro :parâmetros e aplicação no controle de pragas agrícolas (2018).76 f. Dissertação (Mestrado) - Universidade de Caxias do Sul, Programa de Pós-Graduação em Engenharia e Ciência dos Materiais, 2018.

91. Gregório Jr R, Notoci NCPS (1995) Effect of PMMA addiction on the solution crystallization of the alpha-phase and beta-phase of poly (vinylidene fluoride)(PVDF). Journal Physics D: Applied Phys 28:432–436.

92. Lovinger AJ (1982) Poly(vinylidene fluoride). In: Basset DC (ed) Developments in crystalline polymers. Applied Science Publishers, London, chapter 5. pp 196–273.

93. Kepler R G, Nalwa, H S (1995) (Ed.). Ferroelectric polymers: chemistry, physics, and applications. New York: Marcel Dekker, Cap. 3: 183–185.

94. Reneker DH, Chun I (1996) Nanometre diameter fibres of polymer, produced by electrospinning. Nanotechnology, Bristol 7:216–223.

95. Benito JG, Teno J, Torres D, DíazM (2017) Solution blow spinning and obtaining submicrometric fibers of different polymers. Int J Nanoparticles Nanotech 3:5–10.

96. Shuai W, Yapeng L, Xiaoliang F, Mingda S, Chaoqun Z, Yahxian L, Qingbiao Y, Xia H (2011) Preparation of a durable superhydrophobic membrane by electrospinning poly (vinylidene fluoride) () mixed with epoxy–siloxane modified nanoparticles: a possible route to superhydrophobic surfaces with low water sliding angle and high water contact angle. J Colloid Interface Sci 359:380–388.

97. Roach P, Shirtcliffe NJ, Newton MI (2008) Progress in superhydrophobic surface development. Soft Matter 4:224–240.

98. Cai X, Lei T, Sund D, Lind L (2017) A critical analysis of the , and phases in poly(vinylidene fluoride) using FTIR. RSC Adv 7: 15382–15389.

99. Lanceros-Mendez S, Mano JF, Costa AM, Schmidt VH (2001) FTIR and DSC studies of mechanically deformed -pvdf films. Macromol Sci Physics 40:517–527.

100. Gregório RF (1993) Influência das condições de cristalização na morfologia de filmes de polifluoreto de vinilideno (). Polímeros: Ciência e Tecnologia 3:20–27.

101. Guo Z, Nilsson E, Rigdahl M, Hagström B (2013) Melt spinning of fibers with enhanced phase structure. J Appl Polym Sci 130:2603–2609.

102. Liu Z, Maréchal P, Jérôme R (1997) DMA andDSC investigations of the transition of poly (vinylidene fluoride). Polymer 38:4925–4929.

103. Zulfiqar S, Zulfiqar M, Munir A (1994) Study of the thermal-degradation of polychlorotrifluoroethylene, poly(vinylidene fluoride) and copolymers of chlorotri fluoroethylene and vinylidene fluoride. Polym Degrad Stab 43:423–430.

104. Cena CR, Silva MJ, Malmonge LF, Malmonge JA (2018) Poly(vinyl pyrrolidone) sub-microfibers produced by solution blow spinning. J Polym Res 25:238–246.

105. Young An M, Kim HT, Chang DR (2014) Multilayered separator based on porous polyethylene layer, layer, and electrospun nanofiber layer for lithium batteries. J Solid State Electrochem 18:1807–1814.

106. Francis L, Ghaffour N, Alsaadi S, Nunes SP, Amy GL (2013) Hollow fibers and nanofiber membranes for fresh water recovery using membrane distillation. J Mater Sci 49:2015–2053.

CHAPTER 3

SENSORES BASADOS EN GRAFENO FUNCIONALIZADO CON Pt-Sn/TiO_2 PARA DETECCIÓN DE SO_2

Data de submissão: 12/11/2025
Data de aceite: 28/11/2025

Luz María García-Rivera
Centro de Física y Tecnología Avanzada
Campus UNAM No. 3001
C.P: 76230 Juriquilla, Qro. México
https://orcid.org/0009-0008-8384-4992

Juan Manuel Padilla Flores
Universidad Tecnológica del
Centro de Veracruz
Avenida Universidad No. 350
Carretera Federal Cuitláhuac-La Tinaja
Localidad dos Caminos
Cuitláhuac, Veracruz, C.P 94910
http://orcid.org/0000-0002-9038-2959

Octavio Maldonado Saavedra
Universidad Tecnológica del
Centro de Veracruz
Avenida Universidad No. 350
Carretera Federal Cuitláhuac-La Tinaja
Localidad dos Caminos
Cuitláhuac, Veracruz, C.P. 94910
http://orcid.org/0000-0002-0851-4239

Erick A. Juarez-Arellano
Centro de Investigaciones Científicas
Instituto de Química Aplicada
Universidad del Papaloapan
Circuito Central 200, Parque Industrial
C.P. 68301, Tuxtepec, Oaxaca, México
http://orcid.org/0000-0003-4844-8317

RESUMEN: La siguiente propuesta, presenta los avances en el desarrollo de sensores que permitan el monitoreo en tiempo real de la integridad del $SF_{6,}$ mediante la evaluación de la presencia de subproductos de éste, en particular del $SO_{2.}$ El SF_6 es utilizado como material dieléctrico principalmente en interruptores de potencia. Se diseñaron sensores a base de nanocompuestos grafiticos decorados con distintas Np's metálicas. Se utilizó oxido de grafeno (OG), como nanoestructura principal del nanocompuesto y se caracterizó mediante DRX y espectroscopía Raman. Posteriormente se funcionalizó con Np's metálicas. Para la caracterización fisicoquímica de los sensores se utilizó microscopia SEM, AFM y óptica. Así como pruebas de eficiencia de los sensores a escala laboratorio en una cámara de gas utilizando una mezcla N_2-SO_2 a 120 ppm de este último. El nanocompuesto con una relación peso [1:3] (resina-nanoestructura Pt-Sn/TiO_2) presentó una respuesta promedio de 59% ante la presencia de SO_2.
PALABRAS CLAVE: nanocompuesto; nanopartículas de óxidos metálicos; óxido de grafeno; sensores de gas.

SENSORS BASED ON FUNCTIONALIZED GRAPHENE WHIT PT-SN/TIO2 FOR SO2 DETECTION

ABSTRACT: The following proposal presents the advances in the development

of sensors that allow real-time monitoring of SF_6 quality by evaluating the presence of SF_6 by-products, in particular SO_2. SF_6 is used as a dielectric material mainly in power switches. Sensors based on graphitic nanocomposites decorated with different metallic Np's were designed. Graphene oxide (GO) was used as the main nanostructure of the nanocomposite and was characterized by XRD and Raman spectroscopy. Subsequently, it was functionalized with metallic Np's. SEM, AFM and optical microscopy were used for the physicochemical characterization of the sensors. As well as efficiency tests of the sensors at laboratory scale in a gas chamber using a N_2-SO_2 mixture at 120 ppm of the latter. The nanocomposite with a [1:3] weight ratio (resin-nanostructure Pt-Sn/TiO_2) presented an average response of 59% in the presence of SO_2.
KEYWORDS: gas sensors; graphene oxide; nanocomposite; nanoparticles metal oxide.

1. INTRODUCCIÓN

La energía eléctrica que se utiliza diariamente es distribuida mediante una red eléctrica a lo largo del país, donde un elemento esencial son las subestaciones eléctricas, las cuales, tienen como objetivo distribuir y modificar la energía a los parámetros necesarios para su Utilización [1]. Dentro de las subestaciones eléctricas existen un sinfín de equipos y sistemas que trabajan en conjunto [2], por esta ocasión nos enfocaremos en los sistemas dieléctricos, los cuales tienen como finalidad asegurar el aislamiento eléctrico entre los conductores, piezas metálicas y la carcasa de los equipos [3]; estos pueden ser de diferentes elementos tales como: aceite dieléctrico y hexafluoruro de azufre (SF_6), siendo este último el más común en la actualidad [4] [5]. El SF_6 es el compuesto químico gaseoso ideal para utilizarse como inhibidor de arco eléctrico, ya que presenta una gran estabilidad química debido a su perfecto arreglo simétrico. Sin embargo, durante su empleo puede contaminarse con impurezas, tales como, humedad y oxígeno, lo que da paso a la generación de subproductos del mismo; los cuales originan una disminución en su capacidad dieléctrica, además de convertirlo en una sustancia peligrosa para la salud humana y al ambiente [6][7].

En los últimos años se han empleado algunos sistemas de monitoreo basados en diferentes técnicas [4] y aunque han sido eficientes en su momento, actualmente esta tecnología no se considera óptima para el monitoreo del SF_6, lo cual podría dar lugar a la no detección de fallas incipientes en los sistemas aislantes.

Dada esta problemática, es necesario investigar mejores opciones para minimizar su impacto, por lo que se propone el desarrollo de redes inteligentes, las cuales, se basan en sistemas de monitorización y diagnóstico en tiempo real con el objetivo de proporcionar información necesaria para la evaluación del estado en que se encuentra el gas.

En esta propuesta se busca diseñar sensores de tipo resistivo, dado que estos son capaces de dar una respuesta ante un cambio químico de su entorno [8]. El sensor está enfocado en la detección del dióxido de azufre (SO_2), subproducto principal del SF_6; con él se busca garantizar las mejores condiciones del gas y así prevenir cualquier eventualidad [9].

Para el desarrollo de un buen sensor resistivo es necesario tener una superficie con alta sensibilidad a su entorno, por lo que se optó por utilizar nanoestructuras de óxido de grafeno (OG), dado que por su bajo espesor atómico y gran número de sitios activos en la superficie es viable para esta aplicación [10]. Para potenciar aun más la sensibilidad del sensor se busca funcionalizar el OG con Np's metálicas y con ello obtener las nanoestructuras de refuerzo [11]. Se generará un nanocompuesto a base de una matriz polimérica de uso comercial reforzada con las nanoestructuras funcionalizadas de OG, con el cual se recubrirá de manera homogénea los circuitos interdigitados que fungirán como la base del sensor resistivo.

2. OBJETIVO

Diseñar y caracterizar un sensor a base de nanocompuestos grafíticos decorados con Np's metálicas dispersados en una matriz polimérica, para su aplicación en sensores de gas.

3. DESARROLLO EXPERIMENTAL

3.1. SÍNTESIS DE ÓXIDO DE GRAFENO POR EL MÉTODO DE HUMMERS MODIFICADO.

Se optó por utilizar óxido de grafeno (OG), dado que esta especie es más sensible y selectiva en el entorno en que se encuentre [12]. El método de Hummers permite obtener OG mediante un proceso redox en el grafito precursor [13], se propone el uso de dicromato de potasio ($K_2Cr_7O_7$), como agente oxidante. Se tomó como referencia la metodología descrita por Hernández y Galaviz (2016), la cual se modificó ligeramente de acuerdo a la presente propuesta.

3.2. FUNCIONALIZACIÓN DE OG CON NP'S METÁLICAS

Al introducir diferentes Np's metálicas en la estructura del OG, se busca generar una sinergia entre las especies, con la finalidad de obtener nanoestructuras con mayor sensibilidad a los cambios de su entorno [14] [15]. La figura 1, muestra las diferentes Np's metálicas utilizadas para la funcionalización del OG.

Se emplearon en conjunto las técnicas de sonicación y secado en horno, para lograr la funcionalización del OG de manera homogénea en toda la superficie, al dispersar las Np's seleccionadas [16] [17].

Figura 1. Np's metálicas empleadas para la funcionalización de OG (A) Al_2O_3, (B) TiO_2 y (C) Pt-Sn/TiO_2.

3.3. FORMULACIÓN DE NANOCOMPUESTOS Y PREPARACIÓN DE LOS SENSORES

Se empleó una matriz polimérica de uso comercial como la base del nanocompuesto diseñado. Se utilizaron diferentes concentraciones (ver Tabla 1), en relación en peso, con la finalidad de evaluar su comportamiento en función de la concentración.

Tabla 1. Concentraciones de los nanocompuestos formulados.

[3:1] - [30 mg resina: 10 mg OG/Np's]
[1:1] - [20 mg resina: 20 mg OG/Np's]
[1:3] – [10 mg resina: 30 mg OG/Np's]

Para homogenizar el nanocompuesto se utilizaron las técnicas de agitación mecánica, para dispersar las nanoestructuras en el sistema líquido, y sonicación para proporcionar energía localizada y así dispersar los aglomerados que se puedan generar, la figura 2 muestra parte de este proceso; debe de considerarse que esta técnica es recomendable solo para pequeños volúmenes [18].

Figura 2. Preparación de nanocompuestos utilizando el proceso de baño ultrasónico.

Una vez que se obtuvieron las formulaciones, se utilizó un aerógrafo como medio de deposición de los nanocompuestos en la superficie de las tarjetas interdigitadas, esto con la finalidad de lograr un recubrimiento homogéneo en todo el sensor. A continuación, figura 3, se muestran las tarjetas interdigitadas recubiertas con el nanocompuesto obtenido.

Figura 3. Tarjetas interdigitadas recubiertas con el nanocompuesto de Pt-Sn/TiO_2 a distintas concentraciones.

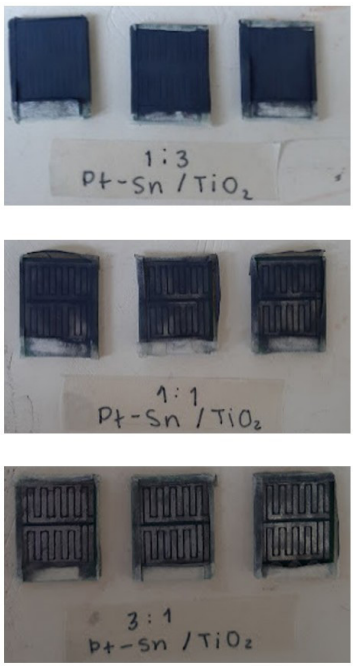

4. RESULTADOS Y DISCUSIONES

4.1. ANÁLISIS DE ESPECTROSCOPÍA RAMAN DEL OG

En la figura 4, se presenta el espectro obtenido, posterior al mapeo de la muestra de grafito comercial empleado como precursor; las bandas características de un grafito hexagonal identificadas como G y D, la primera se encuentra alrededor de los ~1580 cm^{-1} y se atribuye a la dispersión de primer orden de los átomos de ^6C con hibridación sp^2, la gran intensidad de la banda representa el gran número de átomos con tal hibridación dentro de la estructura del material; mientras que la banda D, se observa alrededor de los ~1350 cm^{-1} y se asocia a los cambios en el orden de la misma, por lo que al ser un grafito su intensidad es baja. De igual forma se identificaron las bandas D' (~1620 cm^{-1}), 2D (~2700 cm^{-1}) y la D+D (~2920 cm^{-1}) las cuales corresponden a la resonancia de la banda D.

Figura 4. Espectro Raman del grafito precursor.

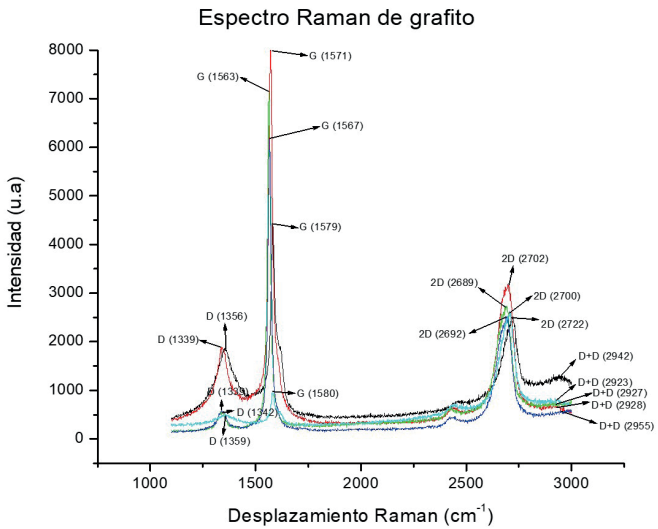

En la figura 5, se presenta el espectro Raman correspondiente al mapeo de la muestra de OG obtenido por el método de Hummers modificado. Se genera un cambio en las intensidades en las bandas D y G, debido al cambio en la estructura del grafito posterior a los procesos de oxidación y exfoliación, por lo que la intensidad de la banda D aumenta al existir mayor desorden de las láminas y la introducción de grupos funcionales a la estructura.

Figura 5. Espectro Raman de óxido de grafeno.

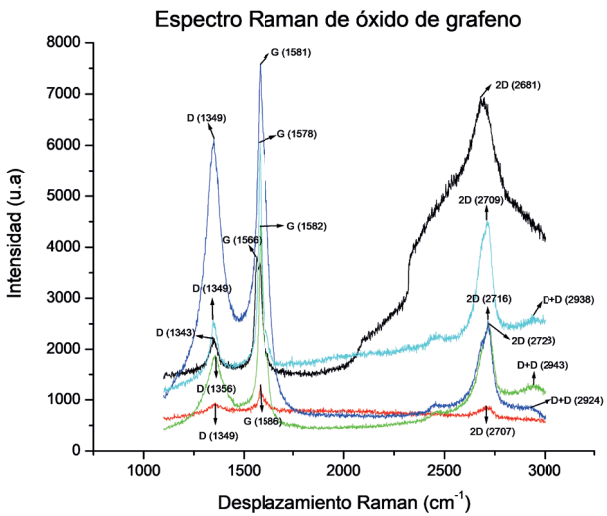

Al llevar a cabo las cinco mediciones correspondientes, se observa una gran variación en las intensidades y anchuras de las bandas, lo que nos indica que la muestra no es homogénea, existen puntos de la muestra con mayor porcentaje de conversión de grafito a OG que en otras.

4.2. ANÁLISIS DE DIFRACCIÓN DE RAYOS X DEL OG

De las figuras 6 a la 10, se muestran los difractogramas obtenidos del óxido de grafeno sintetizado por el método de Hummers modificado comparados con el obtenido del grafito precursor. En la figura 6, se logran apreciar los dos picos característicos del grafito, uno a los 26.6 ° y otro a 44.6 ° correspondiente al plano (002), lo que nos indica una estructura hexagonal típica de los materiales carbonos. Si bien el OG también presenta un pico similar al grafito, este no es tan intenso, lo que manifiesta que la estructura cristalina se ha modificado tras el proceso de oxidación.

Figura 6. Difractograma comparativo de grafito precursor (rojo) y OG (negro).

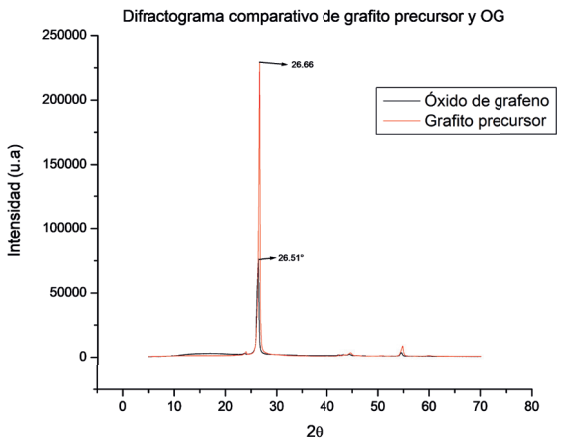

Se realizo una ampliación en el intervalo de los 25 ° a 35 °, figura 7, donde se aprecia un ligero desplazamiento hacia la izquierda del pico principal posterior a la oxidación del grafito.

Figura 7. Ampliación del pico principal, plano (002) en el intervalo de 25 ° y 35 °, color rojo grafito precursor, color negro OG.

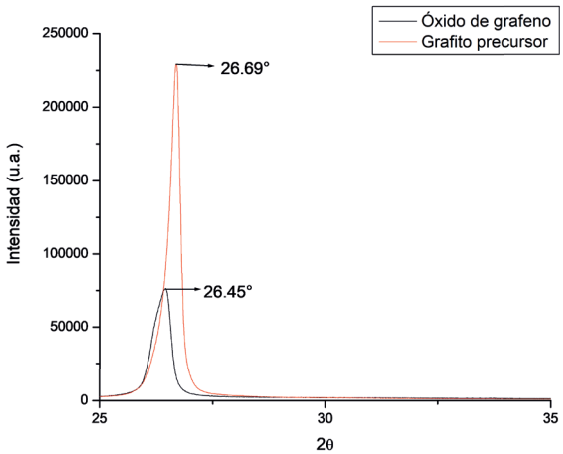

La figura 8 representa la ampliación en el intervalo de 0 ° a 25 ° del difractograma principal, en el que se puede apreciar la elevación de una curva en el ángulo 15.3 ° de la muestra estudiada. Se sabe que el pico de difracción característico de OG se desplaza en 2θ entre 9.90 ° y 10.6 °, lo cual, es indicativo de una gran distancia entre sus capas derivada de la incorporación de los grupos funcionales entre los planos del grafito, así como de su naturaleza cristalina.

Figura 8. Ampliaciones del difractograma comparativo de grafito precursor (rojo) y OG (negro) de 0 ° a 25 °.

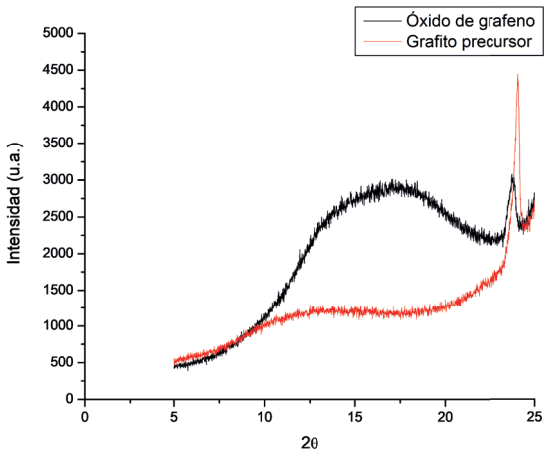

La figura 9, corresponde a una ampliación en el intervalo de 22.5 ° a 25.5 °, se observa para el OG un pico ancho alrededor de los 23.73 °, debido al re-apilamiento de

las capas de grafeno, ya que durante el proceso de síntesis se restablecen parcialmente los dominios sp^2 de la estructura, lo cual se identifica mediante el corrimiento hacia la izquierda del pico, así como la diminución de la intensidad del mismo.

Figura 9. Ampliaciones del difractograma comparativo de grafito precursor (rojo) y OG (negro), en el intervalo de 22.5 ° a 25.5 °.

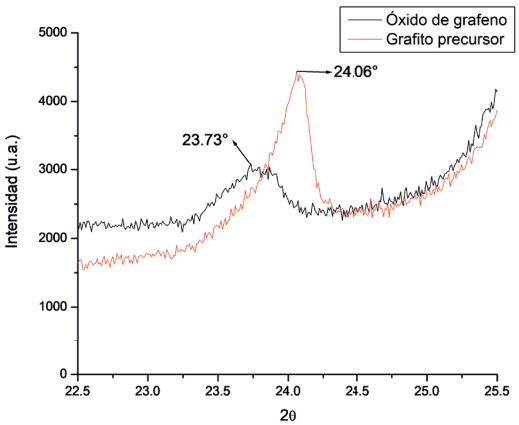

La figura 10 muestra la ampliación del difractograma principal en el intervalo de 40.5 ° a 43.5 °, esto con la finalidad de apreciar los picos alrededor de los 42.4±0.1 °, ya que de acuerdo a la literatura se sabe que es un pico característico del OG tras la oxidación correspondiente al plano (100), su poca intensidad se relaciona a la falta de regularidad de la estructura así como al menos espesor de empaquetamiento, deduciendo así una estructura con pocos números de capas de grafeno.

Figura 10. Ampliaciones del difractograma comparativo de grafito precursor (rojo) y OG (negro) en el intervalo de 40.5 ° a 43.5 °.

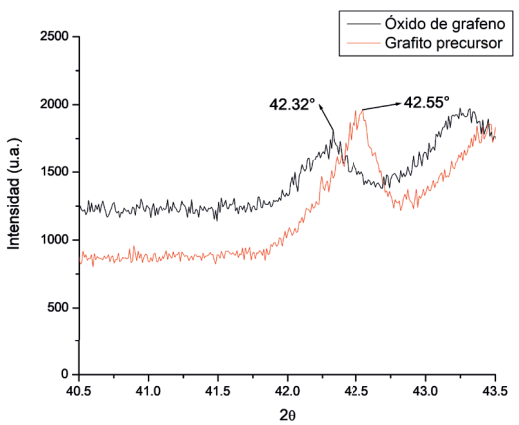

4.3. ANÁLISIS DE MICROSCOPÍA ÓPTICA

Para llevar a cabo este análisis se utilizó el adaptador para cámara Nurugo Micro Smartphone Microscope 400X, con el cual se lograron obtener microscopías con una amplificación de 200x, es decir, a una escala de 500 µm, las cuales nos permiten visualizar la superficie del sensor así como la distribución del nanocompuesto en la misma.

La figura 11, corresponde a la comparativa de las formulaciones a base de Pt-Sn/TiO_2, la concentración [1:1], muestra una mejor distribución del material, sin embargo, representa vacancias en la superficie, dado que el material solidifica creando pequeñas aglomeraciones a lo largo del sensor, generando así mayor diferencia entre los máximos y mínimos de la superficie.

Figura 11. Micrografías ópticas correspondiente a la formulación Pt-Sn/TiO_2 (A) [1:1], (B) [3:1].

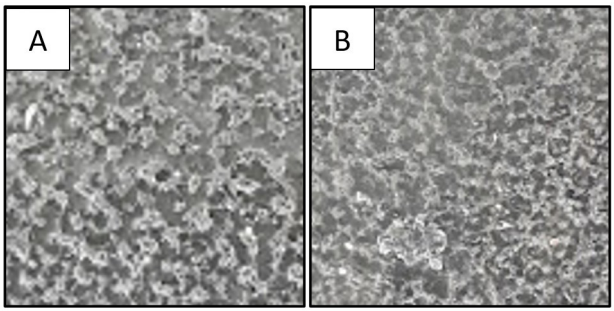

4.4. ANÁLISIS DE MICROSCOPÍA ELECTRÓNICA DE BARRIDO (SEM)

Para llevar a cabo el análisis por SEM se empleó el equipo TESCAN VEGA3, bajo las siguientes condiciones de trabajo: un bombardeo de electrones a 5.0 kV, una amplificación de 600 x, a una escala de 100 µm y velocidad de escaneo de 7.

Se analizó la muestra con la concentración [1:3], dado que al ser la de mayor concentración de nanoestructuras se observa una mejor respuesta ante la presencia del gas, de lo cual se discutirá más adelante. La figura 12, corresponde a la micrografía obtenida del sensor [1:3] de Pt-Sn/TiO_2, donde se logran apreciar pequeñas aglomeraciones a lo largo de toda la superficie, por lo que no es un material homogéneo, sin embargo, presenta una buena distribución. La forma particular de las aglomeraciones se puede comparar a una superficie porosa, lo que nos permite tener una mayor área superficial, punto clave para nuestro objetivo, considerando los resultados obtenidos por medio de otras técnicas se puede decir que esto es favorable para su efectividad.

Figura 12. Micrografía SEM correspondiente al sensor [1:3] de Pt-Sn/TiO_2.

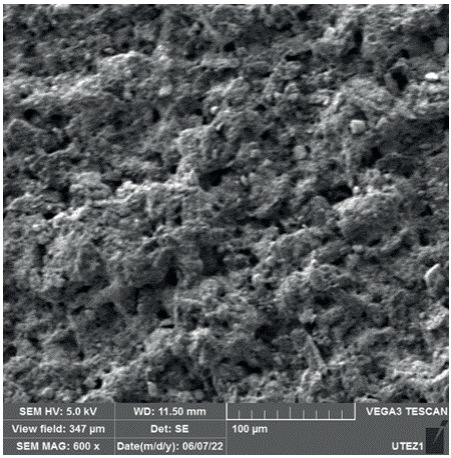

4.5. ANÁLISIS DE MICROSCOPÍA DE FUERZA ATÓMICA (AFM)

Durante el análisis se utilizó el equipo Nanosurf Naio, se escaneo un área de 44.86 µm, equivalente a 512 líneas, a una velocidad de 1.5 s.

Las micrografías 3D resultantes del análisis de la formulación de Pt-Sn/TiO_2 presentan grandes variaciones entre ellas, la figura 13A, corresponde a la concentración [1:1], la cual tiene una distribución muy homogénea, no presenta grandes diferencias dentro de los máximos y mínimos de altura del material, se observan algunos valles en la superficie. Mientras que la concentración [3:1], figura 13B, tiene una topología muy dispersa, zonas con grandes picos y delgados, lo que nos indica que el tamaño de los agregados es pequeño, sin embargo, es de gran altura, así como valles de mayor anchura, pero menor altura. Considerando las micrografías obtenidas en las otras técnicas de esta concentración, se comprueba que existen grandes aglomerados a lo largo de la superficie, esto debido al aumento de matriz en la formulación, ya que las nanoestructuras no se dispersan homogéneamente, sino que generan áreas ricas en ellas y partes deficientes. La última concentración, [1:3], figura 13C, muestra mayor homogeneidad, pero con algunos aglomerados de mayor altura y anchos variables. Comparando las 3 concentraciones, la [1:1] es la más homogénea.

Figura 13. Micrografías 3D de SEM correspondientes a la formulación Pt-Sn/TiO_2 (A) [1:1], (B) [3:1], (C) [1:3].

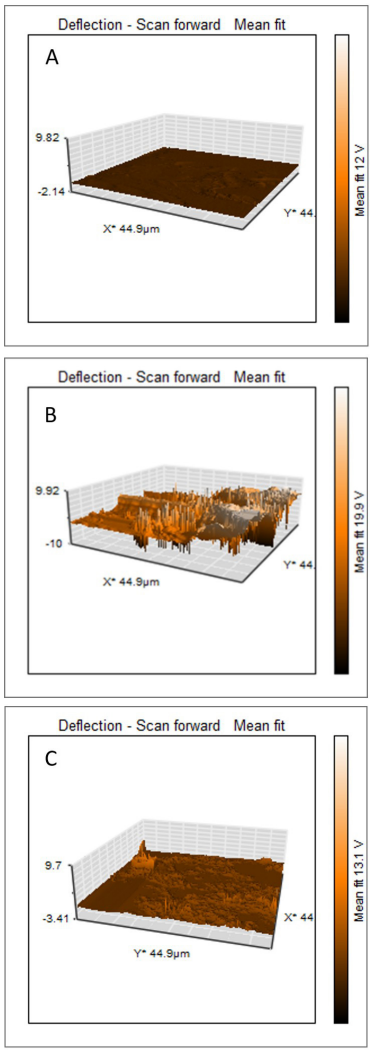

4.6. PRUEBAS DE EFECTIVIDAD EN CÁMARA DE GAS

Posterior a llevar el proceso de recubrimiento de las tarjetas interdigitadas con las formulaciones obtenidas, se dejaron reposar por 12 horas para dejar solidificar el nanomaterial compuesto, finalizado este tiempo, se midieron las resistencias de los sensores, con la finalidad de llevar un control de su comportamiento a condiciones ambientales y tenerlo como referencia para las pruebas ante la presencia de SO_2.

Las pruebas de eficiencia se realizaron en una cámara de gas diseñada para este proyecto en particular; la figura 14A, muestra el sistema donde se realizaron las pruebas. La figura 14B, muestra la forma en que se conectan los sensores dentro de la cámara.

Una vez preparado el sistema, se midieron las referencias en un ambiente de N_2, de esta manera obtenemos una línea base de las mediciones que se esperan al poner en contacto los sensores con el SO_2. Posteriormente, se cargó la cámara de SO_2 a 120 ppm y se monitoreo el comportamiento de los sensores por alrededor de 280 minutos, dado que nuestro objetivo es tener un sensor que brinde respuesta de manera inmediata al estar en contacto con SO_2.

Figura 14. (A) Cámara de gas para pruebas de eficiencia, (B) Conexión del sensor.

Con la finalidad de observar el comportamiento de los sensores en la cámara, se emplea la ecuación 1, donde: R_0 es la resistencia promedio en N_2, R, la resistencia en tiempo real del sensor en ambiente de SO_2.

Ecuación 1. Resistencia relativa.

$$S = \frac{R - R_0}{R_0} * 100\%$$

Se probaron los sensores con mayor concentración de nanoestructuras, dado que posterior a las pruebas anteriores, análisis morfológico y monitoreo de resistencias de referencia, se decidió que eran los que mejor respuesta nos pueden brindar. De esta manera, se obtuvo la gráfica que se muestra en la figura 15, donde se muestran los cambios de resistencia con respecto al tiempo.

Las líneas de color verde y rojo, representan a la formulación [1:3] Al_2O_3, la cual tiene una respuesta entre el 3% y 7%, el patrón de su comportamiento es repetitivo, es decir, si presenta cambios ante la presencia del SO_2 dentro de los primeros minutos, posteriormente se estabiliza y cada cierto tiempo presenta cambios nuevamente de manera espontánea; el porcentaje de respuesta es muy bajo a lo requerido para la aplicación.

Para la formulación [1:3] Pt-Sn/TiO_2, se obtuvo una respuesta promedio del 59% casi de manera instantánea al estar en contacto con el SO_2, lo cual es un resultado prometedor para su aplicación a nivel industrial, si bien aún faltan estudios por hacer al respecto es un buen inicio para esta formulación en particular.

Figura 15. Gráfica comparativa de las resistencias relativas, resultado de las pruebas de efectividad de los sensores. Color verde y rojo formulación [1:3] Al_2O_3, color negro formulación [1:3] Pt-Sn/TiO_2.

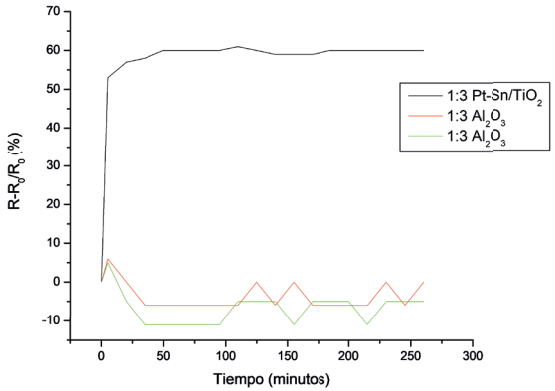

5. CONCLUSIONES

Al utilizar el método de Hummers modificado se obtuvo de manera parcial OG, sin embargo, la oxidación no fue de manera homogénea en toda la muestra, se presentan zonas con mayor grado de oxidación que otras; esto se debe principalmente por el cambio del agente oxidante empleado en la síntesis.

Las técnicas de microscopía óptica, SEM y AFM, muestran resultados congruentes entre ellos, nos brindan una buena imagen de la distribución y morfología del nanocompuesto sobre la superficie de los circuitos interdigitados. Se lograron identificar ciertos patrones de solidificación en los nanocompuestos a base de las mismas Np's metálicas, de igual forma que entre mayor es la cantidad de la matriz empleada es más propensa la formación de aglomeraciones de mayor tamaño.

Las formulaciones de la concentración [1:3] son las que brindan mejores resultados tanto en la distribución del material, como de sensibilidad a los cambios en su entorno.

Las pruebas de eficiencia son punto clave en nuestra investigación, dado que mediante ellas podemos evaluar la sensibilidad de los sensores ante los cambios en su entorno, esto nos permitió identificar que la formulación [1:3] de Pt-Sn/TiO_2, es la que muestra mejores resultados para el monitoreo de SO_2, alcanzando una respuesta promedio de 59% de cambio de su resistencia ante la presencia del gas, lo que sugiere que es un sensor muy viable para su aplicación.

6. AGRADECIMIENTOS

Los autores agradecemos el apoyo del Dr. Vicente Rodríguez González y la Dra. Bety Rivera Escoto del IPICYT, el Dr. Francisco Javier Tzompantzi Morales de

la UAM Iztapalapa y la Dra. Manuela Calixto Rodríguez de la UTEZ, por apoyarnos en las caracterizaciones de espectroscopía Raman, difracción de rayos X y microscopía electrónica de barrido, respectivamente. Al Ing. José Carlos Ruiz Vázquez por su apoyo durante las pruebas de eficiencia de los sensores.

REFERENCIAS

[1] Zárraga-Vázquez A.J (2021) Subestaciones eléctricas: tipos, elementos y beneficios. SISSA https://www.sissamx.com.mx/Nota/227/subestaciones-electricas:-tipos,-elementos-y-beneficios Fecha de consulta: abril de 2022.

[2] Zuñiga P. (2013) 8 partes de las subestaciones eléctricas. Instalaciones eléctricas residenciales. https://instalacioneselctricasresidenciales.blogspot.com/2013/05/subestaciones-electricas.html Fecha de consulta: marzo de 2022.

[3] Pozueta-Rodríguez M.A. (2015) Funcionalización de óxido de grafeno con nanopartículas de paladio y su aplicación en la detección de hidrógeno. San Luis Potosí: Instituto Potosino de investigación científica y tecnológica, A.C.

[4] Huamani M. (2018) El SF_6 en la industria eléctrica y su impacto en el medio ambiente. Lima: CITE energía.

[5] Electricidad (2021) Hexafluoruro de Azufre. Comisión Federal de Electricidad. México: CFE.

[6] Carpio-Balcazar R.V (2017) Diseño de un sistema de gestión integral para el hexafluoruro de azufre en la empresa eléctrica regional centro sur C.A. Ecuador: Universidad de Cuenca.

[7] Molina L. (2011) ElectroIndustria. El hexafluoruro de azufre. EMB. http://www.emb.cl/electroindustria/articulo.mvc?xid=1563&tip=7&xit=elhexafluoruro-de-azufre Fecha de consulta: marzo de 2022.

[8] Bautista-Burdallo I. (2014) Integración de microsensores y estructuras microfluídicas para la medida de parámetros químicos en sistemas biológicos. Barcelona: Universidad Autónoma de Barcelona.

[9] Erasmus (2020) Transmisor para gas SF_6. Vaisala. https://www.erasmus.com.co/index.php/es/lineas-de-productos/monitoreo-dehumedadsf6/en-sf6 Fecha de consulta: marzo de 2022.

[10] Felli E., Martinéz-Victoria E., Fernández- Campollo A.J, Aroca-Serrano A. (2016) El grafeno y sus derivados en la ingeniería tisular. España: Revista Iberoamericana Interdisciplinar de métodos, modelización y simulación.

[11] Esteve I, Gil M., Zaitegui L. Z, Quijano A, & García, M. (2020). Grafeno: obtención, tipos y su aplicación como sensor para detección de gases y sensor de presión. España: Universidad de los Andes.

[12] Hernández-Rosas O.F, Galaviz-Silva E. (2016) Electrodos transparentes conductores basados en óxido de grafeno reducido para depósito electroquímico de óxidos semiconductores de interés fotovoltaico. Tamaulipas: Centro de Investigación en Materiales Avanzados.

[13] Colom X, Cañavate J, Liz M.J, San Juan G & Gil I. (2020) Análisis estructural de óxidos de grafeno (OG) y óxidos de grafeno reducidos (rGO).

[14] Molina-Castelain M. (2017) Desarrollo de métodos sintéticos basados en química click para la preparación de materiales avanzados grafeno-polímero. Madrid: Universidad Complutense de Madrid.

[15] Orozco R.D. (2015) Síntesis y caracterización de materiales compuestos de óxido de grafeno con nanopartículas de plata y con dióxido de titanio. San Luis Potosí, México.

[16] Guillamón-Garrido A. (2018) Preparación y caracterización de nuevos nanocomposites de óxido de grafeno modificado con líquido iónico. Cartagena: Universidad Politécnica de Cartagena.

[17] Segovia N, Sánchez J, Choren E, Arteaga G & Arteaga A. (s.f) Caracterización de catalizadores Pt-Sn/Al_2O_3 por medio de una reacción sonda. Venezuela: Universidad de Zulia.

[18] Fernández-Ramos G. (2017) Efecto de la química superficial del óxido de grafeno en el desarrollo de aplicaciones. España: Universidad de Alicante.

CHAPTER 4

ELECTRODEPOSICIÓN DE RECUBRIMIENTOS METÁLICOS NANOESTRUCTURADOS

Data de submissão: 10/11/2025
Data de aceite: 24/11/2025

Carlos Alberto Mora Santos
Doctor en Ciencias de Ingeniería Mecánica
Instituto Tecnológico de Apizaco
Departamento de Metal- Mecánica
Apizaco, Tlaxcala, México
https://orcid.org/0000-0002-6050-6578

Marcos Bedolla Hernández
Doctor en Ingeniería Mecatrónica
Instituto Tecnológico de Apizaco
Departamento de Metal- Mecánica
Apizaco, Tlaxcala, México
https://orcid.org/0000-0001-9668-2779

Genaro Texcucano Romano
Maestro en Ingeniería Mecatrónica
Instituto Tecnológico de Apizaco
Departamento de Metal- Mecánica
Apizaco, Tlaxcala, México
https://orcid.org/0009-0002-2467-0271

Jorge Bedolla Hernández
Doctor en Ciencias de Ingeniería Mecánica
Instituto Tecnológico de Apizaco
Departamento de Metal- Mecánica
Apizaco, Tlaxcala, México
https://orcid.org/0000-0003-3856-6061

Jorge Aguilar Vázquez
Maestro en Ingeniería Administrativa
Instituto Tecnológico de Apizaco
Departamento de Metal- Mecánica
Apizaco, Tlaxcala, México
https://orcid.org/0009-0005-5287-7060

Luz Fabiola Sánchez Parra
Maestra en Docencia y Administración de Instituciones de Educación Superior
Instituto Tecnológico de Puebla
Departamento de Ciencias Económico Administrativas
Puebla, Puebla, México

RESUMEN: Se presenta el proceso sugerido para el desarrollo de recubrimientos nanoestructurados de cromo (CrNP´s) sobre superficies metálicas mediante la técnica de electrodeposición. Esta propuesta se considera como una alternativa a los procesos convencionales de cromado basados en iones Cr^{4+} y Cr^{6+}; considerados altamente tóxicos para el medio ambiente y la salud humana. La electrodeposición a partir de cromo Cr^{0} y Cr^{3+}en medio acuoso constituye un proceso sustentable y adaptable a superficies, mejorando las propiedades mecánicas y superficiales del sustrato, reduciendo el impacto ambiental. Los recubrimientos se obtuvieron mediante una celda electrolítica conformada por un ánodo de grafito y un cátodo de acero AISI 1020, empleando parámetros de

15.2 V, 0.3 A de corriente directa y un tiempo de deposición de 15 min. Como material de aporte se utilizaron nanopartículas de cromo de forma esférica, en estados Cr^0 y Cr^{3+}, con tamaño promedio de 40 nm y concentraciones de 50 ppm y 100 ppm dispersas en agua desionizada. La solución se sometido a agitación constante de 60 rpm para lograr una suspensión y distribución homogénea de las CrNP´s. Los recubrimientos obtenidos fueron caracterizados mediante microscopia electrónica de barrido (SEM) y espectroscopia (EDX) para la determinación de la formación, crecimiento y la composición elemental. Los resultados muestran la formación de un recubrimiento sobre el sustrato; evidenciando la influencia de la concentración del material de aporte. A 50 ppm se observó un bajo deposito en forma de islas "manchas blancas" sobre la superficie del sustrato, en tanto que, para 100 ppm la morfología cambio significativamente; observándose un depósito homogéneo generado por el crecimiento sostenido de las "islas" sobre la superficie. Lo anterior indica que una mayor concentración de nanopartículas favorece la distribución uniforme del recubrimiento, manteniendo constante los parámetros operativos; conduciendo a la formación de un microrelieve homogéneo sobre la superficie tratada.
PALABRAS CLAVE: recubrimientos nanoestructurados; nanopartículas metálicas; electrodeposición; cromo; morfología.

ELECTRODEPOSITION OF NANOSTRUCTURED METALLIC COATINGS

ABSTRACT: The proposed process for the development of nanostructured chromium (CrNP's) coatings on metallic surfaces by means of the electrodeposition technique is presented. This approach is considered an alternative to conventional chromium plating processes based on Cr^{4+} and Cr^{6+} ions, which are recognized as highly toxic to both the environment and human health. Electrodeposition from Cr^0 and Cr^{3+} chromium species in aqueous media represents a sustainable and surface-adaptable process that enhances the mechanical and surface properties of the substrate while reducing environmental impact. The coatings were obtained using an electrolytic cell consisting of a graphite anode and an AISI 1020 steel cathode, applying a direct current of 15.2 V and 0.3 A for a deposition time of 15 minutes. Spherical chromium nanoparticles (CrNP's), in Cr^0 and Cr^{3+} states, with an average size of approximately 40 nm and concentrations of 50 ppm and 100 ppm dispersed in deionized water, were used as the additive material. The solution was subjected to constant agitation at 60 rpm to ensure a homogeneous suspension and uniform distribution of the CrNP's. The obtained coatings were characterized by scanning electron microscopy (SEM) and energy-dispersive X-ray spectroscopy (EDX) to determine coating formation, growth behavior, and elemental composition. The results indicate the formation of a coating layer on the substrate, revealing the influence of nanoparticle concentration. At 50 ppm, a low-density deposit with discontinuous "white island" regions was observed on the substrate surface, whereas at 100 ppm the morphology changed significantly, exhibiting a homogeneous coating generated by the sustained growth and coalescence of these islands. These findings suggest that higher nanoparticle concentrations promote a more uniform coating distribution while maintaining constant operational parameters, leading to the formation of a homogeneous micro-relief on the treated surface.
KEYWORDS: nanostructured coatings; metallic nanoparticles; electrodeposition; chromium; morphology.

1. INTRODUCCIÓN

A nivel industrial los materiales metálicos constituyen uno de los cimientos sobre lo que está construido nuestro desarrollo tecnológico. Estos materiales, tienen una vida limitada que depende en gran medida de fenómenos negativos como desgaste, fricción y corrosión (Pletcher, 1981); los cuales, se han posicionado como uno de los enemigos más perseverantes y silenciosos de los materiales metálicos, alterando sus propiedades y provocan la destrucción de la mayor parte de materiales fabricados por el hombre. Desde el enfoque ingenieril superficial, la causa de estos fenómenos se debe a fallas por la disminución de tolerancias, grandes cargas aplicadas y a las emisiones contaminantes. En los países desarrollados, este tipo de afectaciones ha provocado costosos paros industriales (Toyo, 2023), con estimaciones que indican pérdidas económicas derivadas únicamente de la corrosión representando alrededor del 6% del Producto Interno Bruto (PIB) equivalente a un tercio de los recursos destinados al mantenimiento y producción, lo que se traduce a miles de millones de dólares anuales; sin considerar las perdidas asociadas a los daños ambientales y los riesgos a la salud humana (Bedolla et al., 2025). En el esfuerzo por aminorar estos fenómenos no deseados, ha surgido el interés y la necesidad de implementar alternativas tecnológicas para la protección de superficies metálicas contra efectos de la corrosión, el desgaste y la fricción. En la actualidad, una de las alternativas tecnológicas es la nanotecnología siendo una opción para la elaboración de protecciones y recubrimientos superficiales; aplicados a múltiples campos, como en la industria, en química, medicina, medio ambiente, etc. Diversos nanomateriales han sido empleados para el desarrollo de recubrimientos funcionales, destacando las nanopartículas metálicas por su amplio uso e interés en materiales avanzados. La aplicación de estos recubrimientos superficiales nanoestructurados sobre sustratos metálicos, han mejorado significativamente en las propiedades físico-mecánicas (Texcucano, et al, 2023).

Sin embargo, diversas técnicas de deposición han sido utilizadas para la fabricación de recubrimientos convencionales y nanoestructurados. la electrodeposición es un proceso simple y viable para fabricar una estructura a nanoescala, siempre que las condiciones de parámetros operativos como la densidad de corriente, tiempo de deposición, velocidad de agitación, y en especial la concentración de partículas, contribuyan a una alta cristalización Tey et al. (2021). La nucleación y crecimiento de granos durante la electrodeposición se deriva de procesos de crecimiento de cristales disponibles y de la formación influenciados por el intercambio de carga en la superficie del electrodo y la difusión de iones.

En relación con lo anterior, la incorporación de partículas de cromo, contenidas en una solución acuosa puede lograrse un proceso que no involucre las afectaciones antes mencionadas, disminuyendo accidentes a causa de la preparación del baño electrolítico, una reducción de gases emitidos y la obtención de una capa de metal depositado con espesores a escala nanométrica con propiedades específicas y avanzadas. Por lo cual, la finalidad de este trabajo es el desarrollo de un proceso experimental para la elaboración de recubrimientos nanoestructurados de cromo (CrNP´s) sobre superficies metálicas mediante la técnica de electrodeposición para favorecer la obtención de la formación de un microrelieve homogéneo sobre la superficie tratada.

2. MATERIAL Y METODO

La presente investigación se desarrolló con enfoque experimental, orientado a determinar la presencia y morfología de recubrimientos nanoestructurados electrodepositados a partir de nanopartículas de cromo (CrNP´s). El procedimiento sugerido se fundamenta en la metodología propuesta por Bedolla et al (2022) y adaptado como se muestra a la figura 1.

Figura 1. Metodología sugerida para el desarrollo de recubrimientos metálicos nanoestructurados.

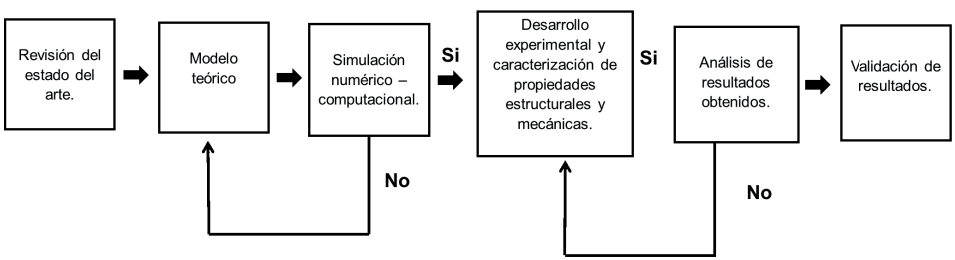

Como se observa en la figura 1, la metodología consta de seis fases, las primeras tres actividades del desarrollo hacen énfasis a la parte teórica y de la etapa tres a la 6 a la fase experimental.

2.1. DESARROLLO EXPERIMENTAL

Se prepararon dos soluciones base con 50 ppm y 100 ppm, dispersando las CrNP´s en 90 ml de agua desionizada. La preparación incluyo un proceso de sonicación durante 10 min para garantizar la homogenización de la suspensión a una temperatura de 23 °C, figura 2.

Figura 2. Baño electrolítico con nanopartículas de cromo CrNP´s.

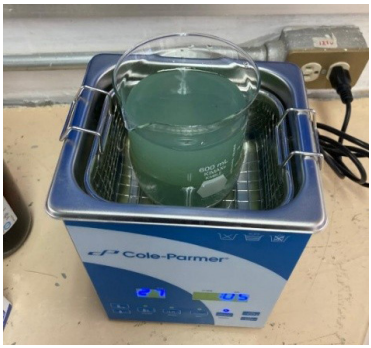

Las probetas de acero AISI 1020, fueron previamente acondicionadas mediante mecanizado de desbaste y pulido, con el fin de obtener un área de 0.0001 m^2 con acabado espejo, ver figura 3. Posteriormente, se realizó un desengrase repetitivo con acetona (C_3H_6O) para eliminar residuos y grasas productos del mecanizado o manipulación, siguiendo el procedimiento descrito por Mahdavi (2015) y evaluadas mediante la prueba de cortina.

El ánodo empleado fue de grafito (C), con un diámetro de 1 cm y longitud de 8 cm, el cual fue limpiado con agua desionizada.

Figura 3. Probetas de acero AISI 1020 mecanizadas y pulidas para pruebas de electrodeposición.

La celda de electrodeposición consistió en un vaso de precipitado (Beaker) donde se conectaron el ánodo (grafito) y el cátodo (AISI 1020) a una fuente de corriente directa (CD). El sistema experimental se monto considerando un agitador magnético con control de velocidad y temperatura (figura a), sobre el cual se coloco el vaso que contiene la solución electrolítica (figura 4b). Los electrodos de trabajo (ánodo y cátodo) se montaron mediante el sistema de sujeción colocándolos en disposición paralela (frente a frente) con una separación de 2 cm (figura 4c). ambos electrodos se conectaron a una fuente regulable de voltaje CD, asignado la terminal positiva para el ánodo y la terminal negativa al cátodo (figura 4d). Posteriormente, los electrodos de trabajo se sumergieron en la solución electrolítica, asegurando el contacto bajo una línea de espejo de la solución.

El agitador magnético se activó para mantener la homogeneidad de la mezcla y posteriormente se encendió la fuente de alimentación para iniciar la electrodeposición.

Figura 4. Banco experimental de electrodeposición y disposición física de componente: (a) fuente de corriente, (b) Beaker con solución electrolítica, (c) porta-electrodos, (d) conexión de ánodo y cátodo.

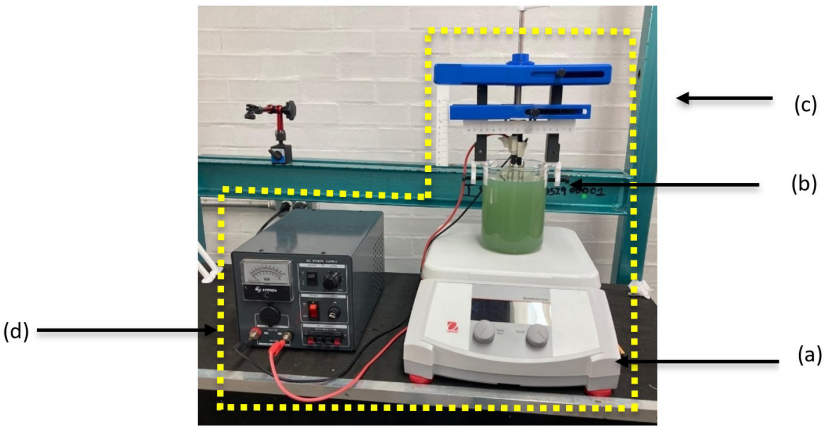

Una vez preparado el baño electrolítico, las probetas y el banco de pruebas experimental, se procedió al desarrollo de electrodeposición, considerando los siguientes parámetros operativos que se muestran en la Tabla 1 y Tabla 2.

Una vez concluidos los pasos descritos anteriormente, se procedió a realizar la fase experimental de recubrimiento, suministrando el voltaje y la corriente requeridos al baño electrolíticos, conforme a los valores establecidos en las Tablas 1 y 2, así como los tiempos asignados a cada muestra.

Transcurrido el tiempo correspondiente para cada muestra, el proceso de electrodeposición termina y cada muestra fue retira de la celda electrolítica para su lavado con agua desionizada, con el objetivo de eliminar los residuos del baño electrolítico. Para cada electrodepósito se empleó una nueva solución electrolítica de 90 ml. Como resultado, se obtuvieron 5 probetas de acero AISI 1020, los recubrimientos obtenidos se sometieron a caracterización morfológica y superficial.

Tabla 1. Parámetros para realizar pruebas experimentales para MUESTRAS A, 50 ppm.

Parámetro		Valor
Corriente		0.3 A
Voltaje		15.2 v
Tiempo	Agitación	60 rpm
	MUESTRA A-2	300 seg
	MUESTRA A-3	600 seg
	MUESTRA A-4	900 seg

Tabla 2. Parámetros para realizar pruebas experimentales para MUESTRAS B, 100 ppm.

Parámetro		Valor
Corriente		0.3 A
Voltaje		15.2 v
Tiempo	Agitación	60 rpm
	MUESTRA B-1	300 seg
	MUESTRA B-2	600 seg
	MUESTRA B-3	3600 seg

2.2. CARACTERIZACIÓN ESTRUCTURAL DE MUESTRAS

Los recubrimientos se caracterizaron mediante microscopia electrónico de barrido (SEM) utilizando un microscopio HITACHI S-3000 N, con aumentos que variaron desde 45X hasta 1000X, voltaje de aceleración para los electrones (Hv) de 20 Kv y una distancia de trabajo (WD) de 15 mm a una escala de 600 µm. Mediante esta técnica se determinó la morfología, perfil de distribución y estructura de los depósitos. Para la observación de la composición elemental se utilizó Espectroscopia de Rayos X Dispersados (EDS), mediante un difractómetro BRUKER INCAx- sight, con una radiación CuKa, λ= 0.154 nm y un intervalo 2θ de 4 a 90° para el barrido.

3. RESULTADOS

El procesamiento y evaluación de los datos experimentales correspondientes a las muestras analizadas, con el fin de determinar el efecto de los parámetros de electrodeposición en la formación y crecimiento del nanorecubrimiento.

3.1. FORMACIÓN Y CRECIMIENTO DEL NANORECUBRIMIENTO

De acuerdo con la figura 5, la muestra A-4 correspondiente a una concentración de 50 ppm y un tiempo de deposición de 900 segundos, presenta en la micrografía un bajo deposito caracterizado por la aparición de “manchas blancas”, visibles en la parte derecha y en la parte superior izquierda de la figura 5a. En contraste, la morfología obtenida en la muestra B-1, figura 5b difiere del depósito de la muestra A-4. Este cambio atribuye al incremento en la concentración del material de aporte a 100 ppm y a la reducción del tiempo de deposición a 300 seg. Observando un depósito no homogéneo, con formación de nódulos localizados sobre sitios de adsorción más estables de la superficie de hierro (Fe).

Figura 5. Micrografía de la Muestra A-4 y Muestra B-1.

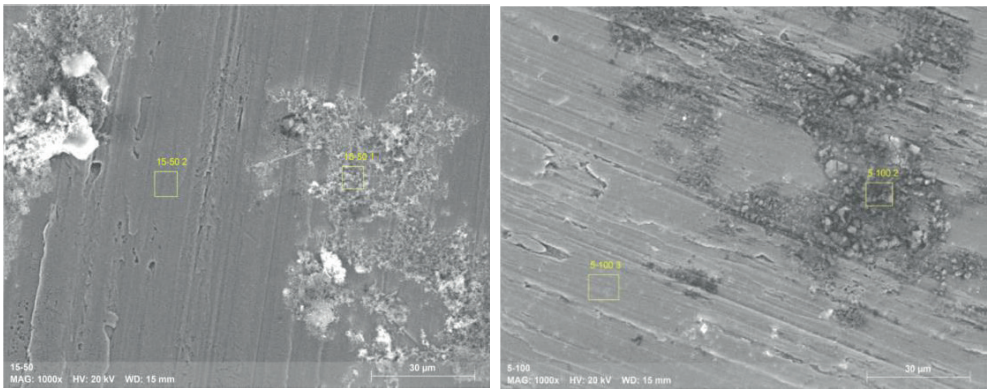

Respecto a la micrografía mostrada en la figura 6, se aprecia una comparación en el tamaño y distribución de las muestras analizadas. En la muestra B-2 se observa una ocupación más dispersa sobre una misma área, en contraste con la muestra B-3, cuya superficie presenta una morfología más definida. Esta diferencia se atribuye a la escala de observación utilizada (600 µm) para ambas muestras. En la figura 3a se observa un depósito de baja densidad, aun cuando se incrementó la concentración de CrNP´s y el tiempo de deposición a 600 segundos. No obstante, se distingue un cambio en la morfología del recubrimiento de la muestra B-3 en comparación con las muestras A-1, B-1 y B-2.

Por otro lado, la figura 6b muestra la micrografía correspondiente a una concentración de 100 ppm de CrNP´s y un tiempo de deposición de 3600 segundos. En esta se observa un depósito más denso y homogéneo, figura 6b, Donde la morfología presenta “islas de crecimiento” y una distribución más definida de las nanopartículas, indicando un proceso de nucleación y crecimiento más estable en la superficie.

Figura 6. (a) Muestra a concentración 50 ppm y (b) Muestra a concentración 100 ppm.

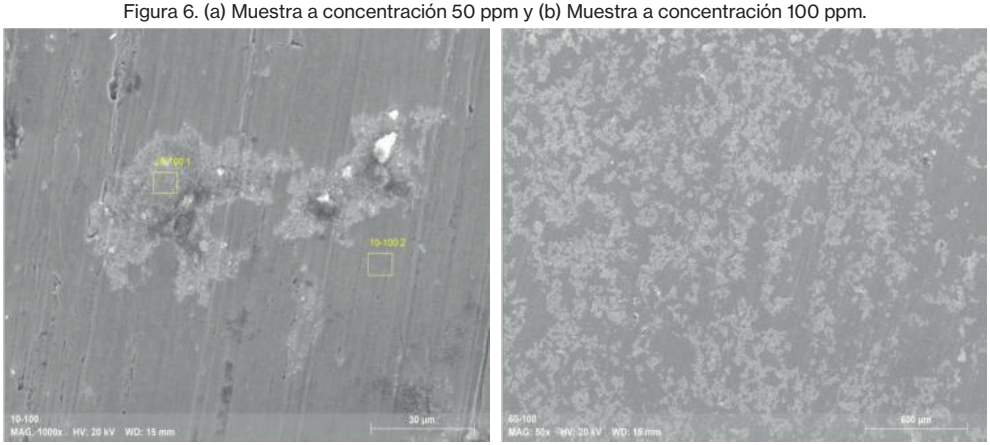

3.2. CARACTERIZACIÓN DE COMPOSICIÓN ELEMENTAL

De acuerdo, al análisis químico superficial (EDX), las muestras A-4 y B-3 fueron seleccionas como las más representativas. Las figuras 7 y 8 muestran los microanálisis correspondientes a cada una.

Figura. 7 microanálisis de la Muestra A-4.

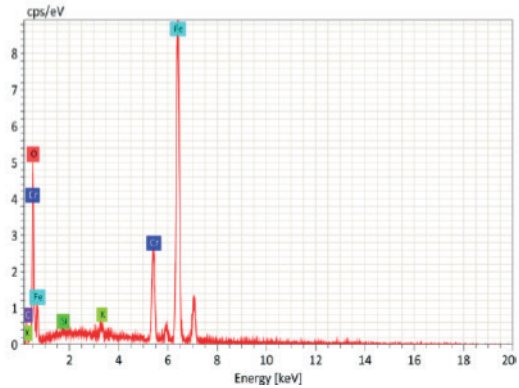

Element	Line s.	Mass Norm. [%]	Atom [%]	abs. error [%] (1 sigma)
C	K-Serie	11,46	31,89	2,88
O	K-Serie	9,93	20,75	1,96
K	K-Serie	0,91	0,78	0,09
Cr	K-Serie	1,37	0,88	0,11
Mn	K-Serie	0,52	0,31	0,10
Fe	K-Serie	75,82	45,39	1,98
		100.00	100.00	

Figura. 8 microanálisis de la Muestra B-3.

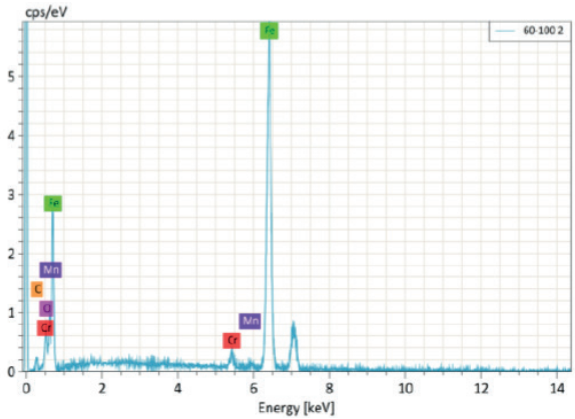

Element	Line s.	Mass Norm. [%]	Atom [%]	abs. error [%] (1 sigma)
C	K-Serie	4,39	16,26	1,81
O	K-Serie	3,70	10,31	1,09
Cr	K-Serie	2,12	1,82	0,14
Mn	K-Serie	0,47	0,38	0,11
Fe	K-Serie	89,33	71,24	2,48
		100,00	100,00	

De acuerdo con la evaluación de la composición elemental y el porcentaje de material de aporte (CrNP´s), la micrografía de la muestra A-4 evidencia la presencia de elementos característicos del sustrato utilizado. Se detectó un contenido de cromo del 1.37 %, atribuible a la incorporación de CrNP´s desde la solución electrolítica. Asimismo, se observó la presencia de oxígeno (O), posiblemente en forma de óxido de cromo (Cr_2O_3) reportado por Palomera (2008).

En el microanálisis correspondiente a la muestra B-3 se identificó una composición elemental más localizada, con picos de mayor intensidad y una distribución heterogénea. El comportamiento se asocia al incremento en la concentración de CrNP´s, lo que

favorece un mayor depósito del recubrimiento, alcanzando un 2.12 % de cromo sobre la superficie. De igual manera, se detectó oxígeno, el cual podría estar presente como óxido de cromo. En ambos casos se observan los elementos característicos del sustrato metálico, evidenciando la relación existente entre la concentración del material de aporte, el tiempo de deposición y la cantidad de cromo incorporado en el recubrimiento.

4. CONCLUSIONES

De acuerdo con lo anterior, la influencia de los parámetros operativos influye en la nucleación y crecimiento del recubrimiento; en el caso específico de la concentración del material de aporte se observó que, a bajas concentraciones, el proceso de nucleación es limitada, obteniendo depósitos caracterizado por la aparición de "manchas blancas" sobre la superficie del sustrato, reflejando un crecimiento restringido. Sin embargo, al incrementar la concentración se observa un crecimiento sostenido en forma de "islas de crecimiento", que favorecen la formación de un microrelieve con apariencia homogénea; lo cual permite inferir que la deposición se inicia en las zonas energéticamente más estables localizadas sobre el sustrato, favoreciendo la adherencia del depósito.

REFERENCIAS BIBLIOGRÁFICAS

Bedolla Hernández, M., Sánchez Parra, L. F., Díaz Domínguez, J., & Texcucano Romano, G. (2025). *Estudio experimental del efecto de la agitación mecánica de la solución electrolítica en la formación de recubrimientos nanoestructurados*. En *Artículos del Congreso Internacional de Investigación Academia Journals Chetumal 2025* (pp. XX–XX). Academia Journals. Chetumal, Quintana Roo, México. © Academia Journals 2025.

Bedolla-Hernández, J., Schabes-Retchkiman, P. S., & Vega-Lebrún, C. A. (2022). *Electrodeposition mechanism of chromium nanoparticle coatings: Modeling and experimental validation*. *Chemical Engineering Science, 252*, 117291.

Mahdavi, S., & Allahkaram, S. R. (2015). *Investigation of tribological behavior of electrodeposited Cr, Co–Cr and Co–Cr/TiO_2 nanocomposite coatings*. *World Academy of Science, Engineering and Technology, International Journal of Chemical, Molecular, Nuclear, Materials and Metallurgical Engineering, 9*(7), 747–751.

Pletcher, D. (1981). *Industrial electrochemistry*. New York: Chapman & Hall.

Palomera Duarte, W. R. (2008). *Estudio de la reducción de soluciones de cromo hexavalente a cromo trivalente en un medio ácido* [Tesis de licenciatura, Centro de Investigación y Desarrollo Tecnológico en Electroquímica (CIDETEQ)]. CIDETEQ.

Tey, E., Z. Zainal, L. K. Pah y I. Ismail. ¨Effect of Mechanical Agitation on Cr-Al2O3 Nanocomposite Coatings Fabricated from Trivalent Chromium Electrodeposition,¨ *Solid State Phenomen,* Vol. 317, Trans Tech Publications, Ltd. 2021. https://doi.org/10.4028/www.scientific.net/ssp.317.506.

Texcucano, G., Bedolla, M., Bedolla, J., Sánchez, E., Colín, F., Aguilar, J., & Rosano-Ortega, G. (2023, noviembre 8–10). *Efectos de la concentración del material de aporte en la formación y crecimiento de recubrimientos nanoestructurados con cromo*. En *SOMI XXXVII Congreso de Instrumentación*. Bogotá, Colombia.

Toyo, M. (2023). *La corrosión: El enemigo invisible de la industria*. INSPENET. Recuperado el 15 de mayo de 2025, de https://www.inspenet.com

CHAPTER 5

CYTOTOXIC EFFECT OF PUMPKIN SEED OIL-LOADED NANOEMULSION IN BREAST CANCER CELL LINES

Data de submissão: 29/10/2025
Data de aceite: 17/11/2025

Guilherme Diniz Tavares
Universidade Federal de Juiz de Fora
Departamento de Ciências Farmacêuticas
Juiz de Fora, Minas Gerais, Brasil
https://orcid.org/0000-0001-6276-0994

Anelise Pereira Alves
Universidade Federal de Juiz de Fora
Departamento de Ciências Farmacêuticas
Juiz de Fora, Minas Gerais, Brasil
https://orcid.org/0009-0003-4750-4839

Fabiano Freire Costa
Universidade Federal de Juiz de Fora
Departamento de Ciências Farmacêuticas
Juiz de Fora, Minas Gerais, Brasil
https://orcid.org/0000-0002-7206-6792

Wanderleya Toledo dos Santos
Universidade Federal de Juiz de Fora
Departamento de Ciências Farmacêuticas
Juiz de Fora, Minas Gerais, Brasil
https://orcid.org/0000-0001-9693-8738

Paula Rocha Chellini
Universidade Federal de Juiz de Fora
Departamento de Ciências Farmacêuticas
Juiz de Fora, Minas Gerais, Brasil
https://orcid.org/0000-0001-8927-446X

Daniel Augusto de Andrade
Universidade Federal de Juiz de Fora
Departamento de Ciências Farmacêuticas
Juiz de Fora, Minas Gerais, Brasil
https://orcid.org/0009-0009-3878-4553

Ana Cláudia Chagas de Paula
Universidade Federal de Juiz de Fora
Departamento de Ciências Farmacêuticas
Juiz de Fora, Minas Gerais, Brasil
https://orcid.org/0000-0001-7998-0950

Felipe Kelmer Müller
Universidade Federal de Juiz de Fora
Departamento de Ciências Farmacêuticas
Juiz de Fora, Minas Gerais, Brasil
https://orcid.org/0009-0000-1330-5055

Kézia Cristine Barbosa Ferreira
Universidade Federal de Juiz de Fora
Departamento de Ciências Farmacêuticas
Juiz de Fora, Minas Gerais, Brasil
https://orcid.org/0000-0002-0545-6934

ABSTRACT: Breast cancer has the highest mortality rate in women worldwide and current treatments have many side effects. Thus, nutraceuticals and nanomedicine aim to improve the quality of life and the effectiveness of conventional treatments. In this sense, this work aimed to evaluate the cytotoxic effect of a *Cucurbita moschata* pumpkin seed oil-loaded nanoemulsion (PSO-N) in metastatic

breast cancer cells (MCF-7). The oil was obtained by cold pressing and characterized by gas chromatography (GC). The PSO-N was prepared using a high-energy emulsification method. The PSO-N was characterized regarding Z-average, PdI, ZP, and pH. Also, a stability study was conducted for 3 months. A cytotoxicity assay was performed by MTT in concentrations of 500 - 3000 µg. mL^{-1}. It was identified a greater proportion of linoleic acid (51.55%). The nanoemulsion with the best stability parameters had HLB 13, Z-average = 149.99 ± 9.95 nm, PdI = 0.14 ± 0.03 and ZP of 22.39 ± 3.19 mV and the best storage condition is at 4 ºC. The nanoemulsion was cytotoxic for MCF-7 cells at a concentration of 500 µg.mL^{-1}. In view of the results, PSO-N has an adequate physical-chemical characteristics and a promissory activity for breast cancer treatment.
KEYWORDS: emulsions; inflammatory breast neoplasms; *cucurbita moschata*; toxicity tests.

EFEITO CITOTÓXICO DE NANOEMULSÃO CONTENDO ÓLEO DE SEMENTE DE ABÓBORA EM LINHAGENS DE CÉLULAS DE CÂNCER DE MAMA

RESUMO: O câncer de mama apresenta a maior taxa de mortalidade entre mulheres em todo o mundo, e os tratamentos atuais possuem muitos efeitos colaterais. Assim, nutracêuticos e a nanomedicina visam melhorar a qualidade de vida e a eficácia dos tratamentos convencionais. Nesse sentido, este trabalho teve como objetivo avaliar o efeito citotóxico de uma nanoemulsão contendo óleo de semente de abóbora *Cucurbita moschata* (PSO-N) em células de câncer de mama metastático (MCF-7). O óleo foi obtido por prensagem a frio e caracterizado por cromatografia gasosa (CG). A PSO-N foi preparada utilizando um método de emulsificação de alta energia. A PSO-N foi caracterizada quanto ao tamanho hidrodinâmico médio, PdI, ZP e pH. Além disso, um estudo de estabilidade foi conduzido durante 3 meses. O ensaio de citotoxicidade foi realizado pelo método MTT em concentrações de 500 a 3000 µg mL^{-1}. Foi identificada uma maior proporção de ácido linoleico (51,55%). A nanoemulsão com os melhores parâmetros de estabilidade apresentou HLB 13, Z-médio = 149,99 ± 9,95 nm, PdI = 0,14 ± 0,03 e ZP de 22,39 ± 3,19 mV, sendo a melhor condição de armazenamento a 4 °C. A nanoemulsão demonstrou citotoxicidade para células MCF-7 na concentração de 500 µg.mL^{-1}. Diante dos resultados, a PSO-N apresenta características químicas adequadas e atividade promissora para o tratamento do câncer de mama.
PALAVRAS-CHAVE: emulsões; neoplasias Inflamatórias da mama; *cucurbita moschata*; testes de toxicidade.

1. INTRODUCTION

Breast cancer is the most frequent cancer with the greatest causes of cancer death in women worldwide with an estimated 2.3 million new cases (11.7%), and is therefore a public health problem (Kashyap *et al*., 2022; Sung *et al*., 2021). Treatments for breast cancer include pharmacological treatment, surgery, chemotherapy or radiation and will depend on the stage of cancer (Rossi *et al*., 2018; Waks, Winer, 2019). Most of these

treatments have serious side effects, which decrease the patient's quality of life. This occurs because the drugs have molecules small enough to pass through the endothelium of several nonspecific regions (Vieira, Gamarra, 2016). In this sense, nutraceuticals and nanomedicine come together with conventional treatments to improve cancer therapies (Puttasiddaiah *et al*., 2022). Nutraceuticals are attractive because their reduced side effects, especially in cancer (Maiuolo *et al*., 2021), beneficial health effects and their reduced cost (Chauhan *et al*., 2013). Besides, nanomedicine appears to be a boost technology in medicine, through the improvement of treatments and diagnosis, using nanomaterials which can permeate and accumulate in solid tumors through a mechanism called enhanced permeability and retention effect (EPR) (Huang *et al*., 2021; Wu, 2021). This means that the tumor microenvironment provides an increased vascular permeability, because in inflamed regions or tumoral regions, cells are more spaced apart, unlike healthy cells, this allows nanoparticles to accumulate in these tumoral tissues (Farokhzad, Langer, 2009; Garbayo *et al*., 2020).

Cucurbita moschata is a species of pumpkin, belonging to the family Cucurbitaceae, widely cultivated and consumed in the world. Its seeds are generally considered to be agro-industrial residues, however, they have several bioactive compounds in their composition, being of great interest in health (Men et al., 2021; Veronezi, Jorge, 2012). They contain fatty acids, carotenoids, phenolic acids, tocopherols, flavonoids, minerals and vitamins (de Carvalho *et al*., 2012; Peiretti *et al*., 2017) being able to exercise the various biological activities already reported, such as antidiabetic, and cardioprotective action (Patel, 2013; Uuh-Narvaez *et al*., 2021).

In addition to these compounds, the literature describes the presence of a substance called moschatin, characterized as a type I ribosome inactivating protein (RIP I) in the mature seeds of *Cucurbita moschata*, which shows cytotoxic activity in human melanoma cells (Xia *et al*., 2003). It is reported the presence of highly oxygenated triterpene structures, called cucurbitacins, which have shown cytotoxicity, antitumoral, hepatoprotective and anti-inflammatory activity. In the seeds of *Cucurbita moschata*, there is the presence of cucurbitacin B, one of the main substances with cytotoxic activity (Montesano *et al*., 2018).

Therefore, we report herein the development of a pumpkin seed oil nanoemulsion, its long-term stability characterization and the evaluation of its cytotoxic effect in metastatic breast cancer cells.

2. MATERIAL AND METHODS

2.1. PUMPKIN SEED OIL EXTRACTION

For this work, fresh seeds of *Cucurbita moschata* (20°49'3,28"S and 45°8'1,31"W) were peeled off and subjected to cold pressing. The oil was subjected to centrifugation (Kasvi K14-4000) at 3000 rpm for 30 minutes. The yield was calculated by the ratio of the mass of the oil to the mass of the seed. This study was registered in the National System for Governance of Genetic Heritage and Associated Tradicional Knowledge (SisGen # AA91593).

2.2. CHARACTERIZATION OF PUMPKIN SEED OIL

Approximately 1mg of *C. moschata* seed oil was dissolved in 100 µL of a solution of sodium hydroxide 1 mol.L^{-1} in ethanol/water (95:5 v/v). After vortexing for 10 s, the oil was hydrolyzed through heating and vibration generated by electromagnetic waves at 30% power for 4 minutes. After cooling, 400 µL of 20% hydrochloric acid, 4µg NaCl and 600 µL of ethyl acetate were added. After vortexing for 10 s and standing for 5 min, an aliquot of 300 µL total of the organic layer was removed and dried by evaporation, thus obtaining free fatty acids (Sande *et al*., 2018). Subsequently, the free fatty acids were methylated with 100 µL BF3 / methanol (14%) by heating for 10 minutes in a water bath at 60 ºC, extracted in 500 µL of hexane and analyzed by Gas Chromatography. The analyzes were performed on an HP7820A Gas Chromatograph (Agilent) equipped with a flame ionization detector. A Supelcowax-10 30 m x 0.2 mm x 0.2 µm column (Supelco) with the following temperature gradient 150 ºC, 1 min, 10 ºC.min-1 to 240 ºC was used; injector (1/20 split) at 250 ºC and detector at 250 ºC. Hydrogen as carrier gas (6 mL.min^{-1}) and injection volume of 1 µL. Peak identification was done by comparison with FAME C14-C22 methylated fatty acid standards (Supelco #18917).

2.3. HLB DETERMINATION

Nanoemulsions with HLB 8.7; 10.9; 12 and 13 containing a percentage of 5% w/w oil, 5% surfactants and 90% water were prepared. The surfactants chosen for the preparation of the emulsions were sorbitan monooleate (Span® 80) and ethoxylated sorbitan monooleate (Tween® 80). After preparing the nanoemulsions, they were evaluated for their preliminary stability by submitting to centrifugations at 1000, 2000 and 3000 rpm for 15 minutes (Kasvi K14-4000). The nanoemulsion that presented the best macroscopic characteristics and did not have phase separation was selected for the next experiments.

2.4. PREPARATION OF NANOEMULSION

HBL 13 nanoemulsion was developed containing a percentage of 5% oil and 5% surfactants (Tween® 80 and Span® 80). All emulsions were prepared by the high energy method, in which the aqueous phase and the oil phase were prepared separately. After the preparation of each phase, the aqueous phase was slowly poured into the oil phase under magnetic stirring (MS300 Magnetic Stirrer) at 786 rpm at 50 ºC. The stirring was maintained until reaching room temperature. The emulsion was then subjected to ultrasonic processor at 20 kHz, 85% amplitude, for 5 minutes (Ultrasonics). An illustrative scheme of the preparation of the nanoemulsions is available in Figure 1.

Figure 1. Summary of the main steps concerning the methodology of the nanoemulsions preparation. Created with Blender 3D.

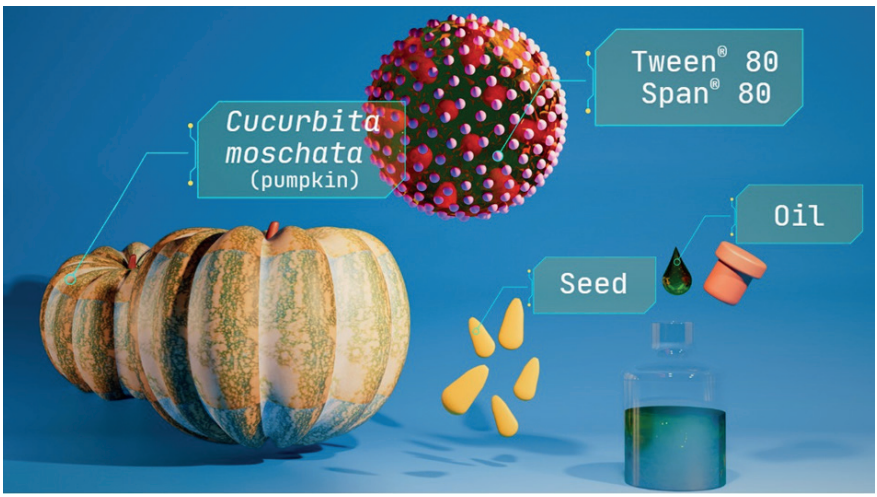

2.5. CHARACTERIZATION OF THE PHYSICAL-CHEMICAL PARAMETERS OF THE NANOEMULSION

The mean particle size (Z-average) and polydispersity index (PdI) were measured by Dynamic Light Scattering using a Zetasizer Nanoseries (Malvern Instruments, Worcestershire, United Kingdom). The analysis were performed at 25 °C, with a detection angle of 173°. The zeta potential (ZP) values were obtained by electrophoretic mobility (Zetasizer Nanoseries, Malvern Instruments, Worcestershire, United Kingdom). Prior to the analyses, samples were diluted in ultrapure water (1:400). The pH was directly determined in the samples (PH-2011, Etekcity, Anaheim, California, USA). The analyses were performed in triplicate.

2.6. STORAGE STABILITY STUDY

The nanoemulsion was stored in different 15 mL flasks, at temperatures of 4, 27 and 45 ºC for 0, 7, 15, 30, 60 and 90 days. After each time the samples were analyzed for the following parameters: Z-average, PdI, PZ and pH. The analyzes were performed in triplicates.

2.7. PREPARATION OF SUBSTANCES

From the three stocks: 10.000, 5000 and 1000 $\mu g.mL^{-1}$ the substances were diluted to the final concentration of 50, 100, 500, 1500 and 3000 $\mu g.mL^{-1}$. Then, the substances were diluted in Tween® 80, 1%, diluted in Dulbecco´s modified eagle medium (DMEM). For the oil control substance with ethanol (EtOH), the oil was diluted in 2% ethanol.

2.8. CYTOTOXICITY STUDY (MTT ASSAY)

The control and test formulations were submitted to sterilization by UV light for 15 minutes. Samples were prepared to the final concentration of 50, 100, 500, 1500 and 3000 $\mu g.mL^{-1}$, diluted in Tween® 80, 1%, at Dulbecco´s modified eagle medium (DMEM). For the oil control substance with ethanol (EtOH), the oil was diluted in 2% ethanol. MCF-7 and human fibroblast cells were seeded $1x10^{-4}$ cells/well in 96-well plates in the DMEM essential medium with L-glutamine (2mM) supplemented with 10% fetal bovine serum and 1% penicillin/streptomycin and maintained at 37 ºC in a 5% CO_2 in incubator (Thermo Scientific) After 24h of incubation, the cells were incubated with the test and control samples (nanoemulsion without the oil) at concentrations of 50, 500 1500 and 3000 $\mu g.mL^{-1}$. Additionally, free oil, oil with 2% ethanol, 2% ethanol and 2% DMSO (for a negative control) were applied to the cells. After 24 and 48 hours, the medium was discarded and 100 µL of MTT solution 5 $mg.mL^{-1}$ (Sigma) was added, according to the manufacturer's guidelines. Then, the plates were incubated at 37 ºC for 4 h. After the incubation time, the formation of formazan crystals was observed under an optical microscope, all medium was discarded and added 100 µL of 0.05 M HCl isopropanol solution for dissolution of the formazan crystals and optical density was measured at 570 nm and 645 nm in the spectrophotometer (Multiskan Go).

2.9. STATISTICAL ANALYSIS

The statistical analyzes were performed by using Graph Pad Prism 5.0. Analyzes of the stability study were carried out by comparing the different groups (Two-way ANOVA and Bonferroni) and in relation to the control group (T0) (Two-way ANOVA followed by the

Dunnett test). The MTT assay analyzes were performed comparing the different groups (Two-way ANOVA followed by the Bonferroni test). Values were presented as mean ± standard error of the mean. Statistical differences were considered significant at $p < 0.05$.

3. RESULTS

The yield percentage of pumpkin seed oil was 24.12% using cold pressing. The yield was calculated by the ratio of the mass of the oil to the mass of the seed. The chromatogram profile of pumpkin seed oil characterization (Table 1) revealed that the fatty acids most present in pumpkin seed oil were C18:2 (linoleic acid; 51.55%), C18:1 (oleic acid; 20.06%), C16:0 (palmitic; 15.66%) and C18:0 (stearic acid; 10.67%).

Table 1. The fatty acids profile of Curcubita moschata seed oil. (RT = Real Time; PSO = pumpkin seed oil-loaded).

Fatty acids	RT (min)	PSO (area)	PSO (%)
C12:0	3.137	12704	0.05
C14:0	4.308	44596	0.17
C16:0	6.315	4039395	15.66
C16:1	6.592	117485	0.46
C18:0	7.991	2753472	10.67
C18:1	8.185	5176699	20.06
C18:2	8.603	13301592	51.55
C18:3	9.107	63869	0.25
C20:0	9.587	146501	0.57
others		245752	0.56

To obtain the nanoemulsion with better physicochemical characteristics and greater stability, formulations with different HLB values were evaluated in terms of macroscopic appearance, particle size (Z-average), polydispersity index (PdI) and zeta potential (ZP) (Table 2). In this sense, the nanoemulsion with HLB = 13 presented the best parameters: Z-average 149.99 ± 9.95 nm, monodisperse population PdI = 0.14 ± 0.03 and ZP of 22.39 ± 3.19 mV.

Table 2. Characterization of the physical-chemical parameters of the nanoemulsions. (HLB = Hydrophilic-Lipophilic Balance; Z-average = Particle Size, PdI = Polydispersity Index; ZP = Zeta Potential).

Composition	Formulation	HLB	Microscopic aspect	Span 80 (%w/w)	Tween 80 (%w/w)	Z-avarage (nm)	PdI	ZP (mV)
	1	8.7	Increased sedimentation	59	41	196.73	0.24	-30.22

5% oil and 5% surfactants	**2**	10.9	Increased sedimentation	38	62	157.31	0.17	-12.51
	3	12	Low sedimentation	28	72	151.44	0.24	-23.61
	4	13	Low sedimentation	18	82	149.99	0.14	-22.39

The stability test carried out at 4 ºC, 27 ºC and 45 ºC revealed relative stability of the formulation at 4 ºC and 27 ºC.). A slight decrease in the mean Z was observed at 30 and 90 days at temperatures of 4 ºC and 27 ºC. The mean Z increased after 90 days at 45 ºC with a peak at 60 days with the particle measuring 245.4 nm. These results are available in function of time, as shown in Figure 2.

No significant difference was observed in the polydispersity index over time at 4 ºC and 27 ºC, but the polydispersity index also varied over the 90 days at a temperature of 45 ºC in relation to the 4 ºC and 27 ºC groups and in relation to the T0. However, during the 90 days, this parameter remained below 0.3 at all temperatures, guaranteeing the characteristics of a monodisperse population.

Furthermore, our results demonstrated variations in zeta potential at all temperatures over time. In this sense, the temperature that came closest to a suitable zeta potential parameter was 4 ºC, as it was the temperature that had the least variations and was close to ± 30mV.

Figure 2. Storage stability characterization at 4 ºC, 27 ºC and 45 ºC for 90 days. Evaluation of the (a) hydrodynamic diameter; (b) polydispersity index; (c) zeta potential; (d) pH. * $p < 0.05$ between groups 4 °C and 27 °C; ϕ $p < 0.05$ between 4 °C and 45 °C; # $p < 0.05$ between 27 °C and 45 °C; ψ $p < 0.05$: compared to T0.

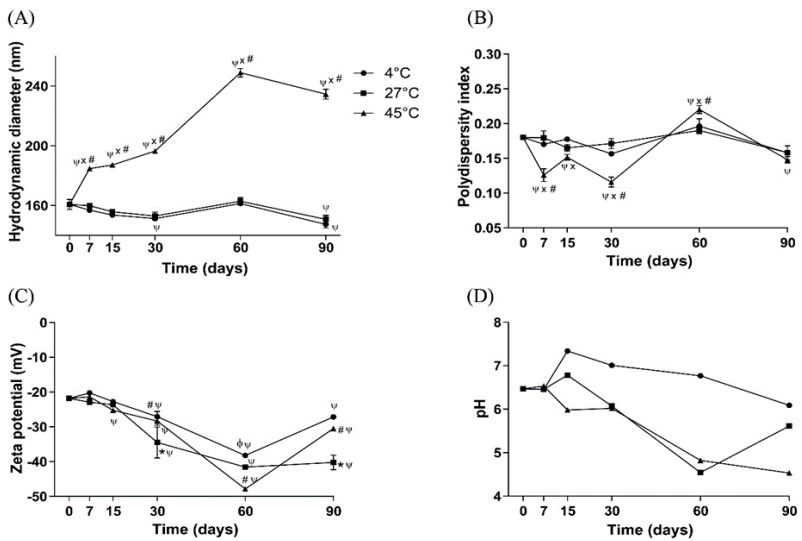

pH decreased at all temperatures over time, but there was no statistical difference between groups. The results demonstrated a decrease in cell viability of more than 50% for MCF-7 cells at concentrations of 500, 1,500 and 3,000 µg.mL-1. However, concentrations of 1,500 and 3,000 µg.mL-1 also showed cytotoxicity in the control nanoemulsion. It is important to highlight that the nanoemulsion was not cytotoxic to fibroblasts at a concentration of 500 µg.mL-1, but it was also cytotoxic at concentrations of 1,500 and 3,000 µg.mL-1 in both the test and control groups.

4. DISCUSSION

According to the literature, pumpkin seed oil content varies between 42 to 54%(Murkovic *et al*., 2004). However, the work of Kabutey and collaborators obtained a percentage of 13.37% in yield by cold pressing of pumpkin seeds, which shows that we had a good yield taking into account the method used.

The variation in the oil content as well as the fatty acid profile may be due to differences in the cultivation of the plant and its varieties, stage of maturation, seed harvesting time and extraction method (Nyam *et al*., 2009). Our analyzes revealed a higher percentage of linoleic acid, which corroborates the results of Durante *et al*. (2014) who also observed a higher percentage of linoleic acid, being the main fatty acid, followed by oleic acid, in *Cucurbita moschata* pumpkin seed oil. The same was observed in the study by Puscas *et al*., 2022.

The higher linoleic acid content in the oil is attractive. A meta-analysis study suggests that dietary linoleic acid consumption is associated with a decreased risk of breast cancer, however, without any statistically relevant association (Zhou *et al*., 2016). Furthermore, in in vivo and in vitro models, dietary conjugated linoleic acid (CLA) was able to inhibit the development of carcinogenesis at multiple sites (Lee et al., 2005) and its activity delayed the growth of breast cancer cells. breast MCF-7. in an in vitro study (Bocca *et al*., 2010). From a chemical point of view, the high percentage of linoleic acid increases the risk of oil oxidation, which can lead to a decrease in the stability of the system (Rezig *et al*., 2012).

To obtain the nanoemulsion with better physicochemical characteristics and greater stability, formulations with different HLB values were evaluated in terms of macroscopic aspect, particle size (Z-average), polydispersity index (PdI) and zeta potential (ZP) (TABLE II). In this sense, the nanoemulsion with HLB = 13 presented the best parameters: Z-average 149.99 ± 9.95 nm, monodisperse population PdI = 0.14 ± 0.03 and ZP of 22.39 ± 3.19 mV. The literature indicates that nanostructures with an average

diameter close to 200 nm more easily penetrate the fenestrations of the tumor vascular epithelium (Liechty & Peppas, 2012); Danaei *et al*., 2018). Furthermore, nanoparticles that exhibit ZP close to ±30 mV exhibit greater colloidal stability (Roland *et al*., 2003); Kurpiers *et al*., 2020).

The pH can also be a parameter for monitoring the stability of the formulation, as changes in its values can indicate bacterial growth or chemical reactions. The pH decreased at all temperatures over time, but there was no statistical difference between the groups (Figure 2D), which in turn can be explained by oxidative reactions, generating free fatty acids that increase the negative charge of the system. Formulations with a high concentration of fatty acids are more susceptible to oxidation reactions, such as hydrolysis, changing pH values (Musakhanian *et al*., 2022) .

Over the 90 days of study, there was no break in the formulation, ensuring stability. At a temperature of 45 ºC, more parameters were changed over time, as expected, since many reactions and physicochemical changes occur at high temperatures. At temperatures of 4 ºC and 27 ºC, the nanoemulsion maintained its adequate physicochemical parameters. However, at 27 ºC a slight change in color was observed, losing the greenish characteristics of the oil and showing greater apparent sedimentation, in addition to a more pronounced variation in zeta potential in relation to 4 ºC. Thus, together, the best storage temperature for the pumpkin seed oil nanoemulsion was 4 ºC, which managed to keep its physicochemical characteristics closer to ideal.

Figure 3. Cell viability evaluated by MTT assay performed at 24 and 48h after pumpkim seed oil nanoemulsion treatment. The representative image of cell morphology and viability of (a) MCF-7 and (b) fibroblast. Statistical differences determined between the groups were determined according to ANOVA followed by the Bonferroni test * p <0.05. Scale bar: 100 µm. CC: cell control; FO: free oil; OETOH: oil diluted in 2% ethanol; ETOH: 2% ethanol; PSO-NE: pumpkin seed oil nanoemulsion; CT-NE: control nanoemulsion (without oil).

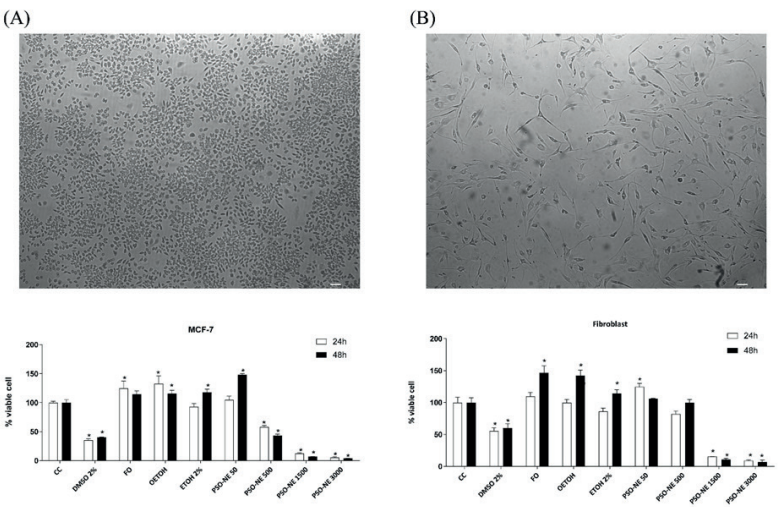

The cytotoxic potential of pumpkin seed oil nanoemulsion was evaluated using the MTT assay. The results demonstrated a decrease in cell viability of more than 50% for MCF-7 cells at concentrations of 500, 1,500 and 3,000 µg.mL-1 (Figure 3A). However, concentrations of 1,500 and 3,000 µg.mL-1 also showed cytotoxicity in the control nanoemulsion. It is important to highlight that the nanoemulsion was not cytotoxic to fibroblasts at a concentration of 500 µg.mL-1, but it was also cytotoxic at concentrations of 1,500 and 3,000 µg.mL-1 in both the test and control groups (Figure 3B).

This result demonstrates that the developed pumpkin seed oil nanoemulsion is cytotoxic to MCF-7 metastasis-derived breast cancer cells and not to fibroblasts (control cells). The biological activity of pumpkin seed oil nanoemulsion may be due to RIP, called moschatin, present in *C. moschata* pumpkin seeds, which also showed cytotoxic activity in M21 human melanoma cells (Chuan Xia *et al*., 2003)The other hypothesis related to the observed biological activity would be the presence of cucurbitacins in pumpkin seeds, which have cytotoxic and antitumor activity and specifically Cucurbitacin B, present in *C. moschata* pumpkin seeds (Montesano *et al*., 2018). Furthermore, Cucurbitacin B has been reported to inhibit hypoxia-inducing factor 1-α (HIF-1α), mainly associated with the progression of aggressive tumors (Ma *et al*., 2014).

Furthermore, the higher content of linoleic acid in the oil must have contributed to the observed cytotoxic activity (Bocca *et al*., 2010; Zeng *et al*., 2015). The cytotoxicity observed at concentrations higher than 1500 µg.mL-1 for both MCF-7 cell types and human fibroblasts may have been due to the surfactants present in the formulation. This result is expected, since there are reports in the literature about the cytotoxicity of surfactants, such as Tween® 80, used in this study (Arechabala *et al*., 1999).

5. CONCLUSION

The *Cucurbita moschata* pumpkin seed oil nanoemulsion at 4 ºC has an adequate physical-chemical characteristics and has a cytotoxic activity against MCF-7 cells. The findings demonstrate that the pumpkin seed oil nanoemulsion has a promising application as a nutraceutical for breast cancer treatment and it should be considered for further studies to investigate the antitumor mechanism involved and to validate its activity.

6. ACKNOWLEDGEMENTS

This work was supported by the Coordenação de Aperfeiçoamento de Pessoal de Nível Superior - Brazil (CAPES) - Finance Code 001, Conselho Nacional de Desenvolvimento Científico e Tecnológico – Brazil and Fundação de Amparo à Pesquisa

do Estado de Minas Gerais - Brazil (Grants numbers: APQ-00443-18 and RED-00570-16). We would like to thank the Multiuser Laboratory of Bioproducts and Bioprocesses (CentralBio, Faculty of Pharmacy, Federal University of Juiz de Fora/UFJF). We would like to thank Dra. Vany Ferraz, Chromatography Laboratory, Department of Chemistry – Federal University of Minas Gerais/UFMG. The authors also thank Correa J. O. A. and Alves M. S. (UFJF) for the kind access to their lab.

REFERENCES

Arechabala, B., Coiffard, C., Rivalland, P., Coiffard, L. J. M., & De Roeck-Holtzhauer, Y. (1999). Comparison of Cytotoxicity of Various Surfactants Tested on Normal Human Fibroblast Cultures using the Neutral Red Test, MTT Assay and LDH Release. Em JOURNAL OF APPLIED TOXICOLOGY J. Appl. Toxicol (Vol. 19).

Bocca, C., Bozzo, F., Cannito, S., Colombatto, S., & Miglietta, A. (2010). CLA reduces breast cancer cell growth and invasion through ERα and PI3K/Akt pathways. Chemico-Biological Interactions, 183(1), 187–193. https://doi.org/10.1016/j.cbi.2009.09.022

Chauhan, B., Kumar, G., Kalam, N., & Ansari, S. H. (2013). Current concepts and prospects of herbal nutraceutical: A review. Journal of Advanced Pharmaceutical Technology and Research, 4(1), 4–8. https://doi.org/10.4103/2231-4040.107494

Chuan Xia, H., Chuan Zhang, Z., & Chuan ZHANG, Z. (2003). Purification and characterization of Moschatin, a novel type I ribosome-inactivating protein from the mature seeds of pumpkin (Cucurbita moschata), and preparation of its immunotoxin against human melanoma cells. Em Cell Research (Vol. 13, Número 5).

de Carvalho, L. M. J., Gomes, P. B., Godoy, R. L. de O., Pacheco, S., do Monte, P. H. F., de Carvalho, J. L. V., Nutti, M. R., Neves, A. C. L., Vieira, A. C. R. A., & Ramos, S. R. R. (2012). Total carotenoid content, α-carotene and β-carotene, of landrace pumpkins (Cucurbita moschata Duch): A preliminary study. Food Research International, 47(2), 337–340. https://doi.org/10.1016/j.foodres.2011.07.040

Durante, M., Lenucci, M. S., D'Amico, L., Piro, G., & Mita, G. (2014). Effect of drying and co-matrix addition on the yield and quality of supercritical CO2 extracted pumpkin (Cucurbita moschata Duch.) oil. Food Chemistry, 148, 314–320. https://doi.org/10.1016/j.foodchem.2013.10.051

Farokhzad, O. C., & Langer, R. (2009). Impact of Nanotechnology on Drug Delivery. ACS Nano, 3(1), 16–20. https://doi.org/10.1021/nn900002m

Garbayo, E., Pascual-Gil, S., Rodríguez-Nogales, C., Saludas, L., Estella-Hermoso de Mendoza, A., & Blanco-Prieto, M. J. (2020). Nanomedicine and drug delivery systems in cancer and regenerative medicine. Wiley Interdisciplinary Reviews: Nanomedicine and Nanobiotechnology, 12(5), 1–22. https://doi.org/10.1002/wnan.1637

Huang, D., Sun, L., Huang, L., & Chen, Y. (2021). Nanodrug delivery systems modulate tumor vessels to increase the enhanced permeability and retention effect. Journal of Personalized Medicine, 11(2), 1–26. https://doi.org/10.3390/jpm11020124

Kashyap, D., Pal, D., Sharma, R., Garg, V. K., Goel, N., Koundal, D., Zaguia, A., Koundal, S., & Belay, A. (2022). Global Increase in Breast Cancer Incidence: Risk Factors and Preventive Measures. BioMed Research International, 2022. https://doi.org/10.1155/2022/9605439

Lee, K. W., Lee, H. J., Cho, H. Y., & Kim, Y. J. (2005). Role of the conjugated linoleic acid in the prevention of cancer. Em Critical Reviews in Food Science and Nutrition (Vol. 45, Número 2, p. 135–144). https://doi.org/10.1080/10408690490911800

Liechty, W. B., & Peppas, N. A. (2012). Expert opinion: Responsive polymer nanoparticles in cancer therapy. European Journal of Pharmaceutics and Biopharmaceutics, 80(2), 241–246. https://doi.org/10.1016/j.ejpb.2011.08.004

Ma J, Zi Jiang Y, Shi H, Mi C, Li J, Xing Nan, et al. Cucurbitacin B inhibits the translational expression of hypoxia-inducible factor-1α. European Journal of Pharmacology. 2014;723, 46–54.

Maiuolo, J., Gliozzi, M., Carresi, C., Musolino, V., Oppedisano, F., Scarano, F., Nucera, S., Scicchitano, M., Bosco, F., Macri, R., Ruga, S., Cardamone, A., Coppoletta, A., Mollace, A., Cognetti, F., & Mollace, V. (2021). Nutraceuticals and cancer: Potential for natural polyphenols. Nutrients, 13(11), 1–27. https://doi.org/10.3390/nu13113834

Men, X., Choi, S. Il, Han, X., Kwon, H. Y., Jang, G. W., Choi, Y. E., Park, S. M., & Lee, O. H. (2021). Physicochemical, nutritional and functional properties of Cucurbita moschata. Food Science and Biotechnology, 30(2), 171–183. https://doi.org/10.1007/s10068-020-00835-2

Montesano, D., Rocchetti, G., Putnik, P., & Lucini, L. (2018). Bioactive profile of pumpkin: an overview on terpenoids and their health-promoting properties. Current Opinion in Food Science, 22, 81–87. https://doi.org/10.1016/j.cofs.2018.02.003

Murkovic, M., Piironen, V., Lampi, A. M., Kraushofer, T., & Sontag, G. (2004). Changes in chemical composition of pumpkin seeds during the roasting process for production of pumpkin seed oil (Part 1: Non-volatile compounds). Food Chemistry, 84(3), 359–365. https://doi.org/10.1016/S0308-8146(03)00240-1

Musakhanian, J., Rodier, J. D., & Dave, M. (2022). Oxidative Stability in Lipid Formulations: a Review of the Mechanisms, Drivers, and Inhibitors of Oxidation. Em AAPS PharmSciTech (Vol. 23, Número 5). Springer Science and Business Media Deutschland GmbH. https://doi.org/10.1208/s12249-022-02282-0

Nyam, K. L., Tan, C. P., Lai, O. M., Long, K., & Che Man, Y. B. (2009). Physicochemical properties and bioactive compounds of selected seed oils. LWT, 42(8), 1396–1403. https://doi.org/10.1016/j.lwt.2009.03.006

Patel, S. (2013). Pumpkin (Cucurbita sp.) seeds as nutraceutic: a review on status quo and scopes. Mediterranean Journal of Nutrition and Metabolism, 6(3), 183–189. https://doi.org/10.1007/s12349-013-0131-5

Peiretti, P. G., Meineri, G., Gai, F., Longato, E., & Amarowicz, R. (2017). Antioxidative activities and phenolic compounds of pumpkin (Cucurbita pepo) seeds and amaranth (Amaranthus caudatus) grain extracts. Natural Product Research, 31(18), 2178–2182. https://doi.org/10.1080/14786419.2017.1278597

Puscas, Andreea & Andruta, Muresan & Socaci, Sonia & Francisc, Dulf & Muste, Sevastița & Fetea, Florinela & Semeniuc, Cristina & Bunea, Andrea & Muresan, Vlad & Pintea, Adela. (2022). Cold pressed pumpkin seed oil fatty acids, carotenoids, volatile compounds profiles and infrared fingerprints as affected by storage time and wax-based oleogelation. Journal of the Science of Food and Agriculture. 103. 10.1002/jsfa.12180.

Puttasiddaiah, R., Lakshminarayana, R., Somashekar, N. L., Gupta, V. K., Inbaraj, B. S., Usmani, Z., Raghavendra, V. B., Sridhar, K., & Sharma, M. (2022). Advances in Nanofabrication Technology for Nutraceuticals: New Insights and Future Trends. Bioengineering, 9(9), 1–22. https://doi.org/10.3390/bioengineering9090478

Roland, I., Piel, G., Delattre, L., & Evrard, B. (2003). Systematic characterization of oil-in-water emulsions for formulation design. International Journal of Pharmaceutics, 263(1–2), 85–94. https://doi.org/10.1016/S0378-5173(03)00364-8

Rossi, L., Mazzara, C., & Pagani, O. (2018). Diagnosis and Treatment of Breast Cancer in Young Women. Current Treatment Options in Oncology, 20(12). https://doi.org/10.1007/s11864-019-0685-7

Sande, D., Colen, G., dos Santos, G. F., Ferraz, V. P., & Takahashi, J. A. (2018). Production of omega 3, 6, and 9 fatty acids from hydrolysis of vegetable oils and animal fat with Colletotrichum gloeosporioides lipase. Food Science and Biotechnology, 27(2), 537–545. https://doi.org/10.1007/s10068-017-0249-1

Sung, H., Ferlay, J., Siegel, R. L., Laversanne, M., Soerjomataram, I., Jemal, A., & Bray, F. (2021). Global Cancer Statistics 2020: GLOBOCAN Estimates of Incidence and Mortality Worldwide for 36 Cancers in 185 Countries. CA: A Cancer Journal for Clinicians, 71(3), 209–249. https://doi.org/10.3322/caac.21660

Uuh-Narvaez, J. J., Negrete-León, E., Acevedo-Fernández, J. J., & Segura-Campos, M. R. (2021). Antihyperglycemic and hypoglycemic activity of Mayan plant foods in rodent models. Journal of the Science of Food and Agriculture, 101(10), 4193–4200. https://doi.org/10.1002/jsfa.11057

Veronezi, C. M., & Jorge, N. (2012). Bioactive Compounds in Lipid Fractions of Pumpkin (Cucurbita sp) Seeds for Use in Food. Journal of Food Science, 77(6), 653–657. https://doi.org/10.1111/j.1750-3841.2012.02736.x

Vieira, D. B., & Gamarra, L. F. (2016). Advances in the use of nanocarriers for cancer diagnosis and treatment. Einstein (São Paulo), 14(1), 99–103. https://doi.org/10.1590/S1679-45082016RB3475

Waks, A. G., & Winer, E. P. (2019). Breast Cancer Treatment: A Review. JAMA - Journal of the American Medical Association, 321(3), 288–300. https://doi.org/10.1001/jama.2018.19323

Wu, J. (2021). The enhanced permeability and retention (Epr) effect: The significance of the concept and methods to enhance its application. Journal of Personalized Medicine, 11(8). https://doi.org/10.3390/jpm11080771

XIA, H. C., LI, F., LI, Z., & ZHANG, Z. C. (2003). Purification and characterization of Moschatin, a novel type I ribosome-inactivating protein from the mature seeds of pumpkin (Cucurbita moschata), and preparation of its immunotoxin against human melanoma cells. Cell Research, 13(5), 369–374. https://doi.org/10.1038/sj.cr.7290182

Zeng, M., Zheng, M., Lu, D., Wang, J., Jiang, W., & Sha, O. (2015). Anti tumor activities and apoptotic mechanism of ribosome inactivating proteins. Em Chinese Journal of Cancer (Vol. 34, Número 8). Landes Bioscience. https://doi.org/10.1186/s40880-015-0030-x

Zhou, Y., Wang, T., Zhai, S., Li, W., & Meng, Q. (2016). Linoleic acid and breast cancer risk: A meta-analysis. Public Health Nutrition, 19(8), 1457–1463. https://doi.org/10.1017/S136898001500289X

CHAPTER 6

ENHANCED ALGINATE/COLLAGEN SCAFFOLDS WITH CONDUCTIVE POLY (3,4-ETHYLENEDIOXYTHIOPHENE) NANOPARTICLES FOR NEXT-GENERATION SMALL-DIAMETER TISSUE-ENGINEERED BLOOD VESSELS

Data de submissão: 06/11/2025
Data de aceite: 20/11/2025

Emilio Castro[1, 2, 3]
Universitat Internacional de Catalunya
Barcelona, Spain
https://orcid.org/0000-0002-7491-4169

Èlia Bosch-Rué[1, 2]
Universitat Internacional de Catalunya
Barcelona, Spain
https://orcid.org/0000-0002-1131-4908

Sara Estruch-Sotoca[1]
Universitat Internacional de Catalunya
Barcelona, Spain

Román A. Pérez[1, 2]
Universitat Internacional de Catalunya
Barcelona, Spain
https://orcid.org/0000-0002-0823-2303

ABSTRACT: Cardiovascular disease remains the leading cause of death worldwide, highlighting the urgent need for improved vascular grafts. While large-diameter tissue-engineered blood vessels (TEBVs) have shown therapeutic success, developing small-diameter TEBVs (inner diameter ≤ 6 mm) remains challenging. This study reports a novel method for fabricating small-diameter TEBVs using a triple coaxial nozzle to co-extrude alginate, collagen, and a sacrificial polymer, forming scaffolds closely mimicking native vessel microarchitecture. The resulting conduits had an outer diameter of approximately 1.6 mm and wall thickness of about 265 µm. A key innovation involved coating the scaffold's surface with conductive poly (3,4-ethylenedioxythiophene) (PEDOT) nanoparticles using in situ interfacial polymerization. Optimal PEDOT-to-APS ratios (4:2 and 8:2) were identified, which increased scaffold swelling capability, slowed degradation, and significantly improved mechanical strength (burst pressure increased from 1.13 to 3.38 bar) and electrical conductivity (up to 122 µS/cm). Enhanced surface roughness and hydrophilicity resulting from the PEDOT layer promoted the adhesion and proliferation of human aortic smooth muscle cells (hASMCs). Notably, lyophilization was found unnecessary, as direct extrusion yielded reproducible, favorable conduit properties. The conductive, biocompatible nature of these hybrid hydrogel scaffolds suggests great potential for use in vascular regeneration and potentially for vascularizing artificial organs, providing a promising route toward functional small-diameter vascular replacements.

[1] Bioengineering Institute of Technology, Universitat Internacional de Catalunya, Sant Cugat del Vallès, 08195 Barcelona, Spain.

[2] Basic Sciences Department, Universitat Internacional de Catalunya (UIC), Sant Cugat del Vallès, 08195 Barcelona, Spain.

[3] Institut de Neurociències, Universitat Autònoma de Barcelona, 08193, Bellaterra (Cerdanyola del Vallès), Spain.

KEYWORDS: blood vessel; PEDOT nanoparticles; conductive hydrogel; vascular regeneration; smooth muscle cells.

ESTRUTURAS DE ALGINATO/COLAGÉNIO MELHORADAS COM NANOPARTÍCULAS CONDUTORAS DE POLI (3,4-ETILENODIOXITIOFENO) PARA VASOS SANGUÍNEOS DE PEQUENO DIÂMETRO DE PRÓXIMA GERAÇÃO, CONCEBIDOS ATRAVÉS DE ENGENHARIA DE TECIDOS

RESUMO: As doenças cardiovasculares continuam a ser a principal causa de morte em todo o mundo, destacando a necessidade urgente de melhorar os enxertos vasculares. Embora os vasos sanguíneos de grande diâmetro criados por engenharia de tecidos (TEBVs) tenham demonstrado sucesso terapêutico, o desenvolvimento de TEBVs de pequeno diâmetro (diâmetro interno ≤ 6 mm) continua a ser um desafio. Este estudo relata um método inovador para fabricar TEBVs de pequeno diâmetro usando um bico coaxial triplo para coextrudar alginato, colagénio e um polímero sacrificial, formando arcabouços que imitam de perto a microarquitetura dos vasos nativos. Os condutos resultantes tinham um diâmetro externo de aproximadamente 1,6 mm e espessura de parede de cerca de 265 µm. Uma inovação importante envolveu o revestimento da superfície da estrutura com nanopartículas condutoras de poli(3,4-etilenodioxietileno) (PEDOT) usando polimerização interfacial in situ. Foram identificadas as proporções ideais de PEDOT para APS (4:2 e 8:2), que aumentaram a capacidade de expansão da estrutura, retardaram a degradação e melhoraram significativamente a resistência mecânica (a pressão de ruptura aumentou de 1,13 para 3,38 bar) e a condutividade elétrica (até 122 µS/cm). A rugosidade superficial e a hidrofilicidade aprimoradas resultantes da camada de PEDOT promoveram a adesão e a proliferação de células musculares lisas da aorta humana (hASMCs). Notavelmente, a liofilização foi considerada desnecessária, pois a extrusão direta produziu propriedades de conduto reproduzíveis e favoráveis. A natureza condutiva e biocompatível dessas estruturas híbridas de hidrogel sugere um grande potencial para uso na regeneração vascular.
PALAVRAS-CHAVE: vaso sanguíneo; nanopartículas PEDOT; hidrogel condutivo; regeneração vascular; células musculares lisas.

1. THE CRITICAL NEED FOR FUNCTIONAL SMALL-DIAMETER VASCULAR GRAFTS

Cardiovascular disease (CVD) remains the preeminent global health challenge, accounting for the largest share of morbidity and mortality worldwide (Kim et al., 2025). A cornerstone of surgical intervention for advanced CVD, particularly in cases of severe atherosclerosis or trauma, involves the bypass or replacement of occluded or damaged blood vessels. While autologous vascular grafts (vessels harvested from the patient) are the gold standard due to their superior biocompatibility and patency rates, their use is often limited by donor site morbidity, insufficient vessel quality, or the sheer lack of available suitable vessels. This pressing clinical need has driven extensive research into the development of artificial vascular grafts (Lang et al., 2024).

Figure 1. Different techniques for developing small diameter TEBVs.

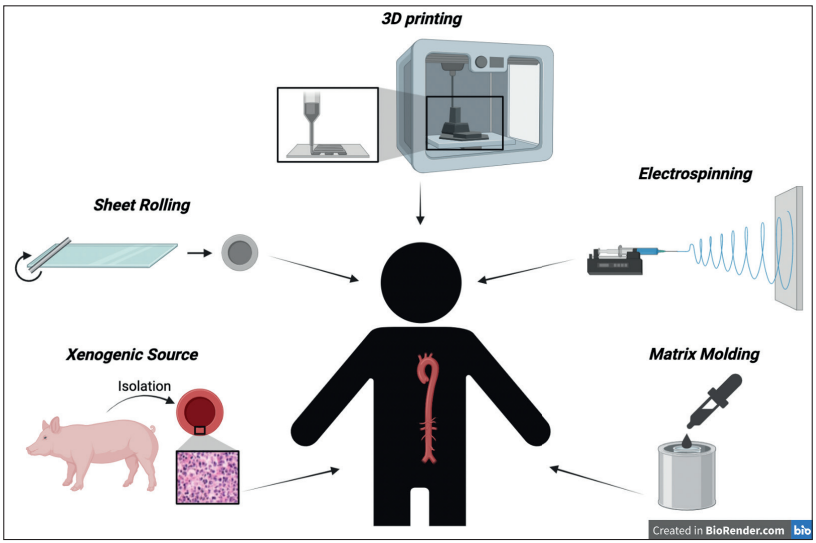

The field of tissue engineering has delivered notable successes, particularly in the creation of large-diameter tissue-engineered blood vessels (TEBVs diameter > 6 mm), which have shown promising clinical outcomes. However, the engineering of functional small-diameter TEBVs (diameter ≈ 6 mm) continues to represent a significant, unmet challenge (È. Bosch-Rué et al., 2023; E. Bosch-Rué et al., 2025). These small-diameter grafts are highly prone to failure due to two primary mechanisms: thrombosis (clotting) and intimal hyperplasia (excessive smooth muscle cell proliferation and extracellular matrix deposition leading to luminal narrowing). A fundamental difficulty lies in recreating the intricate biophysical and biochemical microenvironment of native small arteries, which includes appropriate mechanical strength, compliance, and, crucially, bioelectrical signaling capabilities (Zhang et al., 2021). This current research addresses this critical gap by developing a sophisticated hybrid scaffold that integrates natural polymers with a conductive element to enhance cellular response and mechanical durability.

2. FABRICATION AND CONDUCTIVE POLYMER INCORPORATION VIA INTERFACIAL POLYMERIZATION

2.1. SCAFFOLD FABRICATION AND PREPARATION

The foundation of the TEBV mimicry involved the use of a porous, biocompatible hydrogel composed of alginate (Alg) and collagen (Col) (T. Hu & Lo, 2021; X. Hu et al., 2024). These TEBV-like acellular tubular structures were first fabricated using established extrusion techniques, as previously detailed in the literature (E. Bosch-Rué et al., 2020).

Alginate provides structural integrity and is cost-effective, while collagen offers crucial cell-binding sites, mimicking the natural extracellular matrix (ECM).To obtain the nanoparticles exclusively in the outer layer (alginate), the scaffolds (1.5 cm long) were placed on a metal mandrel in which each edge was sutured with non-absorbable silk sutures (Silkam®), preventing the entry of the reagents to the inner layer.

Figure 2. Schematic representation of TEBV-like structures through extrusion method.

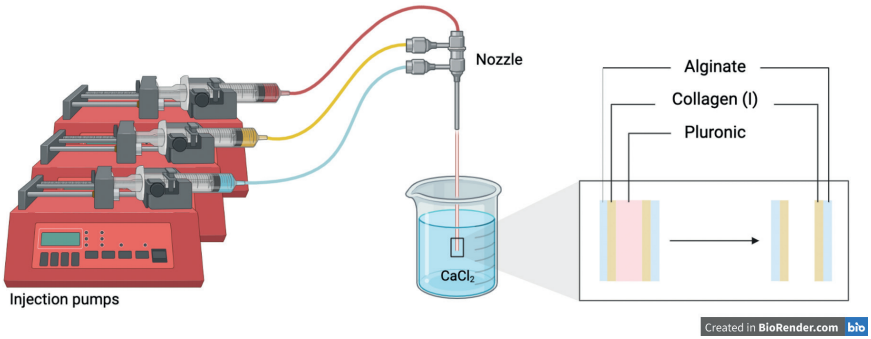

2.2. IN SITU INTERFACIAL POLYMERIZATION OF PEDOT NANOPARTICLES

To impart necessary conductivity, the scaffolds were functionalized with poly(3,4-ethylenedioxythiophene) (PEDOT). The interfacial polymerization method via *in situ* synthesis was specifically selected for the incorporation of the 3,4-ethylenedioxythiophene (EDOT) monomer (purity 99.9%) (Wang, Guan, et al., 2017; Wang, Sun, et al., 2017; Xu et al., 2018). This technique leverages the phase boundary between two immiscible liquids – an aqueous phase containing the oxidant and an organic phase (hexane) containing the monomer. The static polymerization of the EDOT monomer at this interface promotes the directed formation of PEDOT nanoparticles onto the scaffold structure.

Figure 3. Preparation of the conductive PEDOT/Alg/Col hydrogels.

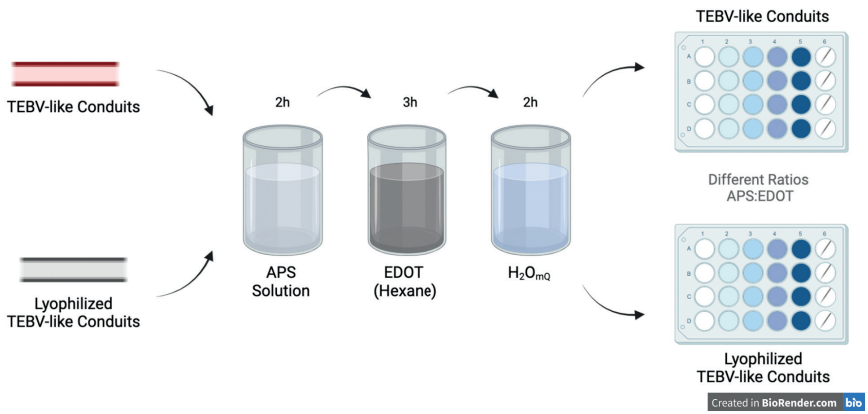

Crucially, to mimic the native vessel architecture and ensure unidirectional cell stimulation, the functionalization was strategically confined to the outer layer (alginate-rich side) of the scaffold. Scaffolds (approximately 1.5 cm in length) were carefully mounted onto a non-reactive metal mandrel. Each edge was securely closed using non-absorbable silk sutures (e.g., Silkam®), effectively sealing the inner lumen and preventing the ingress of polymerization reagents to the inner layer.

2.3. OPTIMIZATION OF CONDUCTIVE NANOPARTICLE ASSEMBLY

Two distinct physical treatments of the Alg/Col scaffolds were assessed prior to conductive modification:

1. Directly extruded hydrogels (Hydrated condition).
2. Samples subjected to a freeze-drying process (Freezing at -20°C for 12 hours, followed by lyophilization for 24 hours).

For the *in-situ* polymerization, the Alg/Col structures were first immersed for 2 hours in a 2 mL aqueous solution containing ammonium persulfate (APS) as the oxidant. The swollen samples were subsequently transferred and incubated for 3 hours in a 2 mL hexane solution containing the EDOT monomer (0.4 mol/L). The progress of the PEDOT formation was macroscopically observed by the scaffolds' gradual transition from a colorless or white state to a distinctive dark navy blue/black coloration, indicative of the successful production of PEDOT nanoparticles *in situ*. Systematic optimization was performed by preparing samples across five different molar concentration ratios of APS to EDOT (0, 0.5, 1, 2, and 4) to determine the optimal synthesis conditions. Finally, the ducts were thoroughly purified by immersion in deionized water for 2 hours and careful washing to eliminate any unreacted reagents or byproducts.

3. PHYSICOCHEMICAL AND BIOLOGICAL CHARACTERIZATION

3.1. MORPHOLOGICAL AND DISTRIBUTION ANALYSIS

The successful polymerization of PEDOT was immediately confirmed by the distinct color shift of the pure white Alg/Col structures to black following the nanoparticle assembly. Scanning Electron Microscopy (SEM) images revealed that the PEDOT nanoparticles, with an average diameter of approximately 50 nm, were successfully grown and localized on the surface of the outermost layer of the samples. Furthermore, the number and surface coverage of these nanoparticles were observed to increase proportionally with higher monomer and oxidant concentrations. Notably, samples where the ends were left

unsutured exhibited PEDOT presence within the inner layer, which critically coincided with a detrimental loss of the characteristic porous structure in that region.

Figure 4. Morphology of the TEBV-like structures was characterized by scanning electron microscope (SEM) (JSM-5410, JEOL).

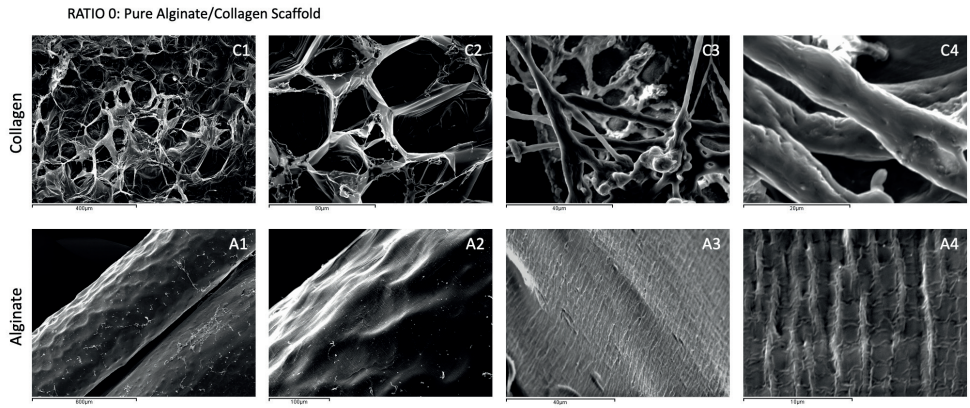

Comparative analysis of the two scaffold pre-treatments (hydrated vs. freeze-dried) showed significant differences in nanoparticle assembly. The data indicated that the freeze-drying process (Group L) prior to PEDOT incorporation resulted in a non-uniform nanoparticle assembly compared to the directly extruded hydrogels. This finding suggests that the structural changes induced by lyophilization (e.g., pore collapse or altered surface chemistry) are detrimental to the final homogeneous distribution of the conductive coating, potentially leading to suboptimal electrical stimulation of cells *in vivo*.

3.2. PHYSICOCHEMICAL AND MECHANICAL PROPERTY ENHANCEMENT

Analysis of the mechanical and swelling properties identified that the molar concentration ratios of APS to EDOT of 4:2 and 8:2 provided the most favorable outcome. These ratios not only demonstrated an increase in the swelling rates of the pure Alg/Col scaffolds but also significantly contributed to decreasing their degradation rate and substantially increasing their overall mechanical properties.

Figure 5. EDS spectra analysis of TEBV surface PEDOT.

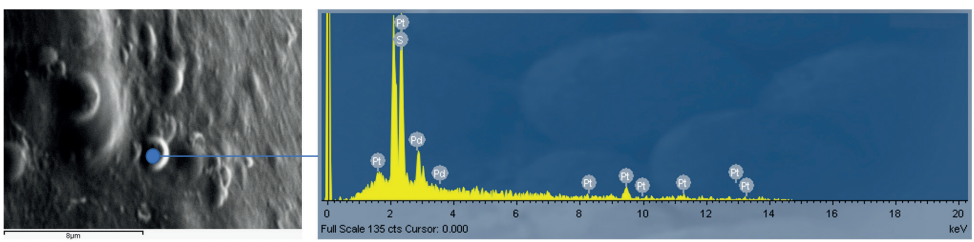

The burst pressure test, a key metric for assessing vascular graft strength, showed that the maximum pressure at rupture increased directly with the amount of incorporated PEDOT. This data strongly supports the conclusion that the nanoparticle integration significantly reinforces the duct wall integrity. The presence of PEDOT was further corroborated via Energy Dispersive X-ray Spectroscopy (EDS) spectra analyses, which successfully identified the characteristic sulfur (S) atoms within the PEDOT chemical structure coupled with SEM imaging.

Figure 6. Burst pressure of TEBVs with different APS:EDOT ratios.

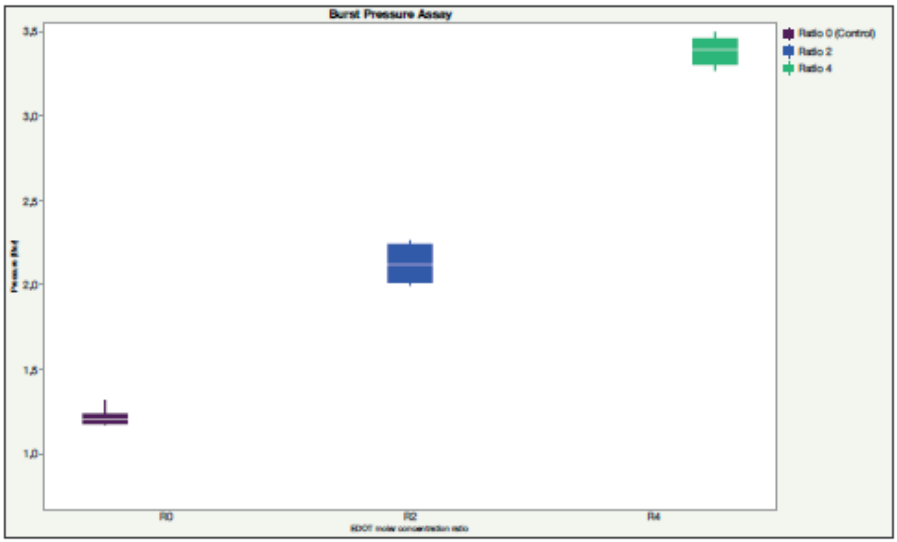

3.3. HYDROPHILICITY AND ELECTRICAL CONDUCTIVITY

The incorporation of the conductive nanoparticles dramatically improved the hydrophilicity of the scaffolds compared to the pure hydrogels. This was quantitatively demonstrated by a decrease in the contact angle value corresponding to a higher molar concentration ratio of APS to EDOT. Enhanced hydrophilicity is crucial for promoting protein adsorption and subsequent cell adhesion.

Figure 7. Images of PEDOT nanoparticles assembly on the surface of TEBVs with different APS:EDOT ratios.

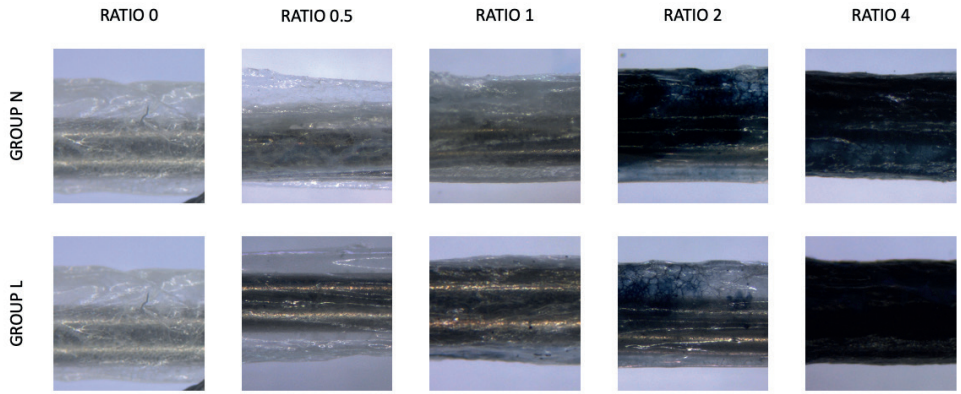

The electrical conductivity of the hydrated scaffolds was a primary focus, measured at various time points (30 minutes, 1 hour, and 24 hours after immersion in high-purity water). The results clearly indicated that higher nanoparticle density translated to greater electrical conductivity. Critically, all four scaffolds with the highest PEDOT loading achieved an electrical conductivity value greater than 1.0 times 10^{-3} mS/cm. This threshold is generally considered sufficient to allow the scaffold to function as an effective electrode for electrical stimulation of vascular cells, a vital function for tissue maturation.

Figure 8. SEM images showing PEDOT nanoparticles on the surface of TEBVs with different APS:EDOT ratios.

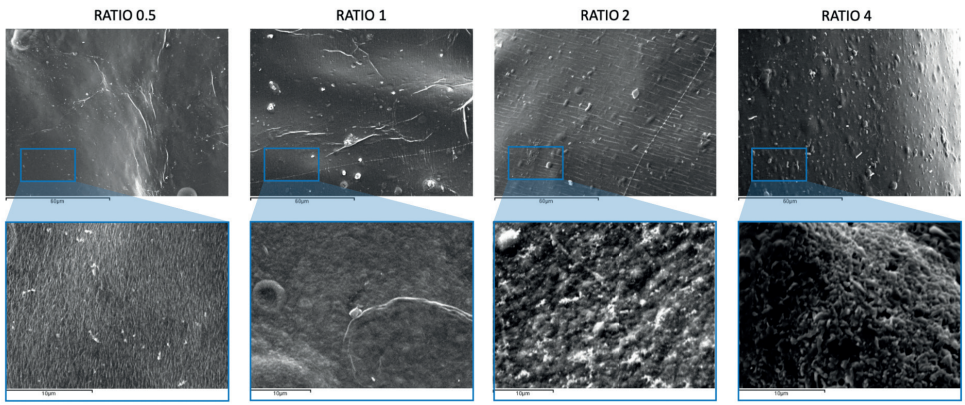

Figure 9. Hydrophilicity of TEBVs with different APS:EDOT ratio.

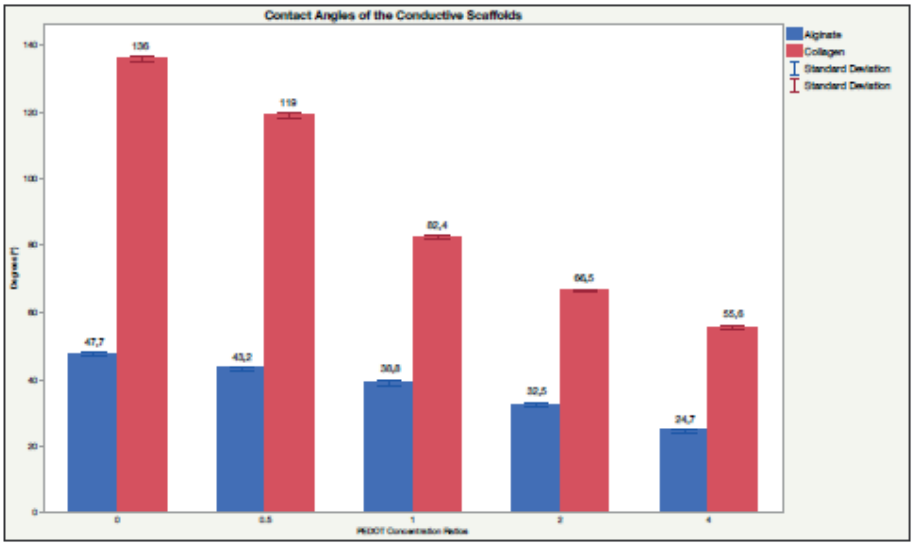

Figure 10. Conductivity of hydrated acellular scaffolds was analyzed using a multiparametric meter (Mettller Toledo TM, S213).

APS:EDOT molar Concentration	Conductivity 30mins (µS/cm)	Conductivity 1h (µS/cm)	Conductivity 24h (µS/cm)
Ratio 0:0	1.19 ± 0.06	1,18 ± 0.08	**1.21 ± 0.13**
Ratio 1:2	17.77 ± 0.84	20.47 ± 1.15	**26.91 ± 1.25**
Ratio 2:2	32.39 ± 1.06	33.15 ± 1.36	**39.04 ± 1.51**
Ratio 4:2	40.82 ± 1.12	53.70 ± 1.37	**63.95 ± 1.77**
Ratio 8:2	72.65 ± 1.06	109.85 ± 1.73	**122.18 ± 1.32**

3.4. CELLULAR VIABILITY AND ADHESION

To assess the biological performance, human aortic smooth muscle cells (hASMCs) were seeded and cultured on the outer, sterilized layer of the PEDOT-assembled Alg/Col scaffolds. Smooth muscle cells (SMCs) are essential for regulating vascular tone and compliance (de Laorden et al., 2025). The introduction of the PEDOT nanoparticles is hypothesized to provide a platform for external electrical stimuli capable of inducing SMC contractility and promoting production of their own native ECM, ultimately improving the functional compliance and strength of the engineered vessel (Molina et al., 2024).

Figure 11. Adhesion of hASMCs were evaluated by staining actin filaments (F-actin) using phalloidin on day 3 after seeding. Confocal laser microscopy (Leica SP8, LAS X software version 3.5.5.19976) was utilized at emission wavelengths of 480 nm-520 nm for phalloidin and 405 nm-460 nm for DAPI.

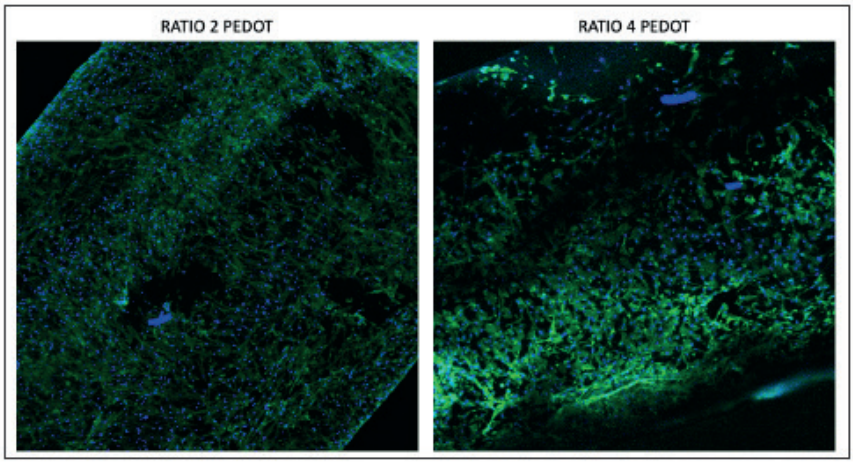

Microscopic evaluation showed excellent cell survival: hASMCs successfully adhered and proliferated, covering almost the entire surface of the vessels containing Alg/Col and various concentrations of PEDOT. This result confirms that the conductive polymer forms a highly biofunctionalized layer that is non-cytotoxic and conducive to cell survival. Furthermore, the scaffold containing the intermediate ratio 2 of PEDOT appeared to enhance superior cell proliferation and attachment compared to the highest molar concentration ratio immediately after seeding, suggesting that there is an optimal concentration for cell compatibility and growth.

4. CONCLUSIONS AND FUTURE OUTLOOK

In conclusion, this study successfully demonstrates the development of hybrid, conductive, porous conduits via the uniform assembly of PEDOT nanoparticles on the surface of Alg/Col scaffolds using a targeted *in situ* interfacial polymerization method. The optimal performance was achieved with the APS to EDOT molar concentration ratios of 4:2 and 8:2. The resulting hydrophilic hydrogel exhibited significantly improved mechanical properties and electrical conductivity suitable for cellular stimulation. Subsequently, *in vitro* testing confirmed that the materials are highly biocompatible, supporting excellent hASMC adhesion and proliferation.

The synergistic combination of the natural, cell-friendly polymers (alginate and collagen) with the electroconductive and mechanically reinforcing properties of PEDOT nanoparticles yields a potentially exceptional scaffold for vascular regeneration (Babeli et

al., 2020). These compelling results strongly suggest that this advanced bioengineering approach is highly suitable for delivering effective electrical stimulation to smooth muscle cells within small-diameter TEBVs. The ability to successfully bioengineer this type of functional artificial artery would constitute a breakthrough, not only serving as a critically needed small-diameter vascular substitute for bypass grafts but also offering a robust, vascularizing platform for the emerging field of artificial organ engineering.

5. ACKNOWLEDGMENTS

This work was supported by a Government of Catalonia grant (No. 2017 SGR 708), the Ramón y Cajal fellowship (No. RYC2018-025977-I) and Project No. RTI2018–096088-J-100 from the Spanish Ministry of Science and Innovation/FEDER-EU.

REFERENCES

Babeli, I., Ruano, G., Casanovas, J., Ginebra, M. P., García-Torres, J., & Alemán, C. (2020). Conductive, self-healable and reusable poly(3,4-ethylenedioxythiophene)-based hydrogels for highly sensitive pressure arrays. *Journal of Materials Chemistry C*, *8*(25), 8654–8667. https://doi.org/10.1039/D0TC01947J

Bosch-Rué, E., Delgado, L. M., Gil, F. J., & Perez, R. A. (2020). Direct extrusion of individually encapsulated endothelial and smooth muscle cells mimicking blood vessel structures and vascular native cell alignment. *Biofabrication*, *13*(1). https://doi.org/10.1088/1758-5090/abbd27

Bosch-Rué, È., Díez-Tercero, L., Buitrago, J. O., Castro, E., & Pérez, R. A. (2023). Angiogenic and immunomodulation role of ions for initial stages of bone tissue regeneration. *Acta Biomaterialia*, *166*, 14–41. https://doi.org/10.1016/J.ACTBIO.2023.06.001

Bosch-Rué, E., Zhang, Q., Truskey, G. A., Olmos Buitrago, J., M Bosch, B., & Pérez, R. A. (2025). Development of small tissue engineered blood vessels and their clinical and research applications. In *Biofabrication* (Vol. 17, Issue 3). Institute of Physics. https://doi.org/10.1088/1758-5090/add626

de Laorden, E. H., Rodilla, B. L., Arroyo-Hernández, M., & Iglesias, M. (2025). Advances in human amniotic placenta membrane-derived mesenchymal stromal cells (hAMSCs) for regenerative medicine: enhancing therapeutic potential with biomaterials and scaffolds. *Frontiers in Bioengineering and Biotechnology*, *13*. https://doi.org/10.3389/fbioe.2025.1590393

Hu, T., & Lo, A. C. Y. (2021). Collagen–alginate composite hydrogel: Application in tissue engineering and biomedical sciences. *Polymers*, *13*(11). https://doi.org/10.3390/polym13111852

Hu, X., Wu, Z., Zhang, Z., Yao, H., & Wang, D. A. (2024). Type II collagen scaffolds for tissue engineering. In *Communications Materials* (Vol. 5, Issue 1). Springer Nature. https://doi.org/10.1038/s43246-024-00598-x

Kim, M. S., Choi, Y., & Lee, K. Y. (2025). Three-Dimensional Printing and Bioprinting Strategies for Cardiovascular Constructs: From Printing Inks to Vascularization. In *Polymers* (Vol. 17, Issue 17). Multidisciplinary Digital Publishing Institute (MDPI). https://doi.org/10.3390/polym17172337

Lang, Z., Chen, T., Zhu, S., Wu, X., Wu, Y., Miao, X., Wang, Q., Zhao, L., Zhu, Z., & Xu, R. X. (2024). Construction of vascular grafts based on tissue-engineered scaffolds. In *Materials Today Bio* (Vol. 29). Elsevier B.V. https://doi.org/10.1016/j.mtbio.2024.101336

Molina, B. G., Fuentes, J., Alemán, C., & Sánchez, S. (2024). Merging BioActuation and BioCapacitive properties: A 3D bioprinted devices to self-stimulate using self-stored energy. *Biosensors and Bioelectronics*, *251*. https://doi.org/10.1016/j.bios.2024.116117

Wang, S., Guan, S., Zhu, Z., Li, W., Liu, T., & Ma, X. (2017). Hyaluronic acid doped-poly(3,4-ethylenedioxythiophene)/chitosan/gelatin (PEDOT-HA/Cs/Gel) porous conductive scaffold for nerve regeneration. *Materials Science and Engineering C*, *71*, 308–316. https://doi.org/10.1016/j.msec.2016.10.029

Wang, S., Sun, C., Guan, S., Li, W., Xu, J., Ge, D., Zhuang, M., Liu, T., & Ma, X. (2017). Chitosan/gelatin porous scaffolds assembled with conductive poly(3,4-ethylenedioxythiophene) nanoparticles for neural tissue engineering. *Journal of Materials Chemistry B*, *5*(24), 4774–4788. https://doi.org/10.1039/c7tb00608j

Xu, C., Guan, S., Wang, S., Gong, W., Liu, T., Ma, X., & Sun, C. (2018). Biodegradable and electroconductive poly(3,4-ethylenedioxythiophene)/carboxymethyl chitosan hydrogels for neural tissue engineering. *Materials Science and Engineering C*, *84*, 32–43. https://doi.org/10.1016/j.msec.2017.11.032

Zhang, Q., Bosch-Rué, È., Pérez, R. A., & Truskey, G. A. (2021). Biofabrication of tissue engineering vascular systems. In *APL Bioengineering* (Vol. 5, Issue 2). American Institute of Physics Inc. https://doi.org/10.1063/5.0039628

CHAPTER 7

ELABORATION OF AN ANTISEPTIC GEL BASED ON BIOACTIVE COMPOUNDS OF *ORIGANUM VULGARE* AND *ALOE VERA* ENCAPSULATED IN SiO_2 Y ZnO-SnO_2 NANOPARTICLES FOR CONTROLLED RELEASE

Data de submissão: 12/11/2025
Data de aceite: 28/11/2025

Juan Manuel Padilla Flores[1]
1Universidad Tecnológica del
Centro de Veracruz
1Av. Universidad No.350
Carretera Federal Cuitláhuac-La Tinaja
Congregación dos Caminos
94910 Cuitláhuac
Veracruz – Llave, México
http://orcid.org/0000-0002-9038-2959

Guadalupe Luna Cedillo
Universidad Tecnológica del
Centro de Veracruz
1Av. Universidad No.350
Carretera Federal Cuitláhuac-La Tinaja
Congregación dos Caminos
94910 Cuitláhuac
Veracruz – Llave, México
http://orcid.org/0000-0003-4876-0773

Francisco Javier Tzompantzi Morales
Universidad Autónoma
Metropolitana – Iztapalapa
Departamento de Química
San Rafael Atlixco No. 186
México 09340, D.F., México
http://orcid.org/0000-0002-3056-9500

Sandra Luz Hernández-Valladolid
1Universidad Tecnológica del
Centro de Veracruz
1Av. Universidad No.350
Carretera Federal Cuitláhuac-La Tinaja
Congregación dos Caminos
94910 Cuitláhuac
Veracruz – Llave, México
http://orcid.org/0000-0001-6962-6413

ABSTRACT: The purpose of this project was to develop an antiseptic gel based on bioactive compounds of *Origanum vulgare* and *Aloe vera* incorporated with SiO_2 and ZnO - SnO_2 nanoparticles, to obtain a broad spectrum of bactericidal and virucidal action. Currently, in Mexico, the sanitary crisis caused by SARS-CoV-2 has had a significant impact on Mexican families, since hygiene and disinfection are the main concern of Mexicans. This problem has led the population to purchase antiseptic gels with a narrower spectrum of action, in order to reduce the cost of disinfection products. ZnO nanoparticles present antimicrobial properties, which together with SnO_2 nanoparticles, which have photocatalytic properties, generate a synergy. Likewise, the liberating properties of the SiO_2 nanoparticles show a better antimicrobial activity as a function of the antiseptic gel based on bioactive compounds of *Origanum vulgare* and *Aloe vera*.

KEYWORDS: antiseptics; nanoparticles; bactericidal; virucidal and bioactive compounds.

[1] Autor para correspondencia.

1. INTRODUCTION

Nanotechnology is the study and development of systems at the nanometer scale (1 nm is equivalent to 10^{-9}m), in which totally new properties and phenomena are observed, which are governed by the laws of quantum mechanics, these new properties are those that scientists take advantage of to create new materials (nanomaterials) or nanotechnological devices. Ortiz Aguilar (2019) explains that nanomaterials can occur naturally, however, there are also manufactured nanomaterials, which are intentionally designed with specific properties (mechanical, electrical, optical and catalytic) and these nanomaterials can be presented in the form of nano-objects, materials that are characterized by having one, two or three external dimensions at the nanoscale.

SiO_2, SnO_2 and ZnO nanoparticles are nano-structured materials that have been studied for their properties, which include antibacterial action. For the fabrication of these nanomaterials, different synthesis methods have been used, either chemical or physical, which provide good properties.

In Mexico, the health crisis caused by SARS-CoV-2 had a significant impact on Mexican families, as the unemployment rate in Mexico increased, indicating a slow recovery of the country's economy. The Mexican population is applying sanitary measures to avoid contagion in their homes, with an estimated increase in the use of antiseptic gels in homes. However, due to the sanitary crisis, the prices of sanitizers, such as antiseptic gels, have risen, since hygiene and disinfection is the main concern of Mexicans. This problem leads the population to purchase antiseptic gels with a lower spectrum of action, in order to reduce the cost of disinfection products. On the other hand, there is a problem related to the epidemiology of wounds in Mexico. The health sector (2018) mentions the epidemiological characteristics and costs to wound care in medical units, as well as for the affected population in this area, since the prices of antiseptics present high costs for the treatment of acute and chronic wounds. It is estimated that 26.6% of the Mexican population presents traumatic injuries, and 23.4% corresponds to diabetic foot ulcers.

2. OBJECTIVE

To elaborate an antiseptic gel based on bioactive compounds of *Origanum vulgare* and *Aloe vera*, incorporated with SiO_2 and ZnO-SnO_2 nanoparticles, which allows having a broad bactericidal and virucidal spectrum to be used as a sanitary measure and improve the antimicrobial action against microorganisms present in wounds.

3. EXPERIMENTAL PART

3.1. OBTAINING THE AQUEOUS EXTRACT OF *ORIGANUM VULGARE*

Origanum vulgare leaves were collected on the federal highway in Fortín, Ver. The leaves were selected complete and free of pests. They were then washed with abundant tap water and the leaves were dried by dehydration for 6 h at 40°C in a smoking oven. Once dried, they were ground in a grinder. The crushed material was subjected to continuous extraction with 95% ethanol using the Soxhlet method. Finally, a simple distillation was performed to obtain the pure extract.

3.2. OBTAINING THE EXTRACT OF *ALOE VERA*

Aloe vera leaves were collected and selected homogeneously and representatively in shape, size and color, discarding those that showed damage or other alterations. The *Aloe vera* leaves were washed in a bath with water and sodium hypochlorite to eliminate microorganisms. Once the leaves were washed and dried, they were cut longitudinally on a tray, then with a spoon, the mucilage was gently scraped until it was completely separated from the cortical parenchyma, then the gel was stored in airtight containers.

3.3. PREPARATION OF NANOPARTICLES

SiO_2 nanopartciles

400 mL of distilled water and the surfactant were placed in an agitation of 700 rpm for 5 min. Subsequently, 16 mL of NH_4OH were added by drip, leaving the solution to agitate for 10 min. The temperature was raised to 95°C, leaving it to react by a constant agitation at 700 rpm. To maintain the temperature, a sand bath system was mounted. The product was then allowed to cool to room temperature. It was centrifuged at 15,000 rpm for 15 minutes with three washes of an ethanol-water solution (1:1). Once obtained, 15 mL of *Origanum vulgare* extract was added, allowing the mixture to rest. Subsequently, the mixture was placed in a water bath at 40°C until a pasty consistency was obtained. It was calcined at 400°C for 1h. At the end of the process of obtaining nanoparticles, a light green dry material was obtained.

SnO_2 nanoparticles

Two g of tin chloride ($SnCl_2 \cdot 2H_2O$), used as tin precursor, was added to 42 mL of *Origanum vulgare* extract and left in agitation until its complete dissolution; obtaining a mixture. Subsequently, the sample was placed in a water bath at 60°C until a pasty

consistency was obtained. It was then calcined at 400°C for 60 min. At the end of the process, a dry light gray material was obtained.

ZnO nanoparticles

2 g of zinc nitrate was dissolved in 50 mL of distilled water in a beaker with constant stirring for 10 min, using a magnetic stirrer. After stirring, 5 mL of *Origanum vulgare* extract was added. The mixture was heated from 60°C to 90°C. The color of the resulting solution changed from a transparent white to a light green paste confirming the formation of ZnO NPs. The obtained paste was transferred to a ceramic crucible and kept in a muffle furnace heated at 400°C for 2h. The resulting powder was used for characterization and preparation of the antiseptic gel.

3.4. CHARACTERIZATION OF NANOPARTICLES

UV-Vis Spectroscopy Analysis

UV-Visible spectrophotometer was used to confirm the formation of SiO_2, SnO_2 and ZnO nanoparticles. The UV-Vis spectra of the samples were performed in Perkin Elmer spectrophotometer, in the range of 200 to 800 nm.

3.5. PREPARATION OF ANTISEPTIC GEL BASE

2 g of carbopol were dissolved in 120 mL of alcohol in a beaker with a stirring of less than 150 rpm. Subsequently, 2 mL of glycerin was added, maintaining a constant agitation. When the mixture was homogenized, 1 mL of trihydroxyethylamine was added. Finally, when the gel obtained consistency, it was bottled.

3.6. PREPARATION OF AN ANTISEPTIC GEL BASED ON NATURAL EXTRACTS AND NANOPARTICLES

2 g of carbopol were dissolved in 120 mL of alcohol in a beaker with a stirring of less than 150 rpm. Subsequently, 2 mL of glycerin was added, maintaining a constant agitation. When the mixture was homogenized, 1 mL of trihydroxyethylamine and 5 mL of *Aloe vera* extract were added. After the gel obtained consistency, it was packaged. To impregnate the SiO_2 and ZnO - SnO_2 nanoparticles, a sonicator was used with a duration of 30 min. Finally, the gel samples were left to rest.

3.7. PREPARATION OF CULTURE MEDIA

In the preparation of the culture media using nutrient agar, 23 g of the medium was rehydrated in 1L of distilled water. It was then allowed to stand for 10 to 15 min. Once

rested, it was heated at constant stirring to boiling point for 1 min to dissolve it completely. It was then autoclaved at 121°C for 15 min.

In casein peptone culture media, 20 g of the medium was rehydrated in 1 L of distilled water. It was then allowed to stand for 15 to 20 min. Once resting, it was heated by stirring constantly to boiling point for 2 min to dissolve completely. It was then sterilized in autoclave at 121°C for 17 min.

Once sterilization was complete, the media were poured into each of the corresponding petri dishes, where they were allowed to cool to room temperature. Finally, the media were labeled for use in other tests.

3.8. DETERMINATION OF ANTIMICROBIAL ACTIVITY

To analyze the antimicrobial activity of the antiseptic gel based on extracts with the incorporation of SiO_2 and SnO_2 - ZnO nanoparticles, disc diffusion methods were performed, where gram-positive and gram-negative bacterial species were used. The sterile discs loaded with different concentrations of nanoparticles solution (1 mg/ mL) were aseptically maintained in petri dish media, previously cleaned with a broth solution of test bacteria.

In addition, the base antiseptic gel was used as a positive control, while samples of the natural extract-based antiseptic gel with the incorporation of nanoparticles were used as negative controls. The antimicrobial activity was scored in the clear zones surrounding the corresponding discs.

4. RESULTS AND DISCUSSION

4.1. UV-VIS SPECTROSCOPY ANALYSIS

SiO_2 nanoparticles

The SiO_2 nanoparticles were analyzed using UV-Vis spectroscopy in the range between 300 to 800 nm. In Figure 1, the peak absorbance of these nanoparticles is observed at 350 nm, due to their surface plasmon resonance.

Figure 1. UV-Vis spectroscopy of the SiO_2.

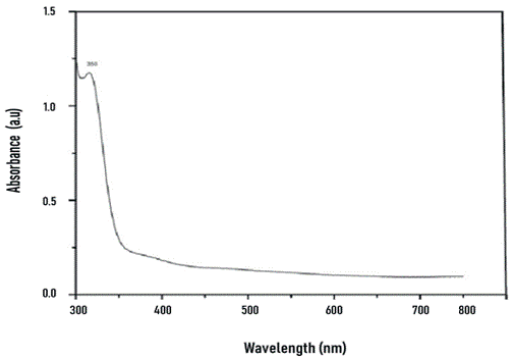

SnO_2 nanoparticles

UV-Vis spectroscopy analysis was performed at room temperature. The absorption spectrum of SnO_2 nanoparticles was recorded in a wavelength range between 200 to 800 nm. In Figure 2, the absorbance peak of SnO_2 nanoparticles at 260 nm is observed. The energy value of the forbidden band is 2.84 eV.

ZnO nanoparticles

The confirmation of Origanum vulgare extract of ZnO nanoparticles was observed by the color change from white to light green. In Figure 3, the UV spectrum of the synthesized ZnO nanoparticles is shown. The absorbance peak is at 354 nm, due to the surface plasmon resonance of these nanoparticles.

Figure 2. UV-Vis spectroscopy of the SnO_2.

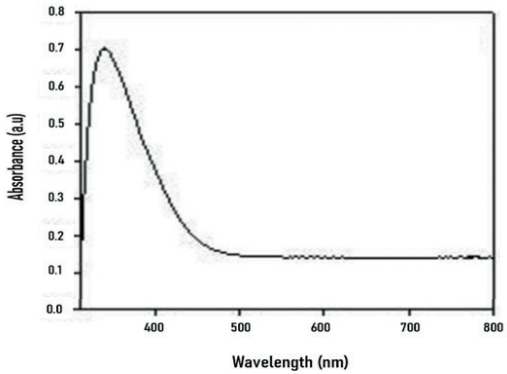

Figure 3. UV-Vis spectroscopy of the ZnO.

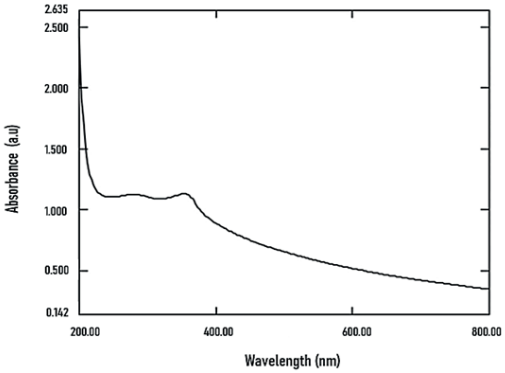

4.2. DETERMINATION OF ANTIMICROBIAL ACTIVITY OF ANTISEPTIC GEL

The nanoparticles used for the preparation of the antiseptic gel are used in various applications due to their antimicrobial properties. In the present study, agar disc diffusion test was used to measure the efficiency of the antiseptic gel based on natural extracts with the incorporation of SiO_2 and ZnO - SnO_2 nanoparticles against gram negative and gram positive bacteria. The inhibition zone was analyzed by the disk diffusion method for 4 h with the corresponding nanoparticles, using different concentrations for the preparation of the antiseptic gel.

Figure 4 shows the antimicrobial activity of the antiseptic gel samples, in the case of Figure 4(a) it can be determined that the base gel presents a superficial antimicrobial activity against the positive bacteria, this is attributed to the large surface area to volume ratio of the nanoparticles used, providing a better inhibitory contact with the microorganisms. The antimicrobial properties of the nanoparticles interact with the microorganisms by adhering to the surface of the bacterial cell membranes, penetrating and affecting the permeability of the bacterial membranes.

Figure 4. Antimicrobial activity (a) base gel and (b) antiseptic gel with ZnO-SnO_2 nanoparticles.

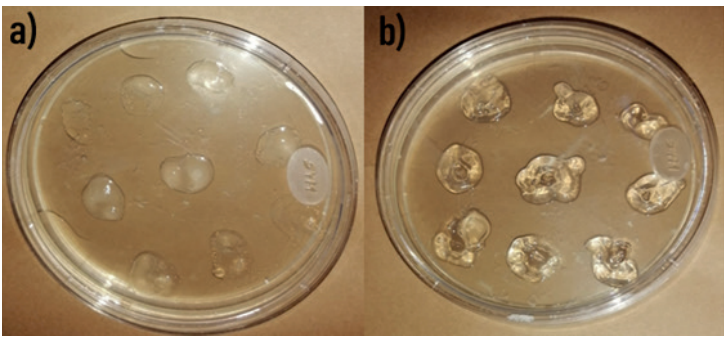

Tables 1 and 2 show the size of the disinfected diameter using the antiseptic gel based on natural extracts with the incorporation of SiO_2 and ZnO - SnO_2 nanoparticles.

Table 1. Recording of the diameter of the disinfected área of the ZnO-SnO_2 nanoparticles

Registro de área desinfectada (mm)				
	1 h	***2 h***	***3 h***	***4 h***
Blanco	5 mm	6 mm	7 mm	8 mm
0.25 g / L	5 mm	7 mm	9 mm	11 mm
0.5 g / L	9 mm	10 mm	15 mm	17 mm
1 g / L	10 mm	11 mm	14 mm	17 mm

Table 1 shows the records regarding the diameter of the disinfection area using ZnO-SnO_2 nanoparticles in the antiseptic gel samples. The record of the disinfection area was recorded in millimeters. As can be seen in the table, the antiseptic gel without the bioactive components of *Origanum vulgare* and *Aloe vera* extracts with the incorporation of nanoparticles at different concentrations, presented a lower area than the samples of the antiseptic gel incorporated by natural extracts already mentioned and ZnO-SnO_2 nanoparticles.

The study to evaluate the effectiveness of the antiseptic gel had a duration of 4 h, where the samples showed an effectiveness in reducing microorganisms present in the medio de cultivo of gram-negative and gram-positive.

The sample with a concentration of 0.5 g/L showed a higher effectiveness in the antimicrobial activity on gram-negative and gram-positive bacteria. However, the samples with a concentration of 1 g/L of ZnO-SnO_2 nanoparticles also presented a greater effectiveness, however, there was not a great difference with respect to the samples with a concentration of 0.5 g/L, which is why it was analyzed that this concentration allows a prolonged release of the bioactive compounds of the *Origanum vulgare* and *Aloe vera* extracts.

Table 2. Recording of the diameter of the disinfected of the SiO_2 nanoparticles.

Registro de área desinfectada (mm)				
	1 h	***2 h***	***3 h***	***4 h***
Blanco	5 mm	6 mm	7 mm	8 mm
0.25 g / L	5 mm	6 mm	8 mm	9 mm
0.5 g / L	5 mm	7 mm	8 mm	10 mm
1 g / L	6 mm	8 mm	9 mm	11 mm

Table 2 shows the record corresponding to the antimicrobial evaluation of the antiseptic gel based on the bioactive components of *Origanum vulgare* and *Aloe vera* extract with different concentrations of SiO_2 nanoparticles with respect to the antiseptic gel without components, which was considered as a blank.

The sample that presented the best effectiveness for the reduction of microorganisms was the one with the concentration of 1 g/L of SiO_2 nanoparticles with the bioactive compounds of the *Origanum vulgare* and *Aloe vera* extracts. However, this sample did not present the same effectiveness with both gram-negative and gram-positive microorganisms.

5. CONCLUSIONS

UV-Vis spectroscopy confirmed the formation of SiO_2, ZnO and SnO_2 nanoparticles.

The study of the antimicrobial activity showed that the antiseptic gel based on *Origanum vulgare* and *Aloe vera* extract with the incorporation of 0.5 g/L of ZnO - SnO_2 nanoparticles developed a synergy, increasing the efficiency of the antimicrobial activity due to its photocatalytic properties, allowing the reduction of gram-negative and gram-positive bacteria.

The release character of SiO_2 can be observed through the increase of the inhibition area with respect to the release of Origanum vulgare and *Aloe vera* extracts over time.

Therefore, it is concluded that the antiseptic properties of alcohol, as well as those of *Origanum vulgare* and *Aloe vera* extracts, the SiO_2 releasing character, and the photoactive properties of ZnO-SnO_2, present a synergy resulting in a better antimicrobial activity.

6. ACKNOWLEDGMENTS

Agradecemos a la Universidad Tecnológica del Centro de Veracruz, por todo el apoyo brindado y por permitirnos el uso de su infraestructura para desarrollar este proyecto. Asimismo, le agradecemos al Dr. Vicente Rodríguez González del Instituto Potosino de Investigación Científica y Tecnológica A.C. (IPICYT), como también al Dr. Francisco Javier Tzompantzin Morales del departamento de Química de la Universidad Autónoma Metropolitana (UAM).

BIBLIOGRAPHIC REFERENCES

Ortiz Aguilar, J. E. (2019). *Actividad antimicrobiana de nanopartículas cerámicas sintetizadas por un método verde para uso en aplicaciones biomédicas*. [Tesis de grado, Universidad Autónoma de Occidente]. https://red.uao.edu.co/bitstream/handle/10614/11795/T08856.pdf?sequence=6&isAllow

Morales, R., Pascual, H. y Tandío, J. (2004). *Jardín Botánico de Madrid*. Ibersaf.

Arcila, C., Loarca, G., Lecona, S. y González, E. (2004). Oregano: Properties, composition and biological activity. *Scielo, 54*(1), 100 – 111. http://ve.scielo.org/scielo.php?script=sci_arttext&pid=S

López, D. (2019). Identification of possible toxicological risks and their sanitary regulations of the use of nanomaterials in products for human consumption in Mexico. *Revista Médica, 10*(3), 221 – 228. https://www.medigraphic.com/pdfs/revmed/md-2019/md193e.pdf

Rodrigues, M., Kosaric, N., Bonham, C. y Gurtner, G. (2019). Wound healing: A cellular perspective. Physiological reviews, 99(1), 665-706. https://doi.org/10.1152/physrev.00067.2017

Wang, P., Huang, B., Horng, H., Yeh, C. y Chen, Y. (2018). Wound healing. *Journal of the Chinese Medical Association: JCMA, 81*(2), 94-101. https://doi.org/10.1016/j.jcma.2017.11.002

CHAPTER 8

ARSENIC REMOVAL FROM GROUNDWATER USING RECYCLED IRON NANOPARTICLES: DEVELOPMENT AND EVALUATION OF A LOW-COST FILTER FOR RURAL COMMUNITIES

Data de submissão: 08/11/2025
Data de aceite: 24/11/2025

Juan Simón Torres Espada
Faculty of Engineering FICAM
Universidad Mayor, Real y Pontificia de San Francisco Xavier de Chuquisaca
Bolivia
https://orcid.org/0000-0003-4176-3672

Yrene Romina Lazcano Cruz
Tesista - Título de Ingeniero Químico
Universidad Mayor, Real y Pontificia de San Francisco Xavier de Chuquisaca
Bolivia

ABSTRACT: The presence of geogenic arsenic in groundwater poses a serious threat to public health in regions such as the Lake Poopó basin in Oruro, Bolivia. This study developed and evaluated a low-cost experimental filter using metallic iron (Fe^0) and iron oxide (Fe_3O_4) nanoparticles obtained from recycled iron shavings using top-down and bottom-up filtration technologies. The nanoparticles were integrated into a homemade filtration system along with readily available materials such as sand, charcoal, and ground brick. Kinetic and adsorption tests were performed under controlled conditions, achieving arsenic removal rates exceeding 97% with Fe^0 nanoparticles and 91% with Fe_3O_4. These results best fit the Freundlich isotherm model and second-order kinetics, which describe the arsenate adsorption behavior on both nanoparticles. The filter proved effective for up to 13 consecutive treatment cycles, reducing arsenic concentrations to levels ≤ 0.01 mg/L. This approach represents a sustainable, economical, and technically viable alternative for rural communities affected by this contaminant.
KEYWORDS: arsenic; iron nanoparticles; iron oxide; groundwater; low-cost filter; adsorption.

1. INTRODUCTION

Arsenic is an inorganic contaminant naturally present in aquifers of volcanic origin, especially in Andean regions. In Bolivia, its presence in groundwater has been little studied, despite representing a significant health risk. The World Health Organization (WHO) establishes a maximum limit of 10 µg/L for arsenic in drinking water. However, concentrations of up to 112 µg/L have been detected in the community of San Agustín de Puñaca. In groundwater bodies, arsenic is found as hydrogen arsenate and arsenic acid, which, under oxidizing or reducing conditions,

can release As $^{+5}$ or As $^{+3}$ ions, respectively. The availability and transport of these compounds in the environment are mainly determined by the pH of the groundwater and by interaction with soil minerals through adsorption and desorption processes. In this context, an experimental filter based on recycled nanomaterials was developed as an accessible and effective solution for arsenic removal. The behavior of Fe^0 and Fe_3O_4 nanoparticles was evaluated using kinetic models and adsorption and equilibrium isotherms for arsenic removal in groundwater samples, allowing the determination $_{of}$ whether the mechanism corresponded to physisorption or chemisorption.

2. MATERIALS AND METHODS

Water samples were collected at five sampling points. Analyses included pH, conductivity, turbidity, and anions. (Bicarbonates, phosphate, nitrates, sulfates), cations (silicon, iron), and total arsenic. To determine the initial arsenic concentration, Atomic Absorption Spectrophotometry (AA500) was used. Samples were microfiltered through a 0.45 µm membrane (Hawach Scientific) using a vacuum pump and then acidified with 2–3 drops of 1% (w/v) HNO_3 (trace metal grade). All samples were stored at low temperature (4°C). Arsenic concentrations were measured using an Atomic Absorption Spectrophotometer to assess the filter's adsorption efficiency.

Metallic iron (Fe^0) and iron oxide (Fe_3O_4) nanoparticles were synthesized from iron shavings using top-down and bottom-up physical and chemical methods. (Torres Espada, 2020) The resulting particles ranged in size from 20–200 nm. The filter consisted of a 5 × 20.6.cm PVC column with 12 layers of filter materials: Fe^0 and Fe_3O_4 nanoparticles, sand, charcoal, and ground brick. (TorresEscalera, 2024) The downward flow was gravity-fed at 0.16 L/h. Batch tests were performed with different concentrations of nanoparticles (10–100 mg), contact times (10–240 min), pH of the natural water solution and 250 RPM. To determine the percentage of arsenic removal. To study the adsorption kinetics of arsenate on metallic iron and iron oxide particles, jar tests were performed at 250 RPM for predetermined intervals (10, 20, 30, 60, 120 and 240 min) during stirring, using 10 and 100 mg of nanoparticles at a pH of 7.86. The best-fitting isothermal and kinetic models were determined according to the coefficient of determination (R^2 value).

Finally, for the isotherm study, experiments were conducted with an initial arsenate concentration of 112 µg/L, using a dosage of 10–100 mg for both nanoparticles at 250 RPM for different times (10, 20, 30, and 60 min). An aliquot was taken from each batch and filtered for arsenic concentration analysis of the filtrate. Several fitting

models (Langmuir, Freundlich, and Dubinin) were tested to find the best fit between the experimental data and the theoretical behavior.

3. RESULTS

Table 1 shows the results of the physical and chemical parameters of the well located in the community of San Agustín de Puñaca, northeast of Lake Poopó, in the department of Oruro. The water quality meets the Bolivian standard NB 512 for drinking water, except for the arsenic content. The arsenic content is 112 µg-As/L, significantly higher than the limit established by the Bolivian standard NB 512 of 10 µg-As/L. The contents of competitive anions – sulfates, nitrates, chlorides, and phosphates – are relatively low, with the exception of silicates.

Table 1. Physical-chemical characterization of the San Agustin de Puñaca community.

Parameters	Units	Analytical Method	Results	Permissible limit NB 512
pH		SM 4500-H / 1992 Potentiometric	7.86	6.5-9.0
Temperature	°C	SM 2550/1992	18.8	-
Electrical Conductivity	µS/cm	SM 2510 / 1992 Conductimetric	970	1500
Potential Oxidation-Reduction	mV	Potentiometric	98	-
Turbidity	NTU	2130-B-SM Turbidimeter	3.19	5
Alkalinity	mg/L	ASTM D 1057-02	150	370
Bicarbonates	mg/L	ASTM D 3875-03	94	370
Chlorides	mg/L	SM 3030-F / 1992	0.45	250
Sulfates	mg/L	ASTM D 516-02	103.1	400
Nitrates	mg/L	DIN 38405 T10 mod.	7.05	45
Phosphates	mg/L	Photometric	0.20	-
Silicates	mg/L	ASTM D 859-05	22.77	-
Iron	mg/L	ASTM D 1068-05A	<0.018	0.3
Arsenic	mg/L	SM 3030-F / 1992 EAA	0.12	0.01

Arsenic speciation in groundwater was determined by analyzing the redox potential (Eh) versus pH diagram, which established that under oxidative conditions it has an Eh of 98 mV and a natural pH of 7.86 (Figure 1). Arsenate As^{+5} is the dominant species, having an anionic product of $HAsO42^{-}$, which favors its removal through adsorption

processes, since it is negatively charged. Neutral H_3AsO_3 at natural pH values (between 6 and 9) is not easily removed. Since arsenic is present as $HAsO_4^{2-}$, it is not necessary to increase the oxidation-reduction potential, Eh, of the contaminated well by aeration, or by the use of chemical reagents to modify the pH, since if the pH is decreased, arsenite As^{+3} will be present as the dominant species, being more toxic, which explains a lower efficiency in arsenic removal systems.

Figure 1. Speciation of arsenic in groundwater.

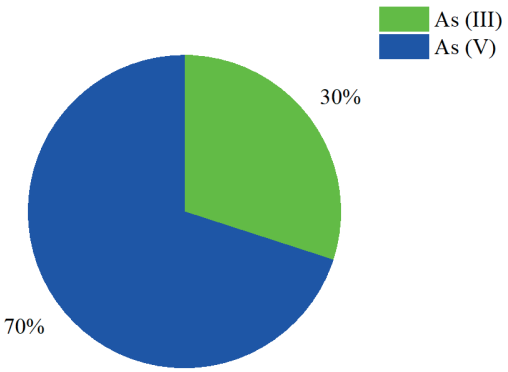

The filter reduced arsenic to 0.007 mg/L in 13 filtration cycles of 10 L, complying with Bolivian standard NB512 and WHO guidelines. Figure 2 shows the physicochemical characterization of the groundwater sample from the community of San Agustin de Puñaca after filtration, reducing turbidity by 67.08%, Aa by 10%, chlorides by 31.11%, sulfates by 41%, nitrates by 12%, phosphates by 40%, and silicates by 34.46%.

Figure 2. Removal of physicochemical parameters.

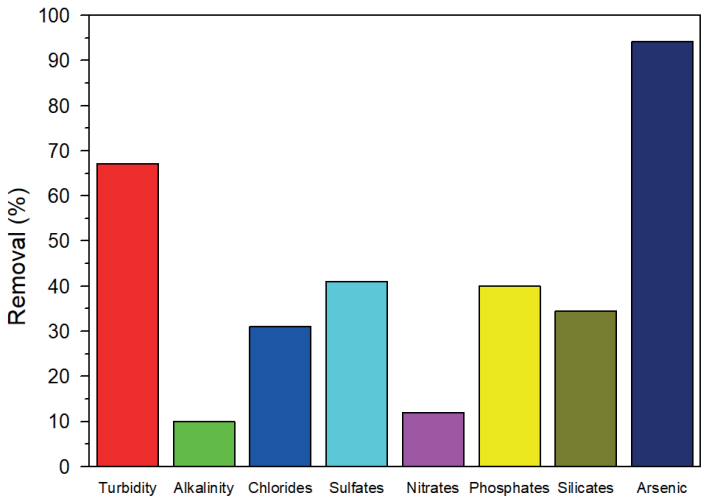

The arsenic removal process under these conditions was optimal, achieving a removal rate of 97.5% for (Fe^{0}) zero valent nanoparticles and 91.7% for Fe_3O_4 iron oxide nanoparticles. The sample was collected directly from its natural environment and contains not only arsenic but also other minerals, organic compounds, and other physicochemical properties, including nitrates, silicates, phosphates, sulfates, etc. All these factors, among others, interfere with the adsorption process, making it less efficient.

Figure 3. Effect of contact time on arsenic removal efficiency with different doses 10-100 mg a) iron nanoparticles Fe ^{0} b) iron oxide nanoparticles Fe $_{3}$ O $_{4}$.

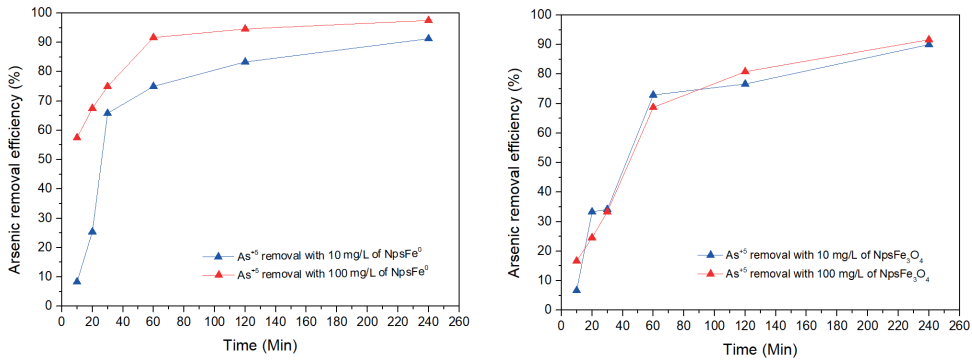

Because the adsorption process was too rapid, exceeding 57.5% efficiency in the first 10 minutes, an equation was developed to describe the adsorption process in such a way that the data could be iterated and the removal efficiency obtained every 2 min, 3 min, 4 min, 5 min, 6 min, etc. It can be seen in Figure 4, that just one minute of contact of the iron nanoparticles with the contaminant, an efficiency of 52% is achieved, thus confirming that the use of metallic iron nanoparticles is effective in the removal of arsenic thanks to their surface area ranging from 60-200 nm, high capacity and high reactivity characteristics of the magnetic material used.

Figure 4. Exponential fit describing the concentration of arsenic in zero valent nanoparticles (Fe ^{0}).

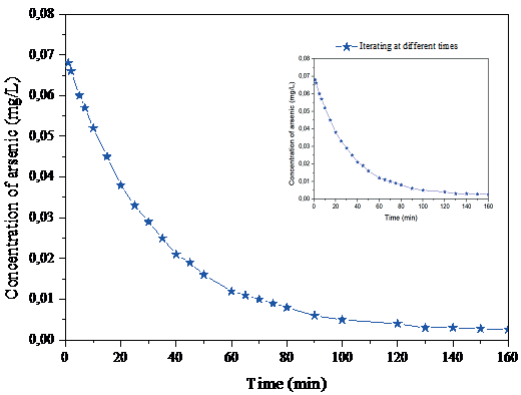

To understand the adsorption mechanism and efficiency of both nanoparticles, the experimental data were analyzed using first-order and second-order kinetic models. The correlation coefficient (R^2) was used to evaluate the best kinetic model (Table 2). Of all the models, the second-order model showed a good correlation coefficient and best fit the experimental data (Figure 5).

Table 2. Kinetic parameters for arsenic removal using metallic iron nanoparticles and iron oxide.

Kinetic Model	Constant	Worth
First Order with NpsFe ^{0}	K	-0.0169
	R^2	0.8971
Second Order with NpsFe ^{0}	K	2,2288
	R^2	0.9607
First Order with $NpsFe_3O_4$	K	-0.0115
	R^2	0.9526
Second Order with $NpsFe_3O_4$	K	0.4127
	R^2	0.9841

Figure 5. Second-order kinetic model for arsenic removal (a) metallic iron nanoparticles (b) iron oxide nanoparticles.

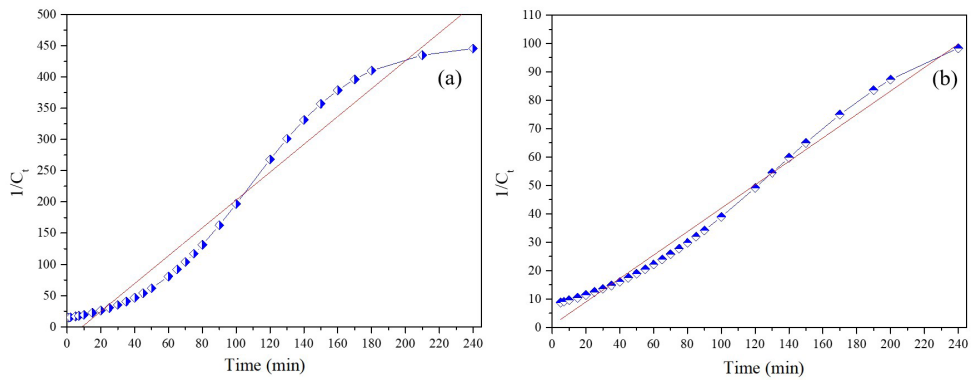

The half-life with respect to contact time, as shown in (Figure 6), shows that after 180 minutes the nanoparticles no longer adsorb more arsenic, so they begin to saturate and the half-life tends to be constant.

Figure 6. Half-life vs. contact time with NpsFe ^{0}.

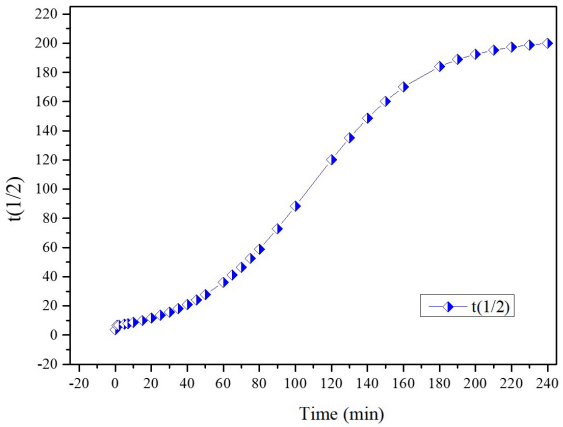

Adsorption isotherm models are fundamental to describing the equilibrium between the adsorbate and the adsorbent. To evaluate the adsorption behavior of the nanoparticles, some well-known isotherms such as the Langmuir, Freundlich, and Dubinin-Radushkevich constants were considered. The fitting results are shown in Figure 7. Table 3 shows the linear regression results according to the Langmuir model. The dimensionless factor R_{$_{L}$} is less than one; therefore, applying the Langmuir isotherm is unfavorable. The calculated Langmuir constant Kf $_{,}$ which can be interpreted as the enthalpy of adsorption, showed negative values. This suggested the exothermic nature of the process and indicated that the surface of the metallic iron and iron oxide nanoparticles was energetically favorable for reacting with the ions.

Table 3. Langmuir model results for arsenic adsorption on nanoparticles.

LANGMUIR MODEL				
PARAMETER	Quantity of NpsFe ^{0} 0.01 g	Quantity of NpsFe ^{0} 0.1 g	Quantity of NpsFe $_{3}$O $_{4}$ 0.01 g	Quantity of NpsFe $_{3}$O $_{4}$ 0.1 g
Adsorption capacity of a monolayer Q $_{or}$ (mg/g)	1,0683	0.7088	1,0243	0.1789
Langmuir constant K $_{f}$ (L/mg)	-33.5520	-26.7710	-30.9536	-32.8267
Adsorption capacity q $_{e}$ (mg/g)	9,0000	1,1000	8,7500	0.8250
Regression coefficient R^{2}	0.5863	0.7537	0.3499	0.6984
R $_{L}$	-0.3305	-0.4520	-0.3684	-0.3402

Table 4 shows the results of the Freundlich model; a higher Kf value indicates a greater adsorption capacity of the adsorbent. Furthermore, a Kf value greater than one indicates the spontaneous nature of the process (Mandal et al., 2014) lanthanum diethanolamine hybrid material is synthesized by co-precipitation method and used for the removal of Cr(VI. However, for all adsorption isotherms for different quantities of nanoparticles, the regression coefficient R^2 was more reliable for the Freundlich model, fitting the experimental data better than for the Langmuir model.

The value of n is related to the distribution of ions bound to the active sites on the surface of the nano-adsorbent. The negative values of n for the different quantities of nanoparticles indicate that the ions of the species present are unfavorable, making it impossible to determine whether the process is by physisorption or chemisorption.

Table 4. Freundlich model results for arsenic adsorption on nanoparticles.

FREUNDLICH MODEL				
PARAMETER	Quantity of $NpsFe^0$ 0.01 g	Quantity of $NpsFe^0$ 0.1 g	Quantity of $NpsFe_3O_4$ 0.01 g	Quantity of $NpsFe_3O_4$ 0.1 g
Freundlich constant K_f (L/mg)	0.0492	0.3372	0.0440	0.0126
Adsorption capacity of a monolayer Q_e (mg/g)	0.2145	0.6237	0.2576	0.1498
Adsorption capacity q_e (mg/g)	9,0000	1,1000	8,7500	0.8250
Regression coefficient R^2	0.8777	0.9189	0.7253	0.9184
n	-0.6496	-3.8149	-0.6199	-0.7762

Table 5 shows the results obtained after applying the Dubinin model. The regression coefficient was almost the same as those calculated by the Freundlich model.

Table 5. Results of the Dubinin model for the adsorption of arsenic on nanoparticles.

DUBININ-RADUSHKEVICH MODEL				
PARAMETER	Quantity of $NpsFe^0$ 0.01 g	Quantity of $NpsFe^0$ 0.1 g	Quantity of $NpsFe_3O_4$ 0.01 g	Quantity of $NpsFe_3O_4$ 0.1 g
Dubinin constant K_f (L/mg)	$4.47x10^{-8}$	$6.00x10^{-9}$	$4.57x10^{-8}$	$3.18x10^{-8}$
Adsorption capacity of a monolayer Q_e (mg/g)	0.3559	0.5463	0.3745	0.06547
Adsorption capacity q_e (mg/g)	9,0000	1,1000	8,7500	0.8250
Regression coefficient R^2	0.8492	0.8877	0.6712	0.8998

Figure 7. Equilibrium adsorption isotherm for arsenic on metallic iron nanoparticles and iron oxide. (a) Langmuir isotherm with 100 mg of NpsFe ^{0}. (b) Langmuir isotherm with 100 mg of NpsFe $_{3}O_{4}$. (c) (d) Freundlich isotherm with 100 mg of NpsFe ^{0}. (e) Freundlich isotherm with 100 mg of NpsFe $_{3}O_{4}$. (f) Dubinin model with 10 mg of NpsFe ^{0}. (f) Dubinin model with 100 mg of NpsFe $_{3}O_{4}$.

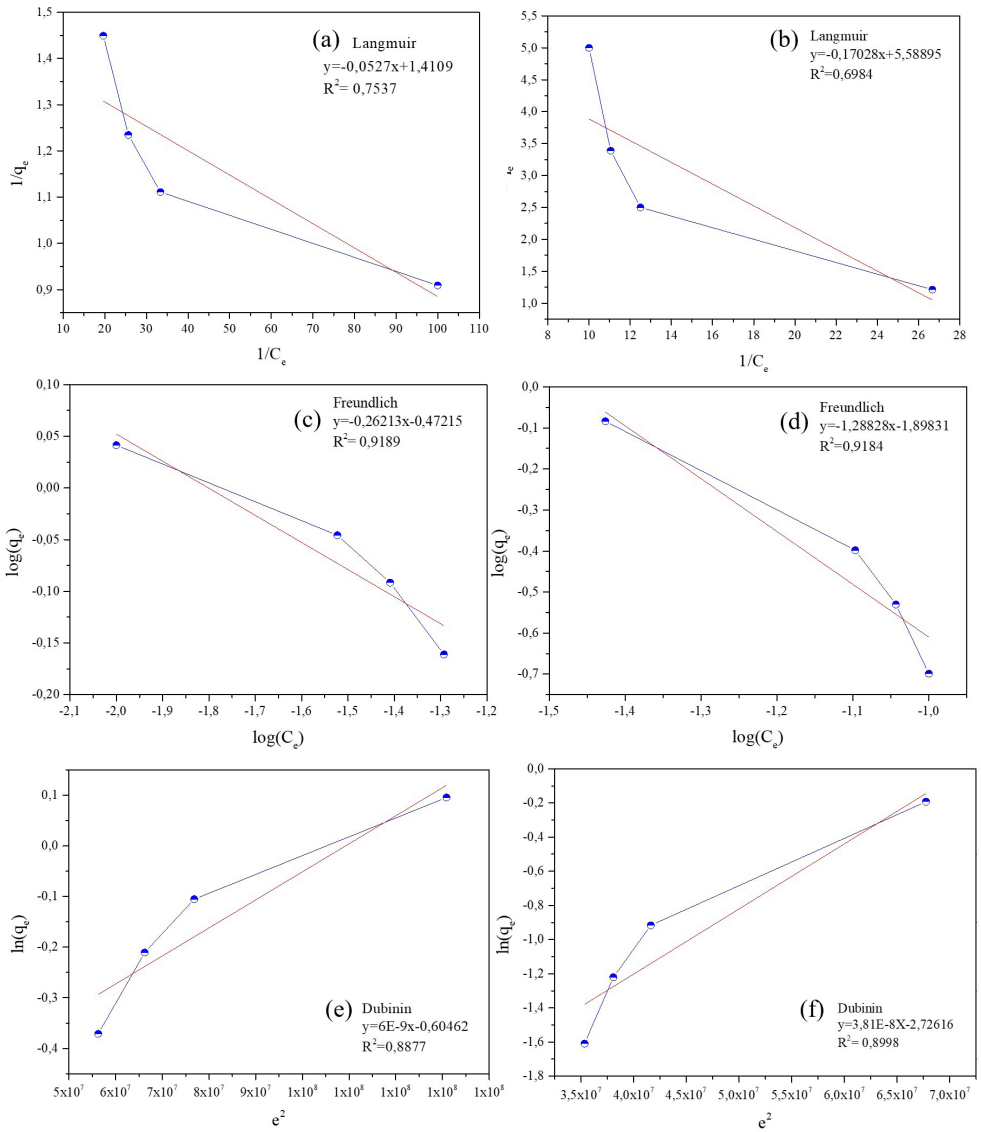

Thermodynamic parameters, such as Gibbs free energy (ΔG), can help determine the likelihood, spontaneity, or exothermic or endothermic states of a reaction – critical aspects of an adsorption process. The energy required to transfer one mole of metallic iron nanoparticles to iron oxide was greater than 40 kJ/mol for arsenic. These results confirmed that the interactions between the adsorbate and the adsorbent were chemical, i.e., a chemisorption process.

4. DISCUSSION

The use of recycled nanoparticles represents a technological innovation with a positive environmental and social impact. Despite the small quantities used, the system achieved results comparable to more expensive commercial technologies. Its combination with locally sourced materials facilitates community implementation. The filter also demonstrated the removal of other contaminants (phosphates, silicates, nitrates), increasing its versatility.

5. CONCLUSIONS

- The presence of geogenic arsenic in the community's groundwater was confirmed, in concentrations dangerous to human health.
- The experimental filter developed effectively removed arsenic to levels below that established by the Bolivian standard NB 512 of 10 µg-As/L, making it an accessible solution for rural areas.
- The adsorption fit the Freundlich model and showed second-order kinetics, indicating a chemisorption process and occurring spontaneously.
- The system is replicable, economical and sustainable, with potential for application in other regions with similar problems.

REFERENCES

1. Carvajal GE. Determination of arsenic in groundwater of the Titicaca sub-basin. 2015.

2. Ravenscroft P, Brammer H, Richards K. Arsenic Pollution: A Global Synthesis. 2009. 3. Muñoz MR. Hydrogeochemistry of naturally occurring arsenic in the Bolivian Altiplano. 2015.

4. Bundschuh J, et al. Distribution of arsenic in Latin America. 2006.

5. (Torres Espada, 2020) Simon, Obtaining iron oxide nanoparticles from chip with bottom-up technology, Revista Ciencia, 18(2021):11-24.

6. T.E.J. Simon, Obtaining iron nanoparticles from chip through top down technology, Int J Green Nanotechnol Mater Sci Eng, 2021.

5. Morgada ME, et al. Arsenic removal with nanoparticulate zerovalent iron. Chemosphere. 2009;143(3):261-8.

6. Ccamerccoa MH, Falcon NLT. J Environ Health Sci Eng. 2022;20(2):849-860. 7. Mandal, S., Mahapatra, S.S., & Patel, R.K. (2015). Neuro fuzzy approach for arsenic(III) and chromium(VI) removal from water. Journal of Water Process Engineering, 5, 58-75.

7. TorresEscalera. (2024). Iron Nanoparticle Filter for Remediation of Groundwater Contaminated by arsenic. *Journal of Drug and Alcohol Research Ashdin Publishing*, 7.

ABOUT THE ORGANIZER

Emilio Castro Otero é professor da área de Bioengenharia na *Universitat Internacional de Catalunya*, Barcelona, Espanha. Pesquisador com ampla trajetória científica nas áreas de biomateriais, nanotecnologia, química física de polímeros e sistemas nanoestruturados aplicados à medicina regenerativa e à liberação controlada de fármacos. Sua produção abrange estudos fundamentais sobre auto-organização molecular, interações entre copolímeros e surfactantes, estabilidade proteica e desenvolvimento de nanopartículas e hidrogéis inteligentes, contribuindo de maneira significativa para a compreensão dos mecanismos físico-químicos que governam materiais avançados e sua aplicabilidade biomédica. Seu trabalho mais recente, publicado em Acta Biomaterialia (2023), aborda o papel angiogênico e imunomodulador de íons nas fases iniciais da regeneração óssea, consolidando sua atuação no campo dos biomateriais bioativos. Ao longo de sua carreira, publicou artigos de impacto em periódicos como Langmuir, Biomacromolecules, Journal of Biomedical Nanotechnology, Macromolecular Bioscience, Journal of Physical Chemistry B, Chemical Physics e Journal of Colloid and Interface Science, além de contribuir com capítulo de livro na área de nanomedicina, ampliando sua presença internacional na literatura científica.

Entre suas contribuições relevantes, destacam-se estudos sobre auto-organização de elastina recombinante e copolímeros responsivos à temperatura, síntese e caracterização de nanopartículas funcionalizadas, incluindo magnetita peguilada e nanocápsulas multifuncionais, e sistemas poliméricos capazes de encapsular e liberar fármacos de forma controlada, com foco em aplicações oncológicas e terapêuticas avançadas. Sua pesquisa também inclui extensas investigações termodinâmicas envolvendo surfactantes, copolímeros e sistemas micelares complexos, bem como análises detalhadas de interações entre proteínas e fármacos anfifílicos, contribuindo para o entendimento de processos de dobramento, estabilidade e agregação proteica. Com forte perfil interdisciplinar, o pesquisador tem colaborado com grupos internacionais de renome em bioengenharia, físico-química de materiais, nanotecnologia e biotecnologia aplicada, contribuindo para o desenvolvimento de estratégias inovadoras em engenharia de tecidos, medicina regenerativa e materiais biomiméticos.

Ao longo de quase duas décadas de produção científica contínua, Emilio Castro Otero consolidou uma carreira marcada pela investigação rigorosa, inovação metodológica e abordagem integrada da ciência dos materiais, oferecendo contribuições relevantes tanto para o avanço do conhecimento fundamental quanto para o desenvolvimento de soluções tecnológicas com potencial translacional na área biomédica.

ORCid: https://orcid.org/0000-0002-7491-4169

INDEX

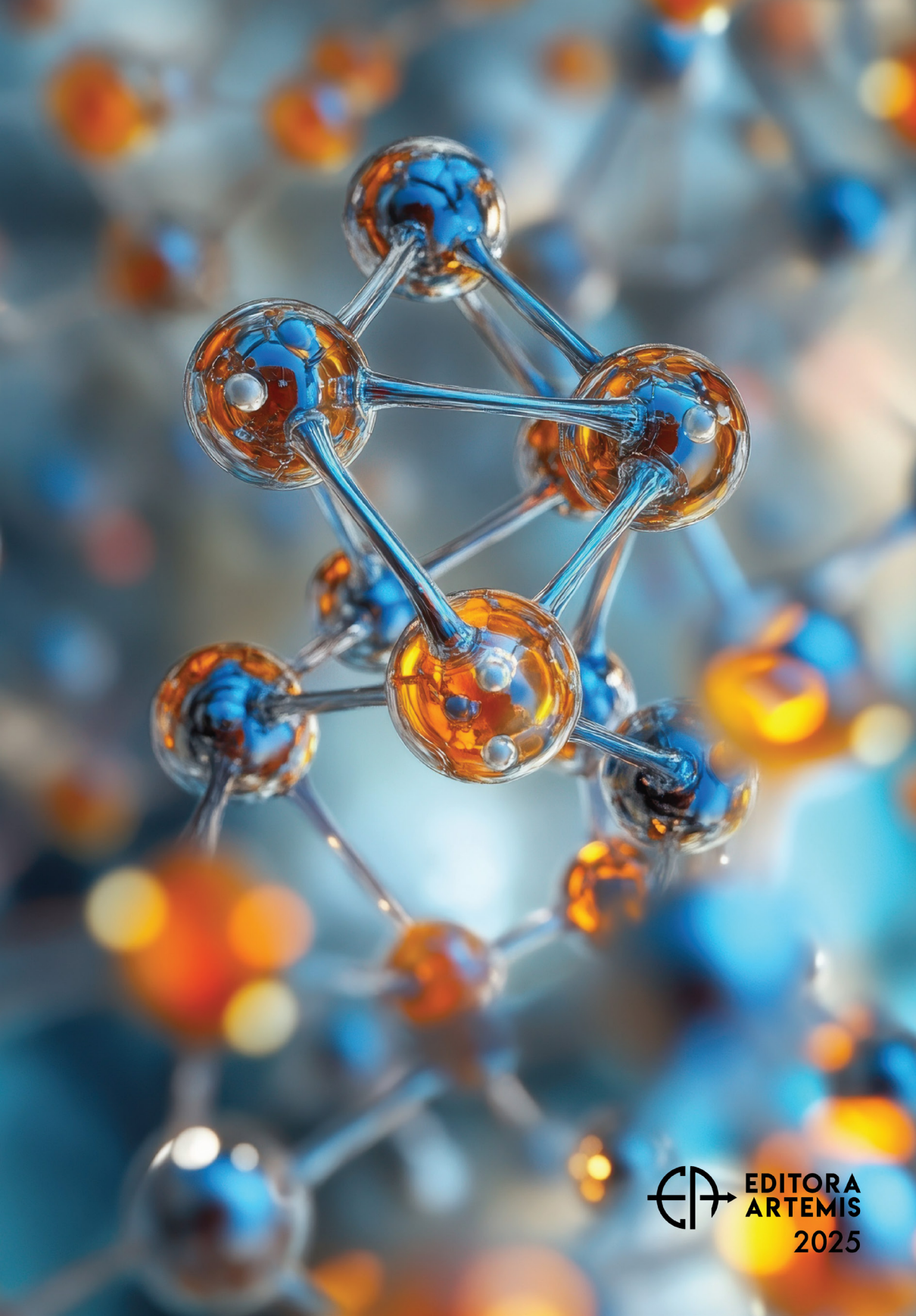

EDITORA ARTEMIS
2025